

# UC Davis

## UC Davis Electronic Theses and Dissertations

### Title

Prospects of Novel Compact Condensers for Multistage Flash Desalination

### Permalink

<https://escholarship.org/uc/item/3v88170p>

### Author

Safarkoolan, Ramuel

### Publication Date

2022

Peer reviewed|Thesis/dissertation

Prospects of Novel Compact Condensers for Multistage Flash Desalination

By

RAMUEL SAFARKOOLAN  
DISSERTATION

Submitted in partial satisfaction of the requirements for the degree of

Doctor of Philosophy

in

Mechanical and Aerospace Engineering

in the

OFFICE OF GRADUATE STUDIES

of the

UNIVERSITY OF CALIFORNIA

DAVIS

Approved:

---

Vinod Narayanan

---

Bryan M Jenkins

---

Valeria La Saponara

Committee in Charge

2022

*To my wife, Mina*

*Your confidence in me and your words of encouragement kept me going  
through uncertain moments*

# Prospects of Novel Compact Condensers for Multistage Flash Desalination

By

RAMUEL SAFARKOOLAN

**D**esalination is used in over 120 countries worldwide and is a viable option for providing fresh water for many regions worldwide. The chief approaches to desalination are Thermal Desalination (TD) and Reverse Osmosis (RO). While there have been significant improvements in membrane technology to enhance the efficiency of the RO process, TD research has been relatively less developed. In this dissertation, the prospect of improving TD is discussed with a specific focus on Multistage Flash (MSF) desalination. In MSF, the brine flows through a bank of tubes in multiple stages, in which steam flashes from the preheated brine. The steam condenses on the outer surface of the tubes and is collected as fresh distillate water. Condensers and the stages are made of exotic alloys to withstand harsh operating conditions and are capital intensive. MSF desalination plants have heat transfer bottlenecks related to phase change heat transfer external to the tubes and internal flow within the tubes. In this work, the potential to reduce the footprint of the tube condenser, and hence the size of the stages, by use of multi-port minichannel condensers is explored. The condenser footprint reduction is achieved by two methods: by tightly packing condenser plates and enhancing the overall

heat transfer coefficient. While the former reduces the condenser footprint, the latter directly reduces the condenser heat exchange area and hence the condenser material cost. An analytical model is developed to predict the performance of a baseline tube bank condenser and proposed multi-port minichannel condensers. A parametric study using the model is undertaken to assess the impact of variations in geometrical parameters on the multi-port condenser performance, results of which are used to optimize the condenser architecture. The results of the parametric study point to the possibility of a 90% size reduction corresponding to a 17% material cost reduction.

A numerical model is developed to test the effect of plate spacing on condensation. From the results, it is concluded that for the geometry of the proposed condenser plate spacing of 6 mm does not adversely affect condensation.

An experimental study on condensation using multi-port mini-channels is performed, and the results validate the model within a mean average error of 7 percent. Improvements in the performance of the condenser are observed using hydrophobic coatings.

Preliminary long-term salt deposition experiments are performed for  $\text{CaCO}_3$  to quantify the potential adverse effects of fouling on condenser performance. These initial results do not show any change in pressure drop over 48 hours of testing at 60 °C.

Overall, a potential path to a reduction in the size of MSF condensers and stages is demonstrated in this work.

Contact:

[Ramuel.s.k@gmail.com](mailto:Ramuel.s.k@gmail.com)

# Contents

.....	1
<b>Chapter 1: Background and Objectives .....</b>	<b>1</b>
<b>1.1. History .....</b>	<b>2</b>
<b>1.2. Types of Desalination.....</b>	<b>5</b>
1.2.1. Reverse Osmosis .....	5
1.2.2. Thermal Desalination.....	7
<b>1.3. Why Thermal Desalination .....</b>	<b>10</b>
<b>1.4. Motivation and Objectives .....</b>	<b>13</b>
.....	<b>16</b>
<b>Chapter 2: Analytical Model .....</b>	<b>16</b>
<b>2.1. Overview of the Proposed Condenser Relative to Conventional Condensers for MSF ...</b>	<b>17</b>
<b>2.2. Unit Cell Analytical Model .....</b>	<b>19</b>
2.2.1. Effectiveness-NTU- Method.....	20
2.2.2. Fouling Resistance .....	21
2.2.3. Conduction Resistance .....	21
2.2.4. Brine (Internal Flow) Convection Resistance .....	23
2.2.5. Phase Change Resistance.....	26
2.2.6. Channel Pressure Drop .....	37
<b>Chapter 3: Effect of Plate Spacing on Condensation.....</b>	<b>39</b>
<b>3.1. Variable Interfacial Shear Stress .....</b>	<b>45</b>
3.1.1. External Flow with Varying Pressure Gradient and Suction .....	45
3.1.2. Internal Flow with Varying Pressure Gradient and Suction.....	47
<b>3.2. Local Saturation Temperature .....</b>	<b>48</b>
<b>3.3. Solution Procedure.....</b>	<b>48</b>
<b>3.4. Results and Discussions.....</b>	<b>52</b>
<b>3.5. Chapter Conclusions .....</b>	<b>58</b>
.....	<b>61</b>
<b>Chapter 4: Parametric Study of the MSF Condenser .....</b>	<b>61</b>

4.1. Plate Gap and Aspect Ratio .....	65
4.2. Effect of Condenser Material .....	67
4.3. Dominant Resistance for Varied Fouling Resistance .....	70
4.4. Combined effect of phase change enhancement and channel size .....	71
4.5. Chapter Conclusions .....	75
.....	78
<b>Chapter 5: Experimental Validation.....</b>	<b>78</b>
5.1. Introduction .....	79
5.2. Experiment.....	79
5.2.1. Experimental Apparatus, and Facility.....	79
5.2.2. Multiport Condenser Test Articles .....	81
5.2.3. Hydrophobic Coating.....	83
5.2.4. Experimental Procedure and Data Analysis .....	84
5.2.5. Statistical Analysis .....	87
5.2.6. Results and Discussion.....	89
5.3. Chapter Conclusion.....	111
.....	113
<b>Chapter 6: Fouling.....</b>	<b>113</b>
6.1. Background .....	114
6.2. General Theory of Fouling .....	119
6.3. Modeling of Crystallization Fouling .....	122
6.3.1. Type of Salts.....	122
6.3.2. Solubility of $CaCO_3$ in solutions with different temperatures. ....	125
6.3.3. $Ca^{2+}$ Equilibrium Concentration .....	126
6.3.4. Rate of Deposit .....	131
6.3.5. Rate of Removal .....	136
6.3.6. Fouling growth.....	138
6.4. Experimental Investigation .....	141
6.4.1. Procedure:.....	141
6.4.2. Experiment Initiation .....	143
6.4.3. Daily Startup Procedure.....	144
6.4.4. Daily Shutdown Procedure .....	144
6.4.5. Data Processing .....	145
6.4.6. Experiment Results and Discussion .....	145
6.5. Chapter Conclusion.....	152



.....	<b>153</b>
<b>Chapter 7: Conclusions and Future Work.....</b>	<b>153</b>
7.1. Conclusions.....	154
7.2. Future Work .....	158
<b>Chapter 8: Extras .....</b>	<b>159</b>
<b>8.1. Nomenclature.....</b>	<b>159</b>
8.1.1. English.....	159
8.1.2. Greek .....	160
8.1.3. Sub-and Superscript.....	160
<b>8.2. References .....</b>	<b>161</b>
<b>8.3. Acknowledgment .....</b>	<b>167</b>
<b>8.4. Appendix I: Steam Chamber Blueprint .....</b>	<b>168</b>
<b>8.5. Appendix II: Derivation of steam velocity.....</b>	<b>177</b>
<b>8.6. Appendix III: Other subcooling results.....</b>	<b>189</b>
8.6.1. $T_{sat} = 100\text{ }^{\circ}\text{C}$ .....	189
8.6.2. $T_{sat} = 80\text{ }^{\circ}\text{C}$ .....	191
8.6.3. $T_{sat} = 60\text{ }^{\circ}\text{C}$ .....	193

## List of Figures

Figure 1-1. A conventional once-through MSF plant with n number of stages, Q thermal energy input, and operating temperature range of TBT-BBT.....	8
Figure 1-2. Unit water cost trends for MSF, and reverse [3] .....	12
Figure 2-1.a conventional MSF tube bundle configuration. [26] b. proposed minichannel condenser configuration. c. single multiport geometry.....	18
Figure 2-2. a) Condenser geometry, b) condensation conditions, c) heat transfer resistance diagram for the half channel. $L$ is the length of a single plate. $H$ is the height of a single plate. $\Delta$ is the plate-to-plate space, vapor space length. $W$ is the width of the condenser plate. Subscripts, $ch$ , $conv$ , $cond$ , $f$ , $phx$ , and $sat$ correspond to channel, convection, conduction, fouling or fluid, phase change, and saturation respectively.....	19
Figure 2-3. a) Multiport condenser plate. b) Control volume and coordinate system. c) Free body diagram.....	27

Figure 3-1. Front view of the proposed condenser. Vapor flow in a) counter-current, b) co-current configurations. c) Control volume and coordinate system. d) Conservation of mass diagram. ....	40
Figure 3-2. a. discretization of the vapor space along the vertical axis into $n$ $dx$ tall and $\Delta$ wide control volumes. b. Steam control volume .....	49
Figure 3-3. Nondimensional plate-height-averaged coefficient of heat transfer, $h$ , vs film-wise Reynolds number, $ReL$ , at different nondimensional shear stress, $\tau_0^*$ . Continuous lines represent Rohsenow's exact solution, while the solid squares correspond to the discretized mathematical numerical solution with $n = 200$ , and $\Delta = 1m$ .....	53
Figure 3-4: Effect of varied plate spacing of a. 1mm, b. 6mm, c. 10 mm, d. 1000 mm, plate height, and subcooling on plate-height averaged subcooling for $n = 200, T_{sat} = 40^\circ\text{C}$ . Mustard, green, and blue shapes represent 4, 8, and 12 K subcooling respectively. ....	55
Figure 3-5: Effect of varied plate spacing of a. 1mm, b. 6mm, c. 10 mm, d. 1000 mm, plate height, and subcooling on Nusselt number ratio for $n = 200, T_{sat} = 40^\circ\text{C}$ . Mustard, green, and blue shapes represent 4, 8, and 12 K subcooling respectively. ....	56
Figure 3-6: Effect of varied plate spacing of a. 1mm, b. 6mm, c. 10 mm, d. 1000 mm, plate height, and subcooling on heat of condensation ratio for $n = 200, T_{sat} = 40^\circ\text{C}$ . Mustard, green, and blue shapes represent 4, 8, and 12 K subcooling respectively. ....	57
Figure 4-1. The effect of varied plate gap, and aspect ratio, on dimensionless a. length, b. pressure, and c. overall heat transfer coefficient .....	65
Figure 4-2. The effect of varied material thermal conductivity on condenser parameters for different scales. $\Delta = 1$ cm, $T_v = 59^\circ\text{C}$ , $T_i = 50$ , $R_{fouling, tube} = 0.203 \text{ m}^2 - \text{k/kW}$ , $H_p = 4.3$ mm, $W_p = 1.8$ mm, $n_{ch} = 6$ $\Delta p = 58$ kPa, $T_{hw} = 300 \mu\text{m}$ .....	68
Figure 4-3. The effect of varied fouling resistance on overall resistance. ....	70
Figure 4-4. The combined effect of phase change and compact condenser scale on overall resistance. Top right inset: compact condenser scale factor, $Sc = W_c/H_c$ .....	72
Figure 4-5. The combined effect of phase change enhancement and minichannel scale on the minichannel condenser parameters. ....	75
Figure 5-1. Experiment loop .....	81
Figure 5-2. Experimental loop A 3D view of two of the testes articles, a) single plate and b) 5-plate condenser. c) Experiment apparatus. d) condenser plate internal dimensions. e) 5-plate plate configuration. All dimensions are in mm. ....	82
Figure 5-3. a-d repeated recorded advancing contact angle on the 120 surfaces. Recorded advancing contact angle on the e. 600, and f. 2000 surface .....	84
Figure 5-4. Condensation flux vs different flow rate for different subcooling for the single plate test article. ....	91
Figure 5-5. Overall heat transfer coefficient vs hydraulic-diameter based Reynold number for different subcoolings for the single plate test article. Condensation length, and area for the single plate configuration was found to be $234.9 \pm 0.01$ mm, and $148.6 \pm 0.024$ cm <sup>2</sup> respectively. Chamber pressure varied between 25.6-28.5, 12.3-14.9, and 18.5-30.3 kPa for 4, 8, 12 K subcooling respectively during the experiment. ....	93
Figure 5-6. Per plate heat flux of condensation vs per plate flow rate for the 6 mm 5-plate test article. ....	94

Figure 5-7. Overall heat transfer conductance vs hydraulic-diameter based Reynold number for the 5-plate 6 mm plate spacing test article. For this article the plate-averaged length of condensation was measured to be  $225.0 \pm 0.01$  mm, and the entire condensation area to be  $711.5 \pm 0.117$  cm<sup>2</sup>. Chamber pressure varied between 23.02-26.14, and 32.89-37.20 kPa for 4, 8 K subcooling respectively during the experiment. .... 95

Figure 5-8. Per plate heat flux of condensation vs per plate flow rate for the 4 mm 5-plate test article. .... 96

Figure 5-9. Overall heat transfer conductance vs hydraulic-diameter based Reynold number for the 5-plate 4 mm plate-to-plate spacing test article. For this article the plate-averaged length of condensation was measured to be 230.1 mm, and the entire condensation area to be  $727.6 \pm 0.119$  cm<sup>2</sup>. Chamber pressure varied between 31.04-41.07, and 23.26-23.66 kPa for 4, 8 K subcooling respectively during the experiment. The dotdashed lines represent arbitrary fit curves used for demonstration purposes. .... 97

Figure 5-10. Top view of the 4mm plate-to-plate spacing article for 36 g/s 4 K subcooling condition. a. Film formation on the outer plate (top plate in the current picture) compared to dry patches observed on the inner plate (yellow dashed box). b. A more detailed picture of inner plates with apparent more dry patches in between the plates. c. point of view 98

Figure 5-11. Condensation flux vs different flow rate for different subcoolings for the single plate test article with hydrophobic promoter. .... 99

Figure 5-12. Overall heat transfer coefficient vs hydraulic-diameter based Reynold number for different subcoolings for the single plate test article coated with the dropwise promoter. Condensation length and area for the coated single plate configuration was found to be  $235.1 \pm 0.01$  mm, and  $148.7 \pm 0.024$  cm<sup>2</sup> respectively. Chamber pressure varied between 37.5-38.9, 64.5-49.7, and 51.1-55.5 kPa for 4, 8, and 12 K subcooling respectively during the experiment. A 5.5 μm promoter thickness and a thermal conduction of 0.25 W/m – K was assumed for the calculated values. .... 100

Figure 5-13. Condensation flux vs different flow rate for different subcoolings for the single plate test article with hydrophobic promoter. .... 101

Figure 5-14. Overall heat transfer coefficient vs hydraulic-diameter based Reynold number for different subcoolings for the single plate test article coated with the dropwise promoter. For this article the plate-averaged length of condensation was measured to be 229.2 mm, and the entire condensation area to be  $724.7 \pm 0.119$  cm<sup>2</sup>. Chamber pressure varied between 37.3-38.9, 64.2-65.7 kPa for 4, and 8 K subcooling respectively during the experiment. A 5.5 μm promoter thickness and a thermal conduction of 0.25 W/m – K was assumed for the calculated values. .... 102

Figure 5-15. Flux of condensation vs plate flow rate comparison between P1H and P1 for different subcoolings. .... 104

Figure 5-16. Overall heat transfer coefficient vs hydraulic-diameter based Reynold number comparison between 6 mm plate-to-plate spacing configuration and the single plate. . 105

Figure 5-17. Overall heat transfer conductance vs hydraulic-diameter based Reynold number comparison between Δ4 and P1. .... 106

Figure 5-18. Overall heat transfer coefficient vs hydraulic-diameter based Reynold number comparison between Δ6, Δ4, and Δ4H. .... 107

Figure 5-19. Log-log Heat flux of condensation parity plot for all the test configuration at any available subcooling. %35, %10, and -10% error lines.....	108
Figure 5-20. Log-log overall heat transfer coefficient parity plot for all the test configuration at any available subcooling. %35, %10, and -10% error lines. ....	109
Figure 6-1. Concentration vs temperature graph for: a. invers-solubility salt, b. normal solubility salt. Solid line indicates equilibrium salt concentration.....	123
Figure 6-2. Total scale composition vs temperature for common seawater figure adopted from [75] .....	124
Figure 6-3. Temperature and concentration gradient for an inverse solubility salt in vicinity of a heated surface.....	131
Figure 6-4: Test piece assembly.....	142
Figure 6-5: Long term salt deposition test assembly schematic.....	143
Figure. 6-6: High Range (HRDP) Pressure Drop, top, and Low Range Pressure Drop (LRPD), bottom, time series for the first experiment. The abscissa is cumulative operating time.....	147
Figure 6-7: Normalized surface temperature time series for the first experiment. Normalization was achieved by subtracting surface temperature from inlet temperature. SMTC2 is the closest and SMTC4 is the furthest from the inlet. The abscissa is cumulative operating time. ....	148
Figure 6-8: Temperature gain across plena time series for the first experiment. The abscissa is cumulative operating time.....	149
Figure 6-9: Reservoir salinity time series as well as the peristaltic pump set point. Data for last portion of the 5 <sup>th</sup> day was not recorded. Data has been cleaned up to remove the effect of moving average applied to data adjacent to zero values.....	150

## List of Tables

Table 1-1: Mean value of total dissolved salts in various global bodies of water [7], [8]...5	
Table 2-1: Plant technical design data from [25] considered as baseline .....	17
Table 2-2: Nusselt numbers for fully developed laminar flow in tubes of differing cross section [27].....	24
Table 3-1: Prescribed conditions, and their variation.....	53
Table 5-1: 4-point average contact angle measurement for different surface roughness. 83	
Table 5-2: Measured value, their range, .....	87
Table 5-3: Experiment matrix, range, and results.....	89
Table 6-1: Some inverse solubility salts [61] .....	125
Table 6-2: Solubility product, $K_{sp}$ for $\text{CaCO}_3$ as a function of temperature. [7].....	127
Table 6-3: Values of $Ea$ , $K_0$ used in the literature for $\text{CaCO}_3$ , $\text{CaSO}_4$ .....	140



# Chapter 1: Background and Objectives



## 1.1. History

Desalination, the process of separating salts and other dissolved solids in water in order to lower its salt content, is as old as written history. It was known to the Greeks that the vapor of ocean water did not carry salt. In his treatise *Meteorologica*, Aristotle noted that when saltwater turned to vapor, it became "sweet" and that this vapor did not form salt water again when it condensed [1]. Until the turn of the 17th century, desalination was used to provide potable water to sailors.

The scarcity of fresh water sources and the need for additional water supply is already essential in water-stressed regions of the world and will be increasingly significant in the future. About 800 million people have no access to safe drinking water, and one out of every five deaths of children under 5 is due to water-related diseases [1]. In addition, over 25 countries have reached water poverty, a number which is believed to increase to 65 by the year 2025 [2].

Desalination is used in over 120 countries worldwide and is one of the most viable options for providing fresh water for many regions worldwide. In many countries, it is more economical to desalinate saline water than to transport fresh water from several hundred kilometers away from natural water resources. Countries located in the Arabian Peninsula, including Saudi Arabia, Kuwait, Qatar, Bahrain, United Arab Emirates, and Oman, do not have a single natural perennial river and are heavily dependent on desalinated water. The latter two countries rely entirely on desalinated water for domestic and industrial supplies [3]. In 2010, it was estimated that around 60 million m<sup>3</sup>/day of desalinated water

was produced, of which 41.3% was in the Middle East and North African (MENA) region [4].

In this country, and in states such as California, multi-year droughts have threatened to become the new norm in the United States, forcing the state to take unprecedented steps in water conservation and regulation [5]. In addition to the need for freshwater for population centers, typically located in the coastal areas, there is a growing need to provide freshwater to inland agricultural areas. California's Central Valley spans 450 miles in length and 40-60 miles in width and is the source of about 50% of the fresh fruits, vegetables, and nuts in the United States. Salinity levels of freshwater sources in this valley are increasing at an alarming rate [6]. Run-offs occur when the ground beneath the running water can no longer absorb the mass of water due to saturation, leading to formation of streams or bodies of water. This excess of water has natural causes such as melting, rain, or storm or can be manmade by agricultural irrigation. The stream of water absorbs minerals such as salts as it traverses the ground from one location to its final location. A problem arises when this excess of salt settles and eventually permeates to the groundwater, contaminating the very freshwater agriculture depends on. For example, in California's Central Valley, the Tulare basin does not have any outlets to discharge over two million tons of salt per year brought in from the north by irrigation water. A drain to the basin was initially proposed but never constructed due to environmental and cost, which has led to the buildup of selenium and other metals causing significant environmental damage. This lack of drain has continued to be problematic for irrigated

agriculture. In-valley desalination for irrigation water, among other methods of removing salt from groundwater and tailwater, is a potential solution to the problem.

Sea water salinity not only changes with location, but also with the time of the year. Factors such as freezing, evaporation, precipitation, droughts, and temperature fluctuations effect the salinity both seasonally, and locationally. Similarly, agricultural drainage salinity, and composition vary with location and season. Seasonal watering schedules, and soil year-around composition can alter drainage salinity, and composition significantly. Salinity is categorized into four major groups based on salinity:

1. Drinking water with a zero ppt salinity,
2. Brackish water, a superset of agricultural drainage with a maximum of 2 ppt, includes some bodies of water such as the Baltic Sea, Caspian Ocean, and Baltic Ocean has a cut-off limit of 30 ppt,
3. Salt water such as those found in Pacific Ocean, Indian Ocean, and Persian Gulf are categorized as Saline water and are limited to 50 ppt, and, lastly,
4. Briny water such as the ones found in Australian Shark Bay, Dead Sea, Lake Urmi, and Don Juan Pond with a salinity as high as 4000 ppt.

Table 1-1 is a collection of mean total dissolved solids, also known as salinity, for global bodies of water. One part per thousand equates to approximately a gram of salt per liter of water.

As seen from table 1-1 the variation in salinity of different bodies of water is large.



Table 1-1: Mean value of total dissolved salts in various global bodies of water [7], [8]

Body of Water	TDS (PPM)	Body of Water	TDS (PPM)
Baltic Sea	7,000	Indian Ocean	33,800
Caspian Sea	13,500	Mediterranean Near Crete	37,900
Black Sea	20,000	Mediterranean	39,000
White Sea	28,000	Persian Gulf	50,000
North Atlantic	29,000	Australian Shark Bay	70,000
Pacific Ocean	33,600	Kara Bogas (Caspian Ocean)	164,000
Atlantic South	36,000	Dead Sea	220,000
North Atlantic	36,200	Lake Urmi	280,000
Adriatic Sea	31,400	Don Juan Pond	400,000

For example, Baltic Sea has only 7 grams of salt dissolved in one liter of water, while Don Juan Pond has as much as 400 grams of salt dissolved in one liter of salt water.

## 1.2. Types of Desalination

Thermal Desalination (TD) and Reverse Osmosis (RO) are the two main desalination approaches. About two-thirds of worldwide desalination is produced using the RO approach while the other third relies on TD [4]. Thermal desalination is predominantly used in the Persian Gulf countries and the North African region, while most of other countries with recent demand for desalination utilize RO to meet their needs.

### 1.2.1. Reverse Osmosis

When two liquids of different concentration are separated by a semi-permeable membrane allowing for the passing of solvent (water molecules) but not the solute, to minimize system chemical potential, the solvent from the fluid with lower concentration moves to the fluid with higher concentration, a process known as forward osmosis. However, when

the opposite direction of solvent transport is desired, as is the case with desalination, energy must be provided to reverse this natural tendency called osmotic pressure. The energy demand to overcome the osmotic pressure is proportional to the concentration difference between the two fluids.

Reverse osmosis (RO) systems have succeeded in securing a larger share of the world seawater desalination market as a result of progress made in membrane technologies and energy recovery devices, enabling lower specific water cost ( $\$/\text{m}^3$ ). Elimelech et al. [9] reported a decrease of energy requirement of RO to 17% of its value compared to the 1970 value. Despite being highly energy efficient, the massive pumps used in RO to overcome osmotic pressure require high-grade energy in the form of electric power. This power requirement can introduce challenges when considering the water-energy nexus - the entangled linkage between water requirement to generate energy, and the energy required to create energy.

In California, RO plants have been proposed along the California coast to cater to cities such as Los Angeles and San Diego; one of the plants is the new 50 million gallons per day Claude “Bud” Lewis desalination plant located near Carlsbad, north of San Diego [6]. McCool et al. [7] investigated the feasibility of RO systems for treating agricultural runoff in the San Joaquin Valley. Water salinity was in the range of 7000-23,000 ppm with wide yearly variation. They demonstrated that with proper mitigation of scaling, RO has a 44 % to 66 % regionwide fresh to feed water ratio (i.e., recovery ratio). Recovery ratio is related to the pumping power consumed in making fresh water, hence, achieving higher recovery ratios, without effecting the system long-term longevity, the better the system

economics. Additionally, McCool et al. concluded that site-specific process optimization is imperative, as well as real-time monitoring for fouling mitigation resulting from time time-varied feed chemistry. In a follow-on study, Thompson et al. [10] monitored the performance of a 65% recovery ratio RO plant that used a 14,000-ppm feed water source in the San Joaquin Valley. They observed rapid performance decline due to the accumulation of scale.

While RO is a viable option for domestic water purification, despite the advances made in this technology, high scaling affinity of brackish and subsurface wastewater as indicated by feed water salinity, time and location (Table 1-1) variations in feed water chemistry, cost of pretreatment, and equipment adaptation prevents RO from fully addressing the issue of wastewater management.

### *1.2.2. Thermal Desalination*

Thermal desalination (TD) works by boiling pretreated feed water, and condensing the resulting vapor, producing salt-free water. Feed water sources vary over a wide range of salinity and composition, such as ocean water, brine, or agricultural run-off.

Among thermal desalination technologies, Multi-Stage Flash (MSF) desalination has proven to be a reliable and a mature thermal solution over the span of its more than 60 years of service.

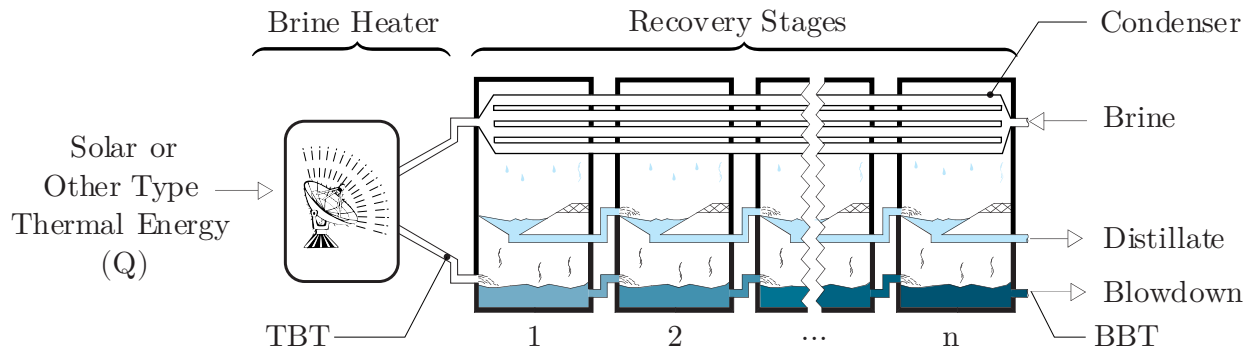


Figure 1-1. A conventional once-through MSF plant with  $n$  number of stages,  $Q$  thermal energy input, and operating temperature range of TBT-BBT.

Figure 1-1 is a simplistic graphical representation of a once-through MSF plant. In a once-through MSF plant, brine enters condenser tube bundle, heating up as it passes through recovery stages. External heat is applied to the brine, through a brine heater, and brine is raised to the desired temperature. This temperature is the highest operating brine temperature which is commonly referred to as the Top Brine Temperature, or TBT. Having gone through the brine heater, the brine is directed into the first flashing chamber. The saturation temperature corresponding to the chamber pressure is lower than the temperature of the inlet brine. The brine is at the meta-stable supersaturated liquid state at that pressure. The supersaturated brine goes through simultaneous homogenous and heterogenous boiling as it releases excess heat in the form of latent heat of evaporation. The brine is then directed to the next stage, each of which is at a progressively lower pressure than the preceding stage. This reduction in saturation pressure ensures that the brine continues to flash throughout the stages, which in turn maximizes distillate output. Finally, blowdown, the remaining flashed brine in the last stage, is ejected from the system. Blowdown has the lowest brine temperature, and, thus, it is called Bottom Brine

Temperature, or BBT in the MSF desalination literature [11]. The steam produced at each stage, condenses on the condenser surface, and is collected in distillate trays. Much like the brine, distillate produced in the previous stage flashes in the next stage, ensuring maximum possible heat recovery. The accumulation of the distillates produced in all the stages is the finished product of a desalination plant.

When comparing desalination plants, two metrics are usually used. The first metric is the specific energy which is defined as the energy input ( $Q$ ) through brine heater per kilogram of distillate produced. The second metric is the specific flow rate which is defined as the required brine flow to produce unit distillate flow [ $\text{kg}_b/\text{kg}_d$ ]. Reducing the specific energy translates directly into energy savings, and reducing the specific flow rate reduces the required pumping power and pump size. Maintaining the same level of distillate production while lowering the two metrics is a desired outcome. For a fixed operation range, increasing the number of stages, up to the thermodynamic limit, reduces the required system energy input, and hence reduces the specific energy input. On the downside, as the stage number reduces so does the condensation driving force, cooling brine inlet temperature minus stage vapor temperature. The continued reduction in the condensation driving force will lower condensation heat flux, and hence increases required heat transfer area, or, if the thermodynamic limit is reached, will completely stop condensation. Thermodynamic limit is reached when the cooling brine temperature is equal to the stage temperature. Due to the presence of salt, brine has a higher evaporation point, and hence higher vapor temperature compared to pure water, a phenomena known as boiling point elevation. Boiling point elevation is a function of salinity which can cause

condensation to cease for lower driving temperatures than the ones observed for pure water. Increasing the operating temperature range, TBT-BTB, increases the distillate production for the same brine flow rate, thereby reducing the specific flow rate metric. While the BTB is limited by the feed water temperature, TBT is determined by the available thermal resources, fouling, and corrosion mitigation technology.

### **1.3. Why Thermal Desalination**

Thermal desalination is more energy intensive compared to reverse osmosis and makes economic sense only with low-cost heat sources. However, most of the energy needed for thermal desalination is in the form of low-grade heat rather than electricity. Additionally, thermal desalination technology is occasionally coupled with thermo-electric power generation plants, an approach intended to improve the combined efficiency achieved through TD's potential to make use of the low-grade exhaust heat from the power plant. Coupling thermal desalination with solar energy, in locations at which low-grade exhaust energy is not available, expands the viability and sustainability of such systems. The available solar energy can either be converted to heat and used as input energy to desalination plants, or converted to electricity and used to run RO plants. The solar-to-electric efficiency of the combined photovoltaic-thermal panels, water cooled PV, exceeds that of regular solar panels [12], yet solar collectors designed to directly convert solar to thermal power are known to be far more efficient, and economical [13]. These highly efficient and relatively inexpensive solar collectors make their coupling to thermal desalination a superior option when compared to PV coupled RO systems.

Recently, a pilot demonstration of solar thermal desalination to purify agricultural runoff has been successfully performed in California [14]. The US Department of Energy has recently invested in advancing thermal desalination technologies as well as in lower cost solar thermal concentrators to reduce the capital cost of thermal desalination with emphasis on high salinity and zero liquid discharge [15].

Reverse osmosis systems, on the other hand, even when equipped with expensive site-specific filters, have an energy efficiency that is highly dependent on the consistency of the feed water [10]. While this challenge can be addressed by understanding, and hence predicting, the time-varying feed water chemistry change for large reservoirs such as oceans and ponds, such predictions for ever-changing feed-water sources such as agricultural run-off is at best futile. It is true that thermal desalination requires feed pre-treatment, but the requirements are lower and less site specific when compared to reverse osmosis.

Desalinated water cost for both reverse osmosis and thermal desalination is dropping considerably over the past five decades [16]. Figure 1-2 shows a comparison of the cost of producing 1 m<sup>3</sup> of water between RO and MSF over the years. Thermal desalination price has dropped 2.5 times since 1970, and reverse osmosis price has halved since 1975. This price reduction in TD is mainly due to process innovation and increased competition [16].

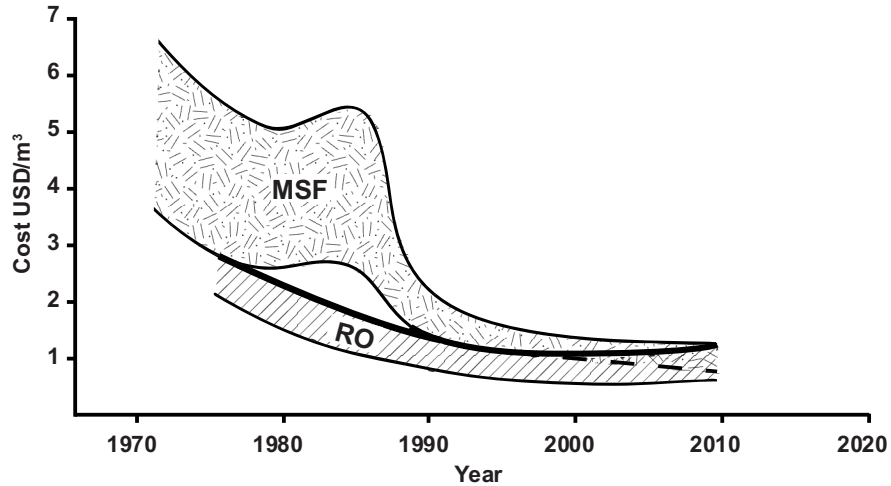


Figure 1-2. Unit water cost trends for MSF, and reverse [3]

The more forgiving nature of thermal desalination, as far as energy intake, and feed water robustness, coupled with competitive pricing compared to RO, are the advantages of this technology. However, in a fair comparison it should be noted that in order to benefit from cheap thermal energy, thermal desalination is the better option when performed either in vicinity of plants near which exhaust heat is available, or in areas with high thermal insolation when coupled to solar collectors. When considering potential sites for solar driven thermal desalination, coastal regions with inherent high solar insolation come to mind. Even when solar energy input is not a part of the design consideration, when built in the coastal areas, stand-alone thermal desalination plants receive operational cost savings owed to reduced required pumping power. These highly coveted coastal regions come with larger land premium, and hence a reduction in plant footprint can considerably reduce large capital investments. Given the land cost near coastal areas, and, or insufficient solar insolation to justify economic feasibility, TD technologies may be employed in-land, desalinating brackish agricultural drainage, and ground water.



## 1.4. Motivation and Objectives

There have been a few improvements in the MSF technology on the economies of scale (capacity increase) and material selection. There has been no major improvement in specific energy, or breakthrough in configuration needed to scale down plants from large ones requiring large financial outlays and land footprint.

It is, therefore, that the overall goal of the present work is to reduce the size and hence capital cost associated with MSF thermal desalination thereby enabling development of potential modular desalination plants. Reduction in size of an MSF plant can be achieved by reducing the size of each stage or by reducing the number of stages. The latter would, as discussed earlier, increase the specific energy and is hence not desirable. The objective of this work is to enable stage size reduction by the means of condensation flux enhancement within each stage. The increase in condensation rate is two folds. On one side by using microchannel minichannel condensers as opposed to the traditional bank of tubes, internal (brine-side) heat transfer coefficient is increased, and on the other hand, phase change resistance on the vapor side is enhanced by promoting dropwise condensation.

As far as internal flow heat transfer enhancement is concerned a significant body of literature has emerged on fundamental thermal-fluidic aspects of minichannels. Minichannels have been used to enhance heat and/or mass transport in diffusion-limited conditions [17] [18], and have been used in several applications such as heat sink thermal management, compact heat and mass exchangers and chemical reactors [19] [20] [21] [22].

On the outside of the cold plates, phase change occurs due to either filmwise or dropwise condensation. As the name suggests in filmwise condensation, vapor condenses onto a sufficiently cold surface and forms of liquid film. In cases pertaining to this work, the condensed liquid film has a poor thermal conductivity and thus acts as a thermal insulation. On the other hand, heat transfer is shown to improve in dropwise condensation [23] [24] compared to filmwise condensation. In-depth discussion of both condensation mechanisms is presented in chapter 2.

Towards this objective, the following tasks are performed:

1. Modeling of the performance of a minichannel condenser: Steady state heat exchanger correlation-based modeling to predict the size of the condenser is performed.
2. Impact of plate spacing in the condenser bank: A semi-theoretical model is developed to determine the impact of condenser plate spacing and length on its performance.
3. Parametric study of the minichannel multiport condenser: Geometrical variations on multiport condensers and comparison of its performance relative to a traditional tube bank MSF condenser is performed in this task.
4. Experimental verification of the model results: The results of the experimental validation of the mini-channel condenser model is presented. Performance of a single condenser plate as well as an array of

condenser plates are experimentally measured and compared against the model developed in Task 1.

5. Impact of use of hydrophobic coating on minichannel condenser performance: An experimental and modeling study is performed to assess the benefits of hydrophobic coating on the performance of the minichannel condenser.
6. Assessment of fouling potential in the minichannel condenser: A preliminary experimental study of fouling in the minichannel condenser is performed.



## Chapter 2: Analytical Model



## 2.1. Overview of the Proposed Condenser Relative to Conventional Condensers for MSF

As discussed in Chapter 1, in each stage, vapor produced by flashing of the brine condenses on the outer surfaces of the condenser (Figure 1-1). Inside the condenser, the brine is preheated by the heat of condensation; this energy recuperation results in lower energy input to reach TBT, and hence higher performance ratio.

To understand the current limitations of MSF desalination, the first stage of unit #5 of “Umm Al Nar” East Extension, Abu Dhabi [25] with design parameters as laid out in Table 2-1 was chosen as a baseline and investigated.

Table 2-1: Plant technical design data from [25] considered as baseline

Parameter	Design Value
Brine Mass Flow Rate	4030 [kg/s]
Number of Tubes, $n_{tube}$	2861
Tube Inner Diameter	29.31 [mm]
Tube Thickness	1.2 [mm]
Tube Bundle Height, H	2.1 [m]
Tube Bundle Width, W	2.1 [m]
Condenser Length	15.9 [m]
Brine Inlet Temperature, $T_{b,i}$	80.4 [°C]
Brine Exit Temperature, $T_{b,o}$	83.6 [° C]
Stage Vapor Temperature, $T_{sat}$	87 [° C]
Fouling Resistance	0.20 [m <sup>2</sup> – K/kW]
Average Heat Transfer Coefficient	2.2 [kW/m <sup>2</sup> – K]

Conventional MSF condensers consists of a bundle of tubes arrangement. The tube bundle has a staggered arrangement configuration with a transverse pitch in width equal to 1.3

tube diameters, and a pitch in height equal to 1.125 tube diameters, arranged such that the centers of any three adjacent tube create an equilateral triangle (Figure 1-2.a) [26].

A preliminary study of the Umm al Nar plant reveals that the plant’s dominant heat transfer is equally due to internal resistance, and outside phase change resistance, and they each equally contribute 40% of the total resistance. Thermal resistances are discussed in detail in the following subsection.

To improve the baseline condenser, a compact condenser is proposed which has a higher surface to volume ratio than the baseline. The proposed compact condenser consists of parallel multiport plates with height,  $H_p$ , width,  $W_p$ , thickness,  $Th_{wall}$ , and gap spacing,  $\Delta$ . Internally, the plates have parallel channels running along the length. Plates are stacked vertically in a staggered fashion (Figure 2-2.b)

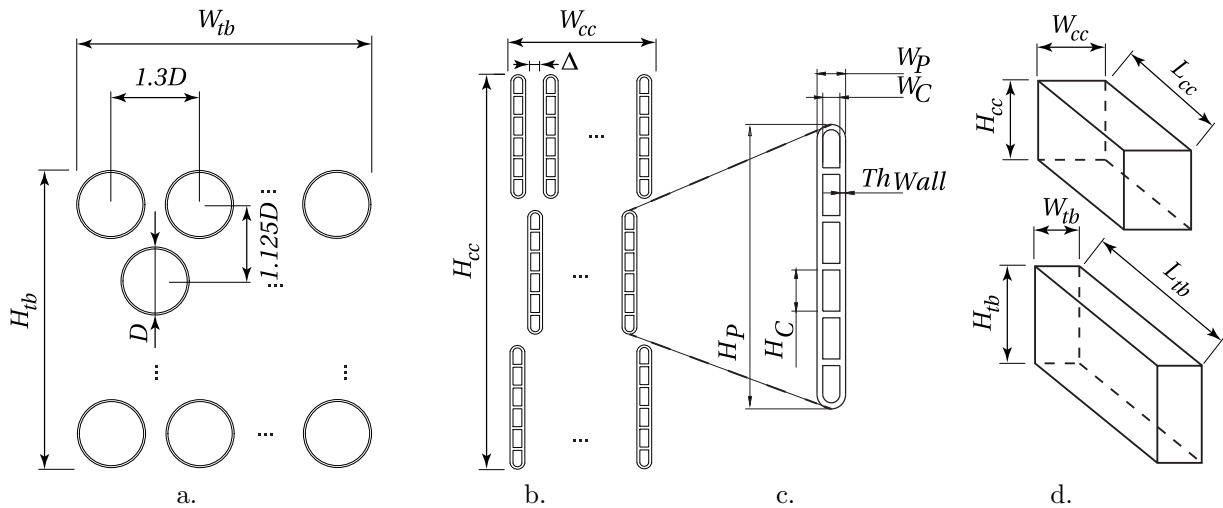


Figure 2-1.a conventional MSF tube bundle configuration. [26] b. proposed minichannel condenser configuration. c. single multiport geometry. d. condenser space comparison

In this chapter, a steady-state thermal design model of a unit cell is developed to predict the performance of the compact condenser. The unit cell is identified by the dashed box

in Figure 2-2. Upon development of this model, a semi-analytical model of the condenser vapor flow is also developed to determine the minimum spacing,  $\Delta$ , between the condenser plates based on consideration of vapor shear, and pressure variation in the vapor gap between plates due to condensation.

## 2.2. Unit Cell Analytical Model

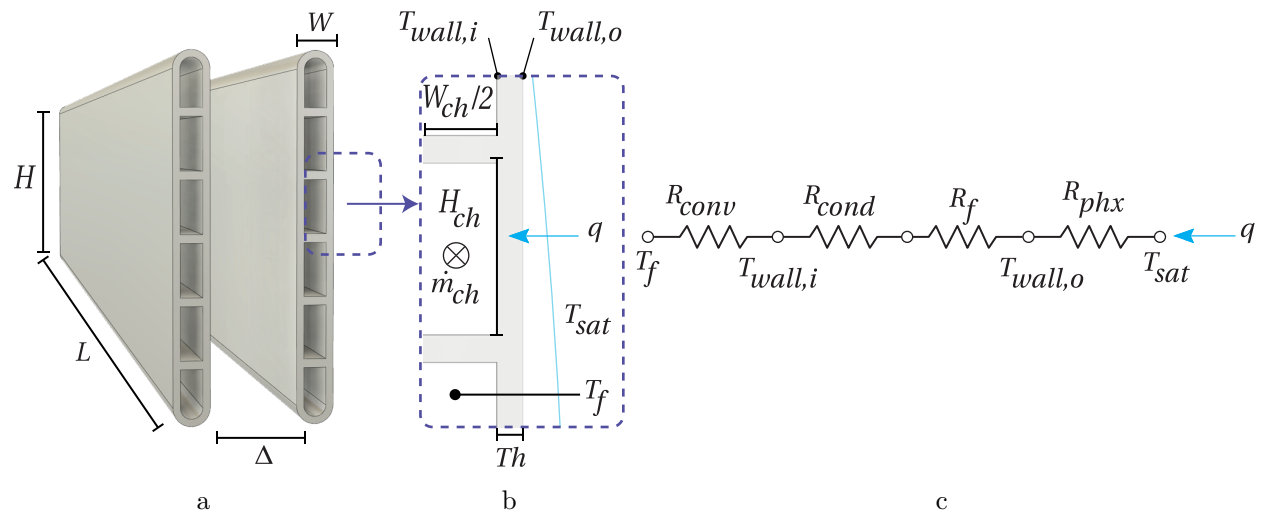


Figure 2-2. a) Condenser geometry, b) condensation conditions, c) heat transfer resistance diagram for the half channel.  $L$  is the length of a single plate.  $H$  is the height of a single plate.  $\Delta$  is the plate-to-plate space, vapor space length.  $W$  is the width of the condenser plate. Subscripts,  $ch$ ,  $conv$ ,  $cond$ ,  $f$ ,  $phx$ , and  $sat$  correspond to channel, convection, conduction, fouling or fluid, phase change, and saturation respectively.

A steady state heat transfer model of the condenser is developed based on the effectiveness-NTU (Number of Transfer Units) method. Using a circuit diagram, as laid out in Figure 2-2. c and the effectiveness-NTU method for a set of prescribed conditions and geometries (Figure 2-2. a-b) the required heat transfer conductance,  $U$ , is calculated. The overall heat transfer conductance is then used to calculate the required demand heat

transfer area. Due to available plate vertical symmetry, only half of the plate, as depicted in Figure 2-2.b, was modeled, the results of which were multiplied by a factor of two.

The following subsection describes the effectiveness-NTU method, which is followed by subsections on heat transfer resistances as described in Figure 2-2.c.

### *2.2.1. Effectiveness-NTU- Method*

For the condenser design, given a prescribed condensation rate,  $q$ , the effectiveness,  $\epsilon$ , of the condenser can be determined as:

$$\epsilon = \frac{q}{\dot{m}_w c_{p,w} (T_{sat} - T_{b,i})}, \quad (2-1)$$

in which  $T_{b,i}$  is the brine (cold side) inlet temperature,  $T_{sat}$  is the vapor temperature,  $\dot{m}_w$  is the mass flow rate of the brine, and  $c_{p,w}$  is brine specific heat.

For a heat exchanger with one fluid undergoing phase change, the effectiveness is given by the following expression

$$\epsilon = 1 - \exp(-NTU), \quad (2-2)$$

in which NTU is given by the following equation

$$NTU = \frac{UA}{\dot{m}_w c_{p,w}}. \quad (2-3)$$

Substituting equation (2-3) into equation (2-2) yields the following equation

$$\epsilon = 1 - \exp\left(-\frac{UA}{\dot{m}_w c_{p,w}}\right), \quad (2-4)$$



where  $UA$  is the heat transfer conductance and calculated as the reciprocal sum of the resistances as shown in Figure 2-2.c,

$$UA = \frac{1}{R_{conv} + R_{cond} + R_{phx} + R_f}. \quad (2-5)$$

Thus, to evaluate the heat transfer conductance, the individual heat transfer resistances pertaining to condensation, fouling resistance, conduction resistance, and internal brine convective resistance must be formulated. In Eq. (2-5),  $U$  is the overall heat transfer coefficient obtained using equations described in the next subsection. Equation (2-5) is an implicit function of  $A$ , which can be solved iteratively by assuming a value for  $A$  and comparing the values of  $\epsilon$  calculated independently from the equation (2-1) and (2-4).

### *2.2.2. Fouling Resistance*

The fouling resistance is quantified as

$$R_f = \frac{R'_f}{A_{fouling}}, \quad (2-6)$$

In which  $R'_f$  is a tabulated value found different sources [27] [26], and  $A_{fouling}$  is the area on which fouling occurs.

### *2.2.3. Conduction Resistance*

#### **2.2.3.1 Wall Conduction Resistance**

For a given brine inlet and exit temperature,  $T_{b,i}, T_{b,o}$  and condenser material, the wall conduction resistance is given by:

$$R_{cond} = \frac{Th_{wall}}{k_{wall}A_{cond}}, \quad (2-7)$$

where  $A_{cond} = H \times L$ , and  $L$ ,  $H$ , and  $Th_{wall}$  are the length, height, and the thickness of the plate respectively.

Thermal conductivity of condenser walls,  $k_{wall}$ , is evaluated at an average between the inlet and outlet temperature, i.e.

$$\begin{aligned} \overline{T_b} &= \text{average}(T_{b,i}, T_{b,o}), \\ k_{wall} &= k(\overline{T_b}). \end{aligned} \quad (2-8)$$

### 2.2.3.2 Dropwise Promoter Resistance

One of the variations studied included assessment of the impact of dropwise condensation on the performance of the compact condenser. To achieve dropwise condensation in presence of water vapor on metallic surface the surface often needs to be coated with a promoter. The resulting resistance caused by the usually low thermal conduction of such promoters often becomes as large as the internal resistance, and hence requires consideration in the resistance model. Like wall conduction consideration, promoter resistance is modeled by 2-D heat conduction through solids, so that

$$R_p = \frac{Th_p}{k_p A_p}, \quad (2-9)$$

where subscript  $P$  denotes promoter attribute. Unlike for metals, the thermal conduction of promoter material is not a strong function of temperature, and as such, its value has been treated as a constant in this work.  $A_p$  is equal to  $A_{cond}$ .

### 2.2.4. Brine (Internal Flow) Convection Resistance

In presence of fins, the convective resistance to heat transfer is given by

$$R_{conv} = \frac{1}{\eta_0 \bar{h}_{conv} A_{tot}}, \quad (2-10)$$

where  $A_{tot}$  is the entire wetted area of the unit cell (including fins),  $\bar{h}_{conv}$  is the single-phase convective coefficient of heat transfer, and  $\eta_0$  is the overall fin efficiency defined as:

$$\eta_0 = 1 - \frac{A_{fins}}{A_{tot}} (1 - \eta_f). \quad (2-11)$$

In equation (2-11),  $A_{fins}$  is the entire wetted fin area given by

$$A_{fins} = n_{ch} L W_{ch}, \quad (2-12)$$

$A_{tot}$  is total wetted area given by

$$A_{tot} = A_{fins} + n_{ch} L H_{ch}, \quad (2-13)$$

and, lastly,  $\eta_{fin}$ , is the fin efficiency calculated using

$$\eta_{fin} = \sqrt{\frac{\tanh(m L_c)}{m L_c}}, \quad (2-14)$$

where  $L_c$  is the adiabatic tip length, given by

$$L_c = (W_{ch} + T h_{wall})/2, \quad (2-15)$$

in which  $m$  is the fin characteristic number, defined as:

$$m = \sqrt{\frac{\bar{h}_{conv} P_{fin}}{k_{wall} A_c}}. \quad (2-16)$$

In equations (2-12), and (2-13)  $n_{ch}$  is the number of channels, and wall thickness is assumed to be equal to the wall thickness.

In equation (2-16)  $P_{fin}$  is the wetted perimeter of the fin

$$P_{fin} = Th_w W_c / 2, \quad (2-17)$$

and  $A_c$  is the fin cross section area as defined b


$$A_c = L_c L, \quad (2-18)$$

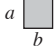

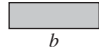
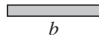

Evaluating the convective coefficient of the heat transfer requires knowledge of the condenser geometry and flow conditions. For the case of a fully developed internal laminar flow, (Reynolds number  $Re_D < 2300$ , from the analytical solution to the heat, mass, and momentum conservation equations, the following equation emerges:

$$Nu = \frac{\bar{h}_{conv} D_h}{k_f} = \mathcal{F} \left( \frac{a}{b} \right). \quad (2-19)$$

In equation (2-19), Nu is Nusselt number, a non-dimensional coefficient of heat transfer,  $D_h$  is the hydraulic diameter,  $k_f$  is the fluid thermal conductivity, and the values of  $\mathcal{F}$  for different slenderness ratios, a/b, and geometries are tabulated in Table 2-2.

Table 2-2: Nusselt numbers for fully developed laminar flow in tubes of differing cross section [27]

Cross Section	$\frac{b}{a}$	$Nu = \frac{\bar{h}_{conv} D_h}{k_f}$		$C_f Re_{D_h}$
		Uniform heat flux	Uniform temperature	
	--	4.36	3.66	16

	1.0	3.61	2.98	14.25
	2.0	4.12	3.39	15.5
	4.0	5.33	4.44	18.25
	8.0	6.49	5.60	41
	$\infty$	8.23	7.54	24

For a fully developed turbulent flow with Prandtl number,  $Pr$ , however, the correlation developed by Dittus-Boelter [27],

$$Nu = 0.023Re_D^{4/5} Pr^{0.3} \left[ \begin{array}{l} 0.6 < Pr < 160 \\ Re_D > 10000 \\ \frac{L}{D} > 10 \end{array} \right], \quad (2-20)$$

is instead used to evaluate  $Nu$ . In equation (2-20),

the hydraulic-diameter based Reynolds number,  $Re_D$ , for a geometry with perimeter,  $P$ ,

and area,  $A$ , is defined as

$$Re_D = \frac{\rho u_{ch} D_h}{\mu}, \quad (2-21)$$

in which

$$D_h = 4 \frac{A_{ch}}{P_{ch}} \quad (2-22)$$

where  $A_{ch}$ , and  $P_{ch}$  are given by

$$A_{ch} = W_{ch} H_{ch}, \quad (2-23)$$

$$P_{ch} = 2(W_{ch} + H_{ch}), \quad (2-24)$$

respectively.

In equation (2-21),  $u$  is the channel average velocity and is calculated using the following equation

$$u_{ch} = \frac{\dot{m}_{ch}}{\rho A_{ch}}. \quad (2-25)$$

$\dot{m}_{ch}$  is the channel mass flow rate. For a known condenser configuration with  $n_{cond}$  of condenser cells, geometry, and plate spacing, when a demand mass flow rate is specified channel mass flow rate can be calculated as follows

$$\dot{m}_{ch} = \frac{\dot{m}}{n_{cond} n_{ch}}. \quad (2-26)$$

### *2.2.5. Phase Change Resistance*

Two condensation models were considered in this work: filmwise and dropwise condensation. While the former predominantly occurs on high surface energy condenser such as metals, without any surface manipulation, the latter is rarely observed in conventional steam condensers. Each mode of condensation is discussed in depth in the following sections.

#### 2.2.5.1 Filmwise Condensation

The first attempts to characterize film-wise condensation dates to Nusselt in 1916 [27].

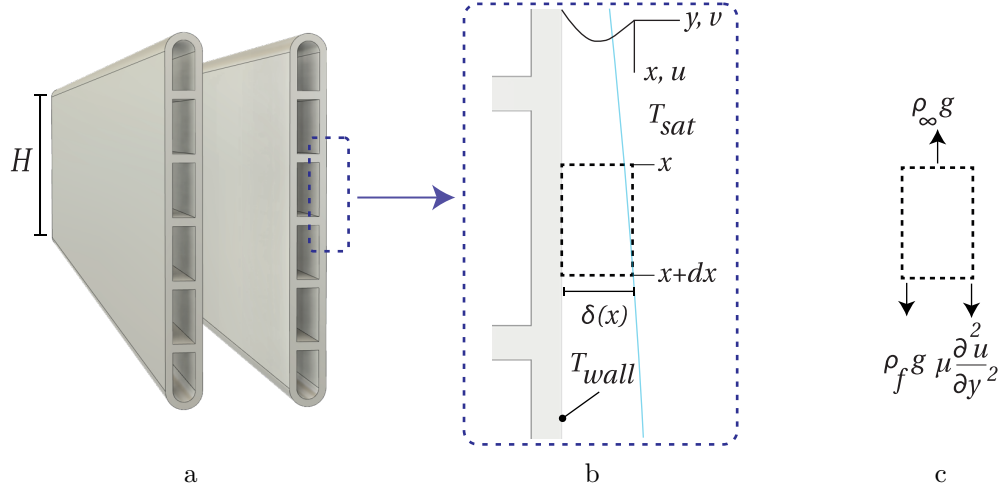


Figure 2-3. a) Multiport condenser plate. b) Control volume and coordinate system. c) Free body diagram.

Nusselt assumed the case of a laminar and constant properties liquid film, condensed on an isothermal-vertical flat plate in the presence of its pure isothermal and motionless vapor [27]. Nusselt's analysis ignored liquid film inertia, thermal advection, and liquid-vapor interface shear stress.

The following governing equation is a force balance drawn on fluid buoyancy and fluid viscosity based on Nusselt's assumptions (Figure 2-3.c).

$$\frac{\partial^2 u}{\partial y^2} = -\frac{g(\rho_f - \rho_{\infty})}{\mu}. \quad (2-27)$$

In equation (2-27),  $u$  is the component of liquid film velocity parallel to gravity,  $y$  is the perpendicular coordinate to the flat plate,  $g$  is the gravitational constant,  $\rho_f$  is the film density,  $\rho_{\infty}$ , is the vapor density, and finally,  $\mu$  is the film dynamic viscosity. Considering the assumption of no thermal advection and radiation, it can be shown that the heat transfer rate within the liquid occurs through conduction alone.

Using an integral analysis over the entire thickness of the liquid film to finding the local condensation rate can be shown to be

$$\overline{\text{Nu}}_H = \frac{\bar{h}_{phx}H}{k_f} = 0.943 \left[ \frac{\rho_f g (\rho_f - \rho_\infty) h_{fg} H^3}{\mu_f k_f (T_{sat} - T_s)} \right]^{\frac{1}{4}}, \quad (2-28)$$

in which  $h_{fg}$  is the latent heat of evaporation, and  $T_s$  is the wall temperature.

Later, Nusselt [28] and Rohsenow [29] showed that when relaxing the negligible thermal advection assumption, and including liquid subcooling,  $h_{fg}$  in equation (2-28) is replaced with a modified latent heat of evaporation given by:

$$h'_{fg} = h_{fg}(1 + 0.68\text{Ja}), \quad (2-29)$$

where Ja is the Jacob's number, defined as the ratio of sensible heat change in the liquid film to latent heat of vaporization,

$$\text{Ja} = \frac{c_{p,f}(T_{sat} - T_{wall})}{h_{fg}}. \quad (2-30)$$

Sparrow et al. [30] further relaxed the assumption of negligible inertia and, in giving the problem a boundary-layer treatment, found that their solution is different from equation (2-28) by a pre-factor. While the pre-factor drastically influenced the condensation characteristic under high Ja number and low  $\text{Pr}_f$  values, it had no effect under low Ja irrespective of the  $\text{Pr}_f$ .



Under common operating condition in water desalination, the values of Ja are close to zero. Hence, the original Nusselt analysis remains a valid model to evaluate phase change heat transfer coefficient in filmwise condensation.

Once the area-averaged phase change coefficient of heat transfer has been evaluated using equation (2-28), the corresponding phase change resistance can be calculated based on

$$R_{phx} = \frac{1}{\bar{h}_{phx,Y} A_{phx}}. \quad (2-31)$$

in which  $A_{phx}$  is the area on which condensation takes place. Dropwise Condensation

Due to high surface energy of metals, a drop of liquid water wets the metallic surface on which it is placed.

This wetting effect is not as extreme as it is for pure nonpolar liquids, such as alcohol and hydrocarbons, because polar liquids such as water have a higher surface tension compared to nonpolar liquids. Surface tension has been demonstrated to consist of two parts: dispersion forces, and metallic/hydrogen bond forces. London dispersion forces, also known as van der Waals forces are intermolecular forces present in any bond. Metallic forces are stronger than hydrogen bonds. For this reason, it is obvious why liquid metals have higher surface tension than water, which in turn has a higher surface tension than alcohol.

Although the wetting effect is not as extreme for water as it is for non-polar fluids such as alcohols, it is enough to form a film covering the entire condensation area under conventional condenser applications. Albeit thin, filmwise liquid thickness for low-thermal-conductivity substances such as water is the main cause of phase change

resistance. Lowering film thickness or preventing film formation altogether can remarkably boost condensation. The problem of surface wetting has been tackled with different methods through surface manipulation. Such attempts have mostly focused on increasing water-to-metal contact angle either through applying lower surface energy surfactant, such as an oil, or polymers such as tetrafluoroethylene, PTFE. Schmidt et al. discovered that surface microscale imperfections act as nucleation sites for dropwise condensation on which droplet nuclei formation is initiation [31]. These droplets further grow as the result of direct condensation onto them. Droplets continue to either individually grow or coalesce with the neighboring droplets until they are large enough for gravity to overcome their surface tension force. Under the influence of gravity, such droplets drain, merging with more droplets as they sweep the surface beneath them clean, and leaving a pristine droplet-free surface on which condensation will occur. This process has a lower average thermal resistance than that created in the case of filmwise condensation mainly due to lower effective condensate thickness and higher liquid-free surface. In fact, Rose points out that heat transfer experimental data suggest dropwise condensation and filmwise condensation are identical for metallic vapor condensation due to the significantly higher film thermal conductivity [32]. Dropwise condensation can be promoted by increasing surface contact angle, thereby reducing surface tension force. A surface with a contact angle below  $90^\circ$  is called hydrophilic, above  $90^\circ$  but below  $150^\circ$  is called hydrophobic, and above  $150^\circ$  is called superhydrophobic. By covering the high-surface-energy metal with a low-surface-energy material such as oil or polymer, the contact angle between water and the low-surface energy layer can be in excess of  $90^\circ$

degrees, thus creating a hydrophobic surface on which dropwise condensation can be promoted.

Thomas Young described the formation of water contact angle in terms of surrounding vapor, substrate and fluid surface energies [33]. Subsequent work done by Wenzel [34] and Cassie and Baxter [35] outlined the effect of surface microstructure on hydrophobicity. Contact angle hysteresis, the difference between an advancing (or growing) droplet's contact angle and a receding (shrinking) one's contact angle, was explored in depth by Dettre and Johnson [36]. Yaminsky proposed that contact angle hysteresis is due to contact-line pinning caused by surface roughness [37]. In conclusion, surface treatments which increase contact angle and decrease contact angle hysteresis tend to better promote dropwise condensation. As summarized by Enright et al. [38] a variety of surface modification has been demonstrated to give rise to dropwise conditions For example, self-assembled monomers which are atom-thick surface treatments demonstrate good hydrophobicity [39] [40] [41] [42]. In contrast, thicker polymer promoters such as Polytetrafluoroethylene, PTFE, and Polyphenylene Sulfide, PS exist [41]. Rare-Earth oxides such as cerium oxide, and lutetium oxide have been shown by Azimi et al. [43] to be intrinsically hydrophobic due to their unfilled  $4f$  orbitals which shields them from interactions with the surrounding environment by the full octet of electrons in the  $5s^2p^6$  outer shell. Microelectromechanical systems such as those described by Huang and Leu lead to hydrophobic surfaces [44]. Lee et al. [45] demonstrated the efficacy of laser irradiation surface preparation techniques to promote hydrophobicity.

Oils wear off during demanding operating conditions, and the benefits of thick enough PTFE coating to withstand such conditions have been found to offset the benefits reaped from dropwise condensation [32]. Over the past two decades, there have been several advances in creating superhydrophobic surfaces using a combination of two-tiered micro- and nano-structures in conjunction with a low surface energy coating to induce the Cassie state in condensing droplets [46]. Several studies have shown that condensation on such surfaces can lead to jumping droplets that can further refresh the surface of liquid and enhance condensation rates [47]. In other work, surfaces with lubricating oils impregnated within micro- and/or nanostructures have shown to cause mobility of the condensing droplets [48]. Such surfaces can potentially result in higher condensation rates than that obtained from a hydrophobic coating on a smooth surface. However, the process of formation of the structures is more involved and the ability to keep the surface clean is vital to its performance.

Regardless of how dropwise condensation is achieved, models to capture its heat transfer have assumed that heat transfer occurs via a range of hemispherical droplets through a series of resistances. Generally, four resistances are considered: vapor-liquid interfacial, capillary, conduction, and finally dropwise film promoter resistance. For resistances in series, temperature drop across any given droplet is equal to the sum of temperature drops due to each of such resistances,

$$T_{\text{sat}} - T_w = \Delta T = \Delta T_{fg} + \Delta T_{cap} + \Delta T_{cond} + \Delta T_p . \quad (2-32)$$

The interfacial temperature drop,  $\Delta T_{fg}$ , is due to net flux of liquid evaporating and vapor condensing at the interface from a hemispherical cap:

$$\Delta T_{fg} = \frac{q}{2h_{l-v}\pi r^2}, \quad (2-33)$$

where  $q$  is the heat flux of condensation, and  $h_{l-v}$  is interfacial coefficient of heat transfer which can be calculated based on the kinetic theory of gasses, from the following equation

$$h_{l-v} = \left( \frac{2\hat{\sigma}}{2 - \hat{\sigma}} \right) \frac{h_{fg}^2}{T_v v_l} \left( \frac{\bar{M}}{2\pi \bar{R} T_v} \right). \quad (2-34)$$

In equation (3-9)  $\hat{\sigma}$  is the accommodation factor, the fraction of vapor molecules making it through liquid-vapor interface,  $\bar{M}$  is the molecular weight of the vapor, and  $\bar{R}$  is the universal gas constant.

In equation (2-16)  $\Delta T_{cap}$  is the temperature difference between the liquid inside of the droplet, and the saturation temperature required by Young-Laplace to maintain the curvature of the droplet with radius  $r$ , and can be calculated as

$$\Delta T_{cap} = \frac{2v_l \sigma T_w}{h_{fg} r}. \quad (2-35)$$

The conduction induced temperature drop across the droplet is calculated based on

$$\Delta T_{cond} = \frac{q}{4\pi k_l r}. \quad (2-36)$$

and, the temperature drop due to the presence of a  $L_p$  thick promoter with thermal conductivity of  $k_p$  is calculated based on

$$\Delta T_p = q \frac{L_p}{k_p}. \quad (2-37)$$

Substituting equations (2-35), (2-35), and (2-36) into equation (2-32), the following equation emerges

$$\Delta T = \frac{2v_l \sigma T_w}{h_{fg} r} + \left( \frac{T_v v_l (2 - \hat{\sigma})}{4\pi r^2 \hat{\sigma} h_{fg}^2} \sqrt{\frac{2\pi \bar{R}}{\bar{M}}} T_v + \frac{1}{4\pi k_l r} \right) q \quad (2-38)$$

In their work, Rose, and his colleague Le Fevre devised a more generalized form of the above equation [23]. Combining the effect of pressure drop across interface for polyatomic gasses with the capillary effect, and modeling conduction through a right-angled cylinder they presented the following equation

$$\Delta T = \frac{2v_l \sigma T_w}{h_{fg} r} + \left( \frac{K_2 T_v v_l}{h_{fg}^2} \left( \frac{\hat{\sigma} + 1}{\hat{\sigma} - 1} \right) \sqrt{\frac{\mathcal{R}}{2\pi}} T_v + \frac{K_1}{k_l} r \right) q, \quad (2-39)$$

in which  $K_1, K_2$  are constant factors, and  $\mathcal{R}$  is the ideal gas constant.

Either equation (2-38) or (2-39) can be used to calculate the condensation heat transfer rate through a single droplet of known radius of  $r$ . To determine the condensation heat transfer rate from a range of droplets on the surface, one can integrate the single droplet heat flux over the droplet size range,

$$Q = \int_{r_{\min}}^{r_{\max}} q A(r) dr. \quad (2-40)$$

However, evaluation of equation (2-38) or (2-39) requires a knowledge of droplet size distribution. One such distribution suggested in the literature is of the form

$$A(r) = \frac{nr^{n-1}}{r_{\max}^n} \quad (2-41)$$

where  $A(r)$  is the area of the surface covered with a droplet of radius  $r$ , and  $n$  is a constant [23].

Solving for  $q$  in equation (2-40) and substituting equation (2-38), (2-41) into it the following equation for the heat of condensation is yielded

$$Q = n/r_{\max}^n \int_{r_{\min}}^{r_{\max}} \frac{\left( \Delta T - \frac{2\sigma v_l T_v}{r h_{fg}} \right)}{\frac{K_1 r}{k_l} + \frac{K_2 v_v T_v (\hat{\sigma} + 1)}{h_{fg}^2 (\hat{\sigma} - 1)} \sqrt{\frac{RT_v}{2\pi}}} r^{n-1} dr. \quad (2-42)$$

Evaluating this integral with the limits of integration of an arbitrary  $r_{\max}$ , and  $r_{\min}$ , as defined per equation (2-43), the entire heat of condensation can be calculated.

In equation (2-42),  $r_{\min}$  is usually taken to be the smallest thermodynamically stable droplet, i.e.:

$$r_{\min} = K_3 \left( \frac{\sigma}{\rho_l g} \right)^{\frac{1}{2}}, \quad (2-43)$$

where  $K_3$  is a constant determined as noted below.

A challenge of using this analytical derivation to determine the condensation heat transfer rate is its reliance on several constants. These constants have been evaluated to provide a best fit to a large body of steam data. A best fit was provided by the values of  $K_1 = \frac{2}{3}$ ,  $K_2 = \frac{1}{2}$ ,  $K_3 = 0.4$ , and  $n = \frac{1}{3}$  for steam at atmospheric pressure [23]. As pointed out by Graham and Griffith [49], the results of equation (2-42) heavily depend on the choice of  $r_{\max}$ , and a priori knowledge of the droplet distribution. On the topic of droplet size

distribution, the work of scholars such as Graham and Griffith [49] Maa [50], Abu-Orabi [51], measurements performed by Tanasawa and Ochiai [52] and Graham [53], and simulation work by Glicksman and Hunt [54] are in good agreement with the choice of exponent of 1/3 for the exponent n. Noteworthy is the fact that measurements of drop size were limited to droplets larger than about 8  $\mu\text{m}$ , and that simulations deviated from the assumed exponent for smaller droplet diameters. Graham and Griffith demonstrated that heat is transferred mostly by the smaller and undetectable droplets [49].

While it is true that the use of equation (2-38) is affected by the choice of many constants, and the derivation of which is arduous in close form, the following equation

$$h_{phx,dw} = T_v^{0.8}[5 + 0.3(T_v - T_{wall})], \quad (2-44)$$

suggested by Rose [23], derived from empirical data, is readily estimated, and is hence adapted in this work.

### 2.2.5.2 The Effect of Film Inundation

In a staggered condenser configuration, the condensate is driven by gravity from upper row of tubes or plates will impinge on the subsequent rows below potentially splashing some of the film formed on the bottom surface, and yet thickening it downstream of the surface. These competing effects are accounted for by the work of Murase [55] for the tube bank configuration in the form of following equation

$$\bar{h}_{phx,Y} = Y^{-1/6}\bar{h}_{phx,0}. \quad (2-45)$$



In this equation  $Y$  is the number of rows of plates stacked vertically,  $\bar{h}_{phx,Y}$  is the condenser-averaged phase change coefficient of heat transfer, and  $\bar{h}_{phx,0}$  is the area-averaged phase change coefficient of heat transfer for the topmost plate.

As the number of vertical plates decrease the average phase change heat transfer coefficient increases. This decrease in the number of vertical plates reduces the liquid film thickness at the bottom-most plate, and hence enhances the phase change heat transfer coefficient.

### *2.2.6. Channel Pressure Drop*

The pressure drop associated with fully developed internal flow results from a balance of pressure and wall shear forces, and can be calculated based the following equation

$$\Delta P = \frac{1}{2} f \rho v^2 L / D_h, \quad (2-46)$$

in which  $f$  is the Darcy friction factor,  $\rho$  is the fluid density,  $v$  is the area-averaged fluid velocity,  $L$  is the length of the channel. The friction factor,  $f$ , for a laminar flow is calculated by the last column in table 2-2 while considering that the Darcy friction factor is related to the Fanning friction factor,  $C_f$ , as

$$f = 4C_f, \quad (2-47)$$

For a turbulent flow, the friction factor is determined from the implicit correlation provided by Colebrook [27],

$$\frac{1}{\sqrt{f}} = -2 \log \left[ \frac{e/D_h}{3.7} + \frac{2.51}{Re_D \sqrt{f}} \right], \quad (2-48)$$

where  $e$  is the channel surface roughness.



# Chapter 3: Effect of Plate Spacing on Condensation



In the classic analysis performed on falling film condensation by Nusselt [56] he assumed no interfacial shear stress at the interface, i.e.  $\mu_f \frac{\partial u}{\partial y} |_{y=\delta} = 0$ . To include the effects of interfacial shear stress caused by vapor flowing in the direction of the condensate, shown in Figure 3-1.a), Rohsenow et al. [57] modified Nusselt's boundary condition to  $\mu_f \frac{\partial u}{\partial y} |_{y=\delta} = \tau_0$ , where the interfacial shear was assumed to be a constant value.

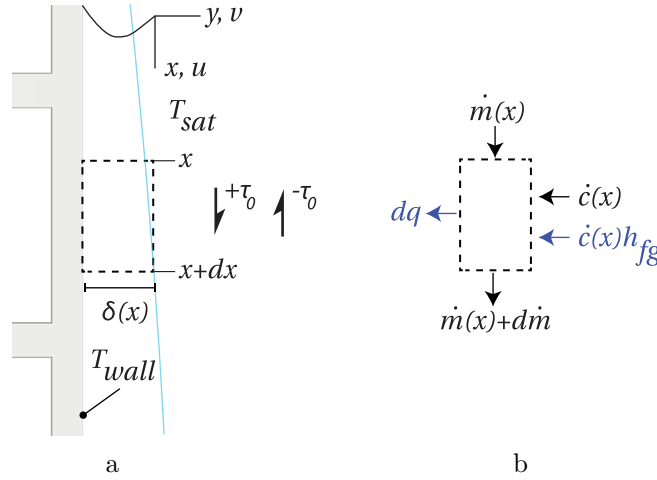


Figure 3-1. Front view of the proposed condenser. Vapor flow in a) counter-current, b) co-current configurations. c) Control volume and coordinate system. d) Conservation of mass diagram.

For a vapor flow in the opposite direction of the film condensate, the boundary condition was modified to  $\mu_f \frac{\partial u}{\partial y} |_{y=\delta} = -\tau_0$ .

Integrating equation (2-27) twice and using the following boundary conditions

$$u|_{y=0} = 0, \quad \mu_f \frac{\partial u}{\partial y} |_{y=\delta} = \pm \tau_0, \quad (3-1)$$

yields  $u$  for velocity defined as

$$u = \frac{g(\rho_f - \rho_s)}{\mu_f} \left( -\frac{1}{2}y^2 + \delta y \right) \pm \frac{\tau_0}{\mu_f} y. \quad (3-2)$$

Integrating this velocity profile over the thickness of the film, one can obtain the mass flow rate per unit depth at any location  $x$  along the plate,

$$\Gamma = \int_0^\delta \rho u dy = \rho_f \int_0^\delta \left[ \frac{g(\rho_f - \rho_s)}{\mu_f} \left( -\frac{1}{2}y^2 + \delta y \right) \pm \frac{\tau_0}{\mu_f} y \right] dy, \quad (3-3)$$

where the condensate mass flow rate per unit depth (plate length), given as

$$\Gamma = \dot{m}/L, \quad (3-4)$$

becomes

$$\Gamma = \rho_f \left[ \frac{(\rho_f - \rho_s)g}{3\mu_f} \delta^3 \pm \frac{\tau_0}{2\mu_f} \delta^2 \right]. \quad (3-5)$$

There are two unknowns in equation (3-5):  $\Gamma$ , and  $\delta(x)$ . The conservation of energy can be used to determine another expression with these two unknowns. Neglecting non-condensable effects, radiative heat transfer and thermal advection, (assuming a linear film temperature profile), heat transfer through the film must happen through conduction alone. For a control volume depicted in Figure 3-1.b this consequence translates to

$$dq = k \frac{T_{sat} - T_{wall}}{\delta} L dx = k_f \frac{\theta}{\delta} L dx, \quad (3-6)$$

where  $L$  is the plate length.

Additionally, forming a Taylor series expansion on the mass flow and neglecting higher order terms, we have

$$\dot{m}(x + dx) = \dot{m}(x) + d\dot{m}, \quad (3-7)$$

and from mass balance (Figure 3-1.b),

$$\dot{m}(x) + d\dot{m} = \dot{m}(x) + \dot{c}. \quad (3-8)$$

where  $\dot{c}$  is the control volume condensate flow rate in Figure 3-1.b.

Equation (3-8) implies that

$$d\dot{m} = \dot{c}. \quad (3-9)$$

Differentiating equation (3-4) and substituting it in equation (3-9) we have

$$\dot{c} = Ld\Gamma. \quad (3-10)$$

On the other hand, the conservation of energy considered for the control volume in Figure 3-1.d, indicates that the heat of condensation is linked to condensed mass through the latent heat of evaporation, i.e.:

$$\dot{c}h_{fg} = dq. \quad (3-11)$$

Combining equations (3-6) and (3-11) yields

$$\frac{d\Gamma}{dx} = k_f \frac{T_{sat} - T_w}{\delta h_{fg}}. \quad (3-12)$$

Chain differentiating equation (3-5) with respect to  $x$ , and noting that  $\delta = \delta(x)$ , yields

$$k_f \frac{T_{sat} - T_w}{\delta h_{fg}} = \rho_f \left[ \frac{(\rho_f - \rho_\infty)}{\mu_f} g \delta^2 \frac{d\delta}{dx} \pm \frac{\tau_0}{\mu_f} \delta \frac{d\delta}{dx} \right]. \quad (3-13)$$

which when combined with equation (3-12) and integrated with respect to  $x$  gives the following equation for condensate thickness

$$\frac{4k_f \mu_f \theta}{\rho_f (\rho_f - \rho_s) g h_{fg}} x = \delta^4 - \frac{4\tau_0}{3(\rho_f - \rho_s) g} \delta^3. \quad (3-14)$$

In equations (3-1)-(3-5) and (3-14) the  $\pm$  signs of the shear stress indicate the directionality of the interfacial shear stress.

Equation (3-14) is a quartic function of  $\delta$ , and as such it at most has four solutions, among which negative and imaginary solutions are not of interest. Expressing the roots in terms of the coefficients is an involved process, and hence explicit expressions of  $\delta$  in terms of  $\tau_0$  are difficult to obtain. However, for a given position  $x$  on the plate and an interfacial shear stress  $\tau_0$ , equation (3-14) can be numerically solved for liquid film thickness,  $\delta$ , and its positive and real resulting solution can be substituted in equation (3-12) to find the condensed mass at each control volume.

Defining the dimensionless parameters following Rohsenow [57]

$$\delta^* = \frac{\delta}{L_F}, \quad (3-15)$$

$$x^* = \left( \frac{H}{L_F} \right) \frac{4c_{p,l} \theta}{\text{Pr} h_{fg}}, \quad (3-16)$$

$$\tau_i^* = \frac{\tau_i}{L_F(\rho_f - \rho_s)g}, \quad (3-17)$$

and lastly

$$L_F = \left[ \frac{\mu_f^2}{\rho_f(\rho_f - \rho_s)g} \right]^{1/3}, \quad (3-18)$$

equation (3-14) becomes

$$x^* = \delta^{*4} + \frac{4}{3}\delta^{*3}\tau_i^*. \quad (3-19)$$

It can be shown that [46]

$$\overline{\text{Nu}} = \frac{\overline{h_F}L_F}{k_f} = \frac{4}{3}\frac{\delta^{*3}}{x^*} + 2\frac{\delta^{*2}\tau_i^*}{x^*}, \quad (3-20)$$

$$\text{Re}_L = \frac{4}{3}\delta^{*3} + 2\delta^{*2}\tau_i^*. \quad (3-21)$$

In evaluation of interfacial shear stress, Carpenter et al. [58], have suggested the coefficient of skin friction, but have refrained from any further discussions. If the velocity profile of the flowing vapor is known one could evaluate the interfacial shear stress by finding the velocity gradient at the liquid-vapor interface.

Vapor flows inside the vapor space, the space created by any two adjacent condenser plates (Figure 2-3.a), and condenses. This condensation of the vapor has two effects. First, it causes freestream velocity variation along the condenser plate, and second, it reduces the local vapor pressure and consequently the saturation temperature. Reduced local saturation temperature can lead to lower condensation rates, equation (3-12), and variation in local shear stress can alter local condensation values, equation (3-13).

In this chapter the effect of plate spacing on the condensation rate induced due to local saturation pressure and shear stress variation is studied.



## 3.1. Variable Interfacial Shear Stress

As steam flows over the condensing plates, it loses some of its mass due to condensation. This loss of mass slows steam, and thereby reduces steam-liquid shear stress, which is why a constant interfacial shear stress may not be an appropriate assumption.

In pursuit of finding the interfacial shear stress, the steam flow problem is divided into two parts. Initially the flow was modeled as flow over a flat plate with pressure gradient and suction, and when the boundary layers from adjacent plates merged, the flow was treated as an internal flow with suction.

### 3.1.1. External Flow with Varying Pressure Gradient and Suction

Due to the lack of an analytical solution for the velocity profile for flow over a flat plate with appropriate suction profile relative to this problem, a 3<sup>rd</sup> order polynomial velocity profile

$$u = u_{\infty} \frac{\frac{3}{2}\lambda_e - \frac{1}{2}\lambda_e^3 + \frac{\rho v \delta_s}{\mu} \left(\frac{3}{4}\lambda_e^2 - \frac{1}{2}\lambda_e^3\right) + \frac{\rho \delta_s^2}{\mu} \left(\frac{1}{4}\lambda_e - \frac{1}{2}\lambda_e^2 + \frac{1}{4}\lambda_e^3\right) \frac{\partial u_{\infty}}{\partial x}}{\frac{\rho v \delta_s}{4\mu_s} + 1}, \quad (3-22)$$

with  $\tau_{y=\delta_s} = 0$  according to table 4-4 in Nellis and Klein [59] was considered. In equation (3-22)  $u_{\infty}$  is the free stream velocity,  $v$  is the suction velocity at the wall, and  $\lambda_e$  is the external nondimensional length defined as

$$\lambda_E = \frac{\Delta/2 - y}{\delta_s} \quad (3-23)$$

where  $\delta_s$  is the steam boundary layer thickness, and  $y$  is the distance from centerline located at the middle of the two adjacent plates. (Figure 3-2.a)

Consequently, wall shear stress is given by

$$\tau_0 = \frac{\rho u_\infty \mu \delta_s^2 \frac{du_\infty}{dx} + 6u_\infty \mu_s^2}{(\rho v \delta_s^2 + 4\mu_s \delta_s)}. \quad (3-24)$$

Through a momentum integral analysis, it can be shown that to calculate the shear stress at any location  $x$  along the height of the plate expression

$$\begin{aligned} \frac{dB}{dx} + \frac{du_\infty}{dx} \left[ -\frac{\delta u_\infty \left( -\rho \delta_s^2 \frac{du_\infty}{dx} + 6\rho v \delta_s + 18\mu_s \right)}{12(4\mu + \rho v \delta_s)} \right] + v u_\infty \\ = -\frac{\rho u_\infty \mu_s \delta_s^2 \frac{du_\infty}{dx} + 6u_\infty \mu_s^2}{\rho(\rho v \delta_s^2 + 4\mu_s \delta_s)} \end{aligned} \quad (3-25)$$

where

$$\begin{aligned} B_i \\ = -\frac{\delta_{s,i} u_{\infty,i}^2 [-4\rho^2 \delta_{s,i}^4 \left( \frac{u_{\infty,i+1} - u_{\infty,i}}{\Delta x} \right)^2 + 9\rho_s^2 v_{s,i} \delta_{s,i}^3 \frac{u_{\infty,i+1} - u_{\infty,i}}{\Delta x} u_{\infty,i}]}{420(4\mu_s + \rho_s v_i \delta_{s,i})^2} \\ - \frac{\delta^2 \left( 54\rho_s^2 v^2 - 12\mu_s \rho \frac{du_\infty}{dx} \right) + 486\mu_s \rho_s v \delta_s + 936\mu_s^2}{420(4\mu_s + \rho_s v \delta_s)^2}, \end{aligned} \quad (3-26)$$

should be calculated. [59]

The pressure drop along the vapor space is given by

$$\frac{dp}{dx} = -\rho_s u \frac{du_\infty}{dx}. \quad (3-27)$$

The vapor space free stream velocity is equal to

$$u_\infty = \frac{\dot{m}}{\rho_s L \Delta}. \quad (3-28)$$

in which  $\dot{m}$  is the locally-varying mass flow rate inside the vapor space,  $L$ ,  $\Delta$  are the plate length and space respectively.

### 3.1.2. Internal Flow with Varying Pressure Gradient and Suction

For the internal flow section, a quadratic velocity profile was considered and evaluated at

$$\lambda = 1; u = 0, \lambda = 0; u = u_0, \frac{\partial u}{\partial y} = 0, \quad 29$$

which resulted in

$$\frac{u}{u_0} = -\lambda_I^2 + 1, \quad (3-30)$$

where  $u_0$  is the centerline velocity, and  $\lambda_i$  the internal nondimensional length as defined

$$\lambda_I = \frac{y}{\Delta/2}. \quad (3-31)$$

It can be shown<sup>1</sup> that the steam shear stress is given by

$$\tau_{0,i} = -\frac{4\mu_s u_0}{\Delta}. \quad \text{eq(3-32)}$$

The pressure drop along the vapor space by

$$\frac{dp}{dx} = \frac{26}{15} u_0 \rho_s \frac{du_0}{dx} + \frac{2\rho_s}{\Delta} u_0 v - \frac{2}{3} \mu_s \frac{d^2 u_0}{dx^2} + 8\mu \frac{u_0}{\Delta^2}, \quad (3-33)$$

---

<sup>1</sup> For detailed derivations refer to appendix II

and lastly, the centerline velocity by

$$u_0 = \frac{3}{2} \frac{\dot{m}}{(\Delta - \delta_l)\rho_s L} \quad (3-34)$$

## 3.2. Local Saturation Temperature

The local saturation temperature driving the local condensation rate is calculated based on the Clausius-Clapeyron equation

$$T_{sat} = \frac{h_{fg}}{R_g} \ln \left[ \frac{P_{sat}}{P} \right] + T, \quad (3-35)$$

where  $R_g$  is steam gas constant,  $P$ , and  $T$ , are reference saturation pressure and temperature equal to 100 °C, and 101.325 kPa respectively, and  $P_{sat}$  and  $T_{sat}$  are the local saturation pressure, and saturation temperature in order.

## 3.3. Solution Procedure

Neither of the velocity profiles have analytical solution, and hence a numerical solution is sought. Steam can either enter the condenser space from the top and flow alongside the condensate creating a co-current flow or enter from the bottom and flow against the condensate film causing a counter-current flow. As a preliminary analysis in this work the case of co-current was considered.

The height of the plate was divided into  $n$  equal  $dx$  tall control volumes (Figure 3-2.a), and equations (3-25),(3-27),(3-28), and eq(3-32)-(3-34) were discretized as following for the  $i^{th}$  control volume for the external flow condition,

$$\frac{B_{i+1} - B_i}{dx} + \frac{u_{\infty,i+1} - u_{\infty,i}}{dx} \left[ \frac{\overline{\delta_{s,i}} \overline{u_{\infty,i}} \left( -\rho \overline{\delta_{s,i}^2} \frac{u_{\infty,i+1} - u_{\infty,i}}{dx} + 6\rho \overline{v_i} \overline{\delta_{s,i}} + 18\mu_s \right)}{12(4\mu + \rho v_i \overline{\delta_i})} \right] \quad (3-36)$$

$$+ \overline{v_i} \overline{u_{\infty,i}} = - \frac{\rho \overline{u_{\infty,i}} \mu \overline{\delta_{s,i}^2} \frac{u_{\infty,i+1} - u_{\infty,i}}{dx} + 6 \overline{u_{\infty,i}} \mu_s^2}{\rho(\rho \overline{v_i} \overline{\delta_{s,i}^2} + 4\mu_s \overline{\delta_{s,i}})}, \quad (3-37)$$

$$\tau_{0,i} = \frac{\rho \overline{u_{\infty,i}} \mu \overline{\delta_{s,i}^2} \frac{u_{\infty,i+1} - u_{\infty,i}}{dx} + 6 \overline{u_{\infty,i}} \mu_s^2}{\rho \overline{v_i} \overline{\delta_{s,i}^2} + 4\mu_s \overline{\delta_{s,i}}}, \quad (3-37)$$

$$P_{i+1} = P_i - \frac{1}{2} \rho_s (u_{\infty,i+1}^2 - u_{\infty,i}^2), \quad (3-38)$$

$$u_{\infty,i} = \frac{\dot{m}_i}{\rho_s (\Delta L)}, \quad (3-39)$$

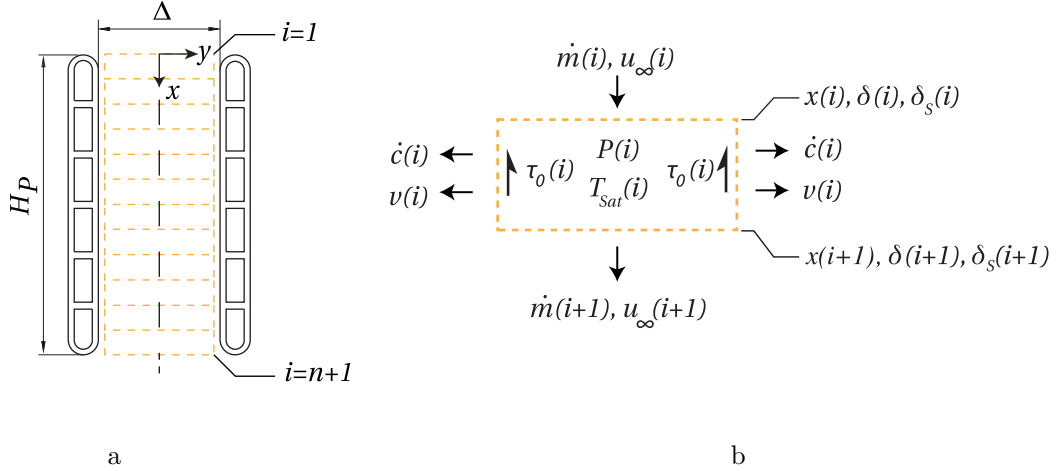


Figure 3-2. a. discretization of the vapor space along the vertical axis into  $n$   $dx$  tall and  $\Delta$  wide control volumes. b. Steam control volume

$$\tau_{0,i} = - \frac{4\mu_s u_{0,i}}{\Delta}, \quad (3-40)$$

$$P_{i+1} = P_i + \frac{26}{15} \overline{u_{0,i}} \rho_s (u_{0,i+1} - u_{0,i}) + \frac{2\rho}{\Delta} \overline{u_{0,i} v_{\frac{\Delta}{2},i}} dx$$

$$- \frac{2}{3} \mu_s \frac{u_{0,i-1} - 2u_{0,i} + u_{0,i+1}}{dx} + 8\mu \frac{\overline{u_{0,i}}}{\Delta^2} dx$$
(3-41)

$$u_{0,i} = \frac{3}{2} \frac{\dot{m}_i}{\rho_s (\Delta L)}$$
(3-42)

for the internal flow. In equation (3-36) (3-42) the bar operator,  $\overline{\phantom{x}}$ , indicates the current and next control volume averaged value, i.e.

$$\overline{X_i} = \frac{X_i + X_{i+1}}{2}$$
(3-43)

In equations (3-42)(3-39) liquid thickness,  $\delta_{\ell,i}$ , is neglected.

Vapor mass flow rate along the vapor space is updated as

$$\dot{m}_{i+1} = \dot{m}_i - 2\dot{c}_i,$$
(3-44)

and the suction velocity is calculated as

$$v_i = \frac{\dot{c}_i}{\rho_f L dx}$$
(3-45)

Discretized conservation of energy and momentum balance derived earlier, equation (3-13), takes the form of when the change in the interfacial shear stress is also considered

$$k_f \frac{T_{sat,i} - T_w}{\overline{\delta_{\ell,i}} h_{fg}} = \rho_f \left[ \frac{(\rho_f - \rho_s)}{\mu_f} g \overline{\delta_{\ell,i}^2} \frac{\delta_{\ell,i+1} - \delta_{\ell,i}}{dx} \right.$$

$$\left. - \frac{\tau_{0,i}}{\mu_f} \overline{\delta_{\ell,i}} \frac{\delta_{\ell,i+1} - \delta_{\ell,i}}{dx} \frac{\delta_{\ell,i}^2}{2\mu_f} \frac{\tau_{0,i+1} - \tau_{0,i}}{\Delta x} \right],$$
(3-46)

the control volume condensed mass is given by

$$\dot{c}_i = k_f \frac{T_{sat,i} - T_w}{\delta_{\ell,i} h_{fg}}, \quad (3-47)$$

and the local saturation temperature is computed using

$$T_{sat,i} = \frac{h_{fg}}{R_g} \ln \left[ \frac{P_i}{P_\infty} \right] + T_\infty. \quad (3-48)$$

The numerical problem mathematically described by set of equations (3-36)-(3-42) and (3-44)-(3-47) is solved for the following set of boundary

$$\begin{aligned} \delta_1 = \delta_{s,1} = B_1 = u_{0,1} = 0, \\ \tau_{0,n+1}, \dot{m}_{n+1} = 0, \end{aligned}$$

and prescribed

$$T_\infty, P_\infty, L, H, \Delta, n$$

conditions.

Neglecting natural convection, the flow inside of the vapor space is purely condensation driven. This suggests that, at steady state, for a strict co-current flow any steam entering the vapor space must condense completely on the plates, with no mass leaving the last control volume i.e.  $\dot{m}_{n+1} = 0$ . In other words, only as much vapor as can be condensed is drawn into the vapor space between the plates.

The mathematical system of equations was solved in EES, but the following procedure is useful in understanding the results. To solve this model, an initial inlet mass flow rate,  $m_1$ , is assumed, and flow attributes including the growth of vapor-boundary layer,  $\delta_{s,i}$ , were calculated and tracked using equations pertaining to external flow as set forth in section 3.1.1. When the boundary layer thickness exceeded half of the vapor space

width,  $\delta_{s,i} > \Delta/2$ , the vapor flow was treated as an internal flow with suction, and the forward flow attributes were updated using the internal flow equations described in 3.1.2. The resulting  $\dot{m}_{n+1}$  was compared to zero, and if their differences was within  $10^{-15}$  the procedure ended. Otherwise, the initial inlet mass flow rate was updated, and the system was solved to achieve the  $\dot{m}_{n+1} = 0$  boundary condition. Steam properties were evaluated at  $T_{sat}, P_{sat}$  while liquid properties were kept at film temperature, defined as the average of  $T_{sat}$  and  $T_w$ , or  $T_{sat} - \frac{1}{2}\Delta T_{sub}$ .

### 3.4. Results and Discussions

The results of the discretized mathematical model for fixed shear stresses,  $\tau_0$ , 1 m long plate spacing, and varied plate heights were cast in the form of  $Re_L$  and  $\tau_0^*$ , and compared to the results of the exact solution of Rohsenow (equations (3-20) and (3-21)) [57]. The results are shown in Figure 3-3 as non-dimensional average heat transfer coefficient as a function of Reynolds number for various imposed shear stress. Solid lines correspond to Rohsenow's exact solution, and the solid squares indicate the discretized model results. An excellent match between the model and analytical results is observed with and without vapor-imposed shear.



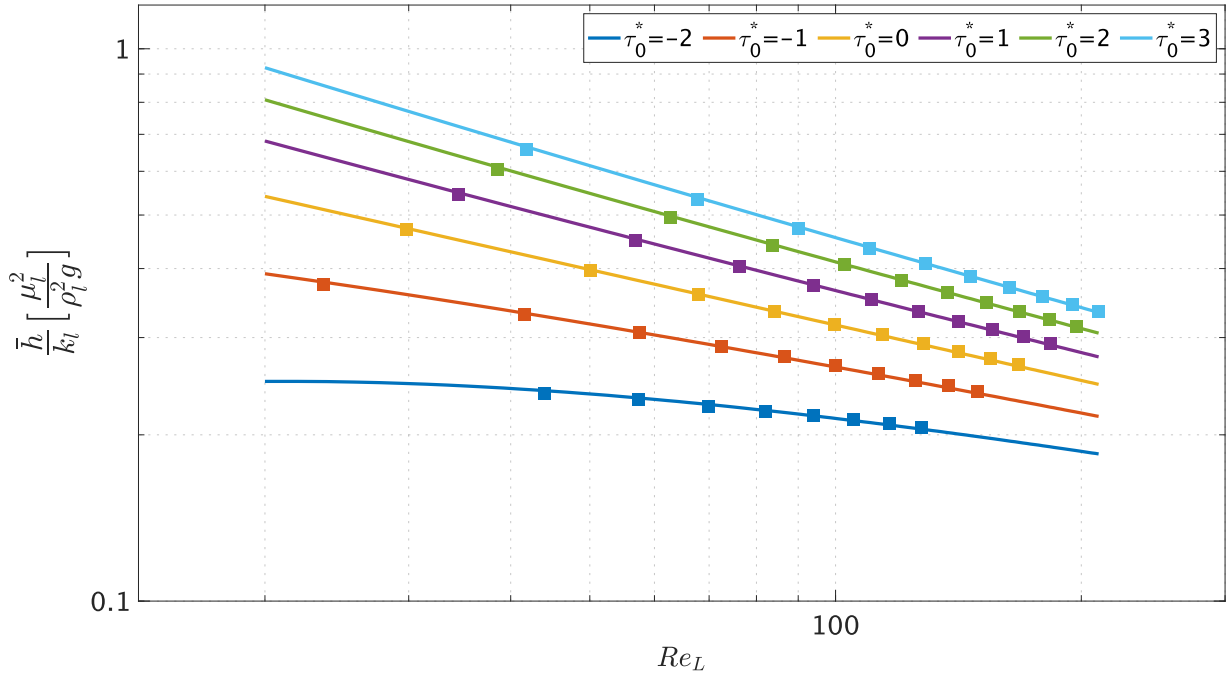


Figure 3-3. Nondimensional plate-height-averaged coefficient of heat transfer,  $\bar{h}$ , vs film-wise Reynolds number,  $Re_L$ , at different nondimensional shear stress,  $\tau_0^*$ . Continuous lines represent Rohsenow's exact solution, while the solid squares correspond to the discretized mathematical numerical solution with  $n = 200$ , and  $\Delta = 1m$

Prescribed conditions were varied as indicated in Table 3-1 and their corresponding effects on total condensation, coefficient of phase change heat transfer, as well as subcooling reduction are plotted in Figures 3-4 - 3-6.

Table 3-1: Prescribed conditions, and their variation

Prescribed Condition	Values	Unit
Vapor space width	1, 4, 6, 10, 100, 1000	mm
Height of plate	3-30	cm
Steam bulk temp	40, 60, 80, 100	°C
Subcooling	4, 8, 12	K

Clausius-Clapeyron state equation indicate that the rate at which saturation temperature reduces for a fixed saturation pressure reduction is increases as the initial saturation pressure hence saturation temperature reduces. For this reason, the results of the lowest

bulk temperature, the most extreme case, obtained from the current analysis is presented and discussed here.<sup>2</sup>

In preparation of the results, the following definitions were used:

$$\bar{h}_d = \frac{1}{H_p} \sum_{i=1}^{n+1} \frac{k_f}{\delta_i} dx, \quad (3-49)$$

$$\Delta\bar{T} = \frac{1}{H_p} \sum_{i=1}^{n+1} (T_{sat,i} - T_w) dx, \quad (3-50)$$

$$q_{\tau_0,P} = \frac{1}{H_p} \sum_{i=1}^{n+1} \frac{k_f}{\delta_i} (T_{sat,i} - T_w) dx, \quad (3-51)$$

in which  $\bar{h}_d$ ,  $\Delta\bar{T}$ , and  $q_{\tau_0,P}$  are the plate-height averaged coefficient of heat transfer, subcooling, and condensation heat flux respectively.

---

<sup>2</sup> The rest of subcooling results are presented in the appendix III

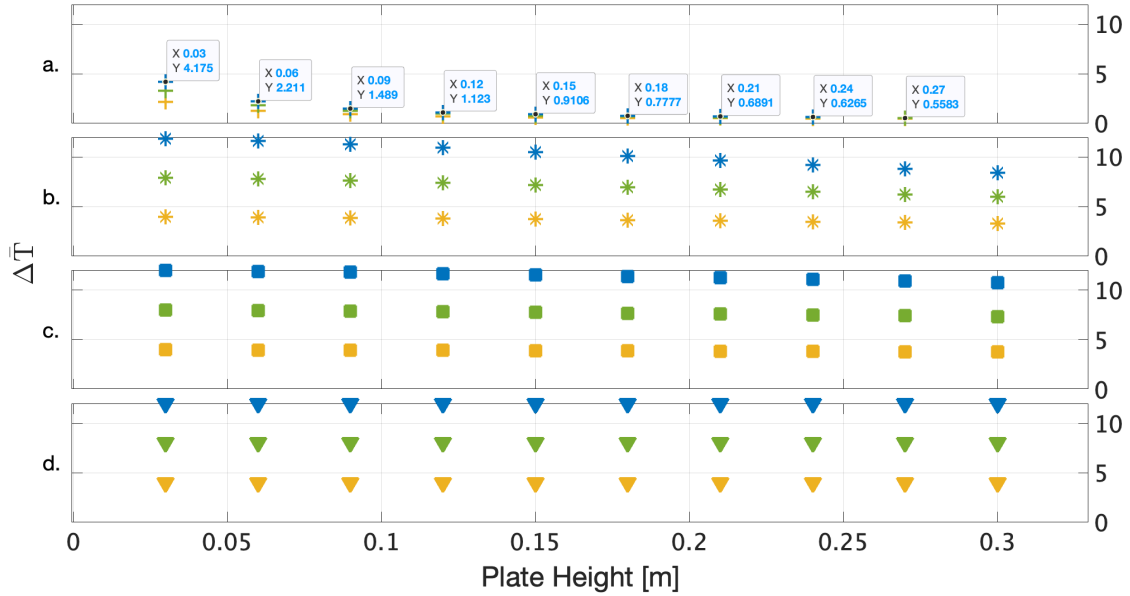


Figure 3-4: Effect of varied plate spacing of a. 1mm, b. 6mm, c. 10 mm, d. 1000 mm, plate height, and subcooling on plate-height averaged subcooling for  $n = 200$ ,  $T_{sat} = 40^\circ\text{C}$ . Mustard, green, and blue shapes represent 4, 8, and 12 K subcooling respectively.

For all the studied conditions averaged subcooling either stays the same or is reduced (Figure 3-4).

As observed in Figure 3-4.a, and especially in b, although the length-averaged subcooling reduces irrespective of the subcooling, the difference between any two length-averaged subcoolings remains the same. Subcooling reduction decreases with increased plate spacing, and in the case of 1 m plate spacing it is completely absent.

By observing the case 6 mm plate spacing it is evident that as the plate spacing height increases averaged subcooling reduces, and it appears that an infinitely long plate, for any plate spacing, will eventually reduce the local subcooling to near zero (Figure 3-4.b). This is substantial in the extreme case of 1mm plate spacing in which the length-averaged subcooling reduces to near zero at 30mm (Figure 3-4.a).

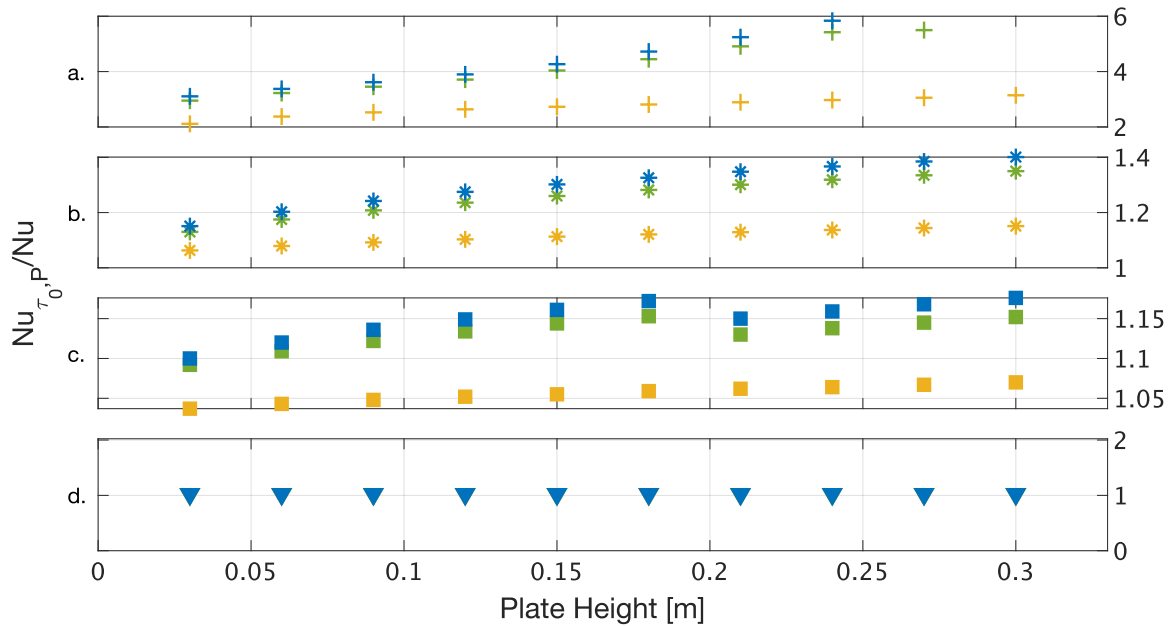


Figure 3-5: Effect of varied plate spacing of a. 1mm, b. 6mm, c. 10 mm, d. 1000 mm, plate height, and subcooling on Nusselt number ratio for  $n = 200$ ,  $T_{sat} = 40^\circ\text{C}$ . Mustard, green, and blue shapes represent 4, 8, and 12 K subcooling respectively.

The results of the plate length averaged Nusselt number are divided by the original Nusselt numbers and presented in Figure 3-5 against plate height. The Nusselt number ratio increases with plate height for all the 1, 6, 10 mm cases irrespective of subcooling, although the increase is larger for higher subcooling at any plate height. The 8K trails the 12K results more so than 4K results follow 8K. Nusselt ratio is the same for any plate height as long as the plates are placed at least a meter apart, i.e. in Figure 3-5.d Nusselt number ratios are equal to unity, and subcooling results overlay each other. Overall, the Nusselt number ratio is greater or equal to one. This indicates that, at any subcooling, plate height, and plate spacing, there is an enhancement in area-averages Nusselt number, or coefficient of phase change heat transfer. To understand this increase, it is helpful to consider equation (3-14), a more compact form of equation (3-46). Effective subcooling reduces, making the left-hand side of equation (3-14) smaller. On the other hand, presence

of positive shear stress adds a positive term to the right-hand side of equation (3-14). This combined effect of reduced subcooling, and the presence of a positive shear stress, lowers the film thickness which is inversely proportional to the local coefficient of heat transfer.

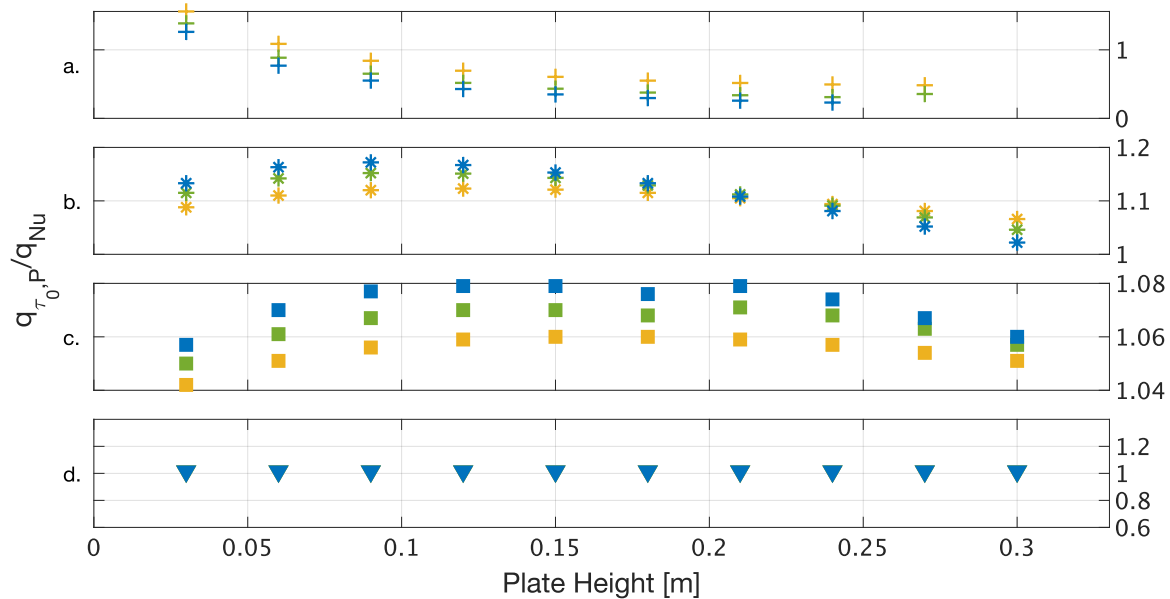


Figure 3-6: Effect of varied plate spacing of a. 1mm, b. 6mm, c. 10 mm, d. 1000 mm, plate height, and subcooling on heat of condensation ratio for  $n = 200$ ,  $T_{sat} = 40^\circ\text{C}$ . Mustard, green, and blue shapes represent 4, 8, and 12 K subcooling respectively.

The sum of the product of the local subcooling and liquid thickness is calculated and divided by the height of the plate to calculate the length averaged heat flux of condensation. The ratio of this number to the flux of condensation achieved using the original Nusselt number is calculated and shown on the ordinate in Figure 3-6. The ratio remains unity for all plate heights, and subcoolings in the case of 1m spaced plates (Figure 3-6.d). The 10-mm spaced condenser plates have slightly higher condensation values than Nusselt prediction, and an increase of about 4% to 8% in heat of condensation is observed.

The condensation ratio appears to have a local maxima in the neighborhood of plate height equal to 18-cm for all of the subcoolings in the 10 mm spacing case.

For the case of 6 mm plate spacing, 11% is the highest condensation improvement and is observed for a 9 cm tall plate operated at 12K subcooling. Although at 1 mm plate spacing, for a 3-cm-tall-plate, condensation is improved by 20-30%, despite having the highest favorable shear stress, such tight plate spacing has an adverse effect on condensation so much so that condensation is reduced by a factor 3 for the 28-cm tall plate at 8K subcooling.

Subcooling is a determining factor in the heat flux of condensation ratio with higher subcooling corresponding to higher ratios at any plate height in the 6 mm plate spacing case, but this effect reverses at plate height of 21 cm in the 4 mm plate spacing case (Figure 3-6.b), and continues to remain true for the entire case of 1 mm plate spacing (Figure 3-6.a).

For the 1 mm plate spacing no solutions converged for the 30-cm tall plate at any subcooling, neither were any solutions obtained for the 28-cm tall condenser at 12K subcooling.

### **3.5. Chapter Conclusions**

In this chapter the effect of plate spacing on condensation for different plate height, subcooling, and bulk temperature was numerically investigated. The problem of condensation over a flat plate in presence of favorable vapor shear stress caused by co-

current steam flow as well as condensation-induced saturation temperature reduction is considered.

The following are salient chapter results

1. Local subcooling reduction becomes only important at lower bulk temperature cases
2. Compared to falling film values,
  - a. Averaged heat transfer coefficient improves compared to the original Nusselt calculation - (up to 6 times at 1 mm plate spacing)
  - b. Condensation flux reduces while Nusselt number increases for the 1 mm plate spacing
  - c. For all the case of 4, and 6 mm plate spacing
    - i. Plate-averaged subcooling reduces takes place
    - ii. Condensation flux improves when plate gap is reduced
  - d. For plates separated far enough, condensation-induced co-current flow does not affect condensation
3. In the realm of proposed MSF condensers,  $\Delta > 4$  mm,  $H_p < 9$  mm a condensation improvement of 15% is observed over Nusselt calculations.

This chapter considered only the co-current flow of steam inside the vapor space. In reality, vapor will enter the vapor space from either end, creating competing, co-current and counter-current flows. The extent to which a mode of flow takes place is dictated by the total pressure drop caused by that flow. It can be argued that a counter-current flow will have a lower condensation-induced pressure drop and hence dominate the flow.

Additionally, in an MSF flashing chamber, vapor flashes from the bottom and is most likely to enter the vapor space from the bottom, creating a counter-current flow scenario. Unlike the case for the co-current, a counter-current flow does not benefit from condensation-assisting shear stress, so the subcooling reduction observed here compounded with the adverse shear stress will lead to overall lower condensation fluxes. It is likely that the combined increase of condensation due to co-current flow and condensation reduction due to counter-current flow, for the proposed multiport mini channel condensers, will balance each other, and the values obtained from the original Nusselt number will be sufficient for modeling purposes.





# Chapter 4: Parametric Study of the MSF Condenser



In this section, a comparison of the performance of the compact condenser will be made relative to a conventional tube bank condenser shown in Figure 1-1. The model for the condenser was described in Section 2.2. In order to characterize the potential size reduction achieved through the adoption of a compact condenser, the desalination plant outlined in section 2.1, was used as baseline for this analysis.

The overall heat transfer conductance reported in table 3 for the tube bank was verified using the analytical model described in chapter 2, and taken as baseline value throughout the rest of this work.

It was assumed that the available condenser frontal area, plant thermal energy and brine input and distillate output are the same between the baseline tube bank and the minichannel multiport condenser. Frontal area is defined as the entire area occupied by the condenser package perpendicular to the direction of the flow. Equal condenser frontal area implies that  $W_{cc} \times H_{cc} = W_{tb} \times H_{tb}$ , see Figure 2-2.a, b. The intent was to determine the reduction in the condenser length achieved by the use of the compact condenser, and the impact on pressure drop, and hence pumping power.

For the given stage conditions, and the above set area constrain, using their corresponding appropriate equation, each resistance in equations (2-6)(2-7)(2-10)(2-31) can be calculated. The overall heat transfer coefficient in equation (2-5) can be subsequently estimated for both the baseline (bank of tubes) and the compact condenser.

Keeping the required energy input constant implies that energy recuperated across the condensers is equal i.e.

$$Q_{cc} = Q_{tb}, \quad (4-1)$$

where the subscripts cc, and tb denote compact condenser's and tube bank's attribute.

Using the log mean temperature difference formulation, equation (4-1) takes the following form

$$U_{cc}A_{cc}\Delta T_{lm,cc} = U_{tb}A_{tb}\Delta T_{lm,tb} \quad (4-2)$$

Understanding that for the same stage inlet, outlet, and steam temperature the log mean temperature is the same, equation (4-2) simplifies to

$$U_{cc}A_{cc} = U_{tb}A_{tb}. \quad (4-3)$$

Rewriting the heat exchanger area,  $A$ , in equation (4-3) in terms of the perimeter of a single tube or plate of the heat exchanger,  $P$ , multiplied by the number of heat exchanger elements,  $n$ , and finally by the length of the element, the area for the conventional and the compact condenser can be written as

$$A_{cc} = P_{cc}n_{cc}L_{cc}, \quad A_{tb} = P_{tb}n_{tb}L_{tb}, \quad (4-4)$$

Respectively where the equivalent length of compact condenser is obtained as

$$L_{cc} = \frac{U_{tb}P_{tb}n_{tb}}{U_{cc}P_{cc}n_{cc}}L_{tb}. \quad (4-5)$$

Defining dimensionless parameters for length,  $\Lambda$ , overall heat transfer coefficient,  $\Omega$ , packing density of tubes/plates,  $N$ , and perimeter ratio,  $\Gamma$ , respectively as

$$\Lambda = \frac{L_{cc}}{L_{tb}}, \quad \Omega = \frac{U_{cc}}{U_{tb}}, \quad N = \frac{n_{cc}}{n_{tb}}, \quad \Gamma = \frac{P_{cc}}{P_{tb}} \quad (4-6)$$

Equation (4-5) becomes

$$\Omega N \Gamma \Lambda = 1. \quad (4-7)$$

In equation (4-5) the quantities corresponding to the bundle of tubes are taken from table 2-1,  $U_{cc}$  is calculated from equation (2-5),  $P_{cc}$  depends on the choice of geometry, and  $n_{cc}$  is determined when a plate spacing is chosen.

Similarly, stage pressure drop ratio can be defined as

$$\Pi = \frac{\Delta P_{cc}}{\Delta P_{tb}} \quad (4-8)$$

In evaluation of equation (4-8) while the length of the tube bundle is known from plant technical data, minichannel condenser equivalent length needs to be evaluated.

Once the minichannel geometry and the plate spacing are determined, the corresponding minichannel condenser equivalent length,  $L_{cc}$ , and the stage pressure drop were found from equation (4-5), and (4-8).

The following subsections are a discussion on parametric variation and their impact on plant size, total pressure drop, and overall heat transfer change.

## 4.1. Plate Gap and Aspect Ratio

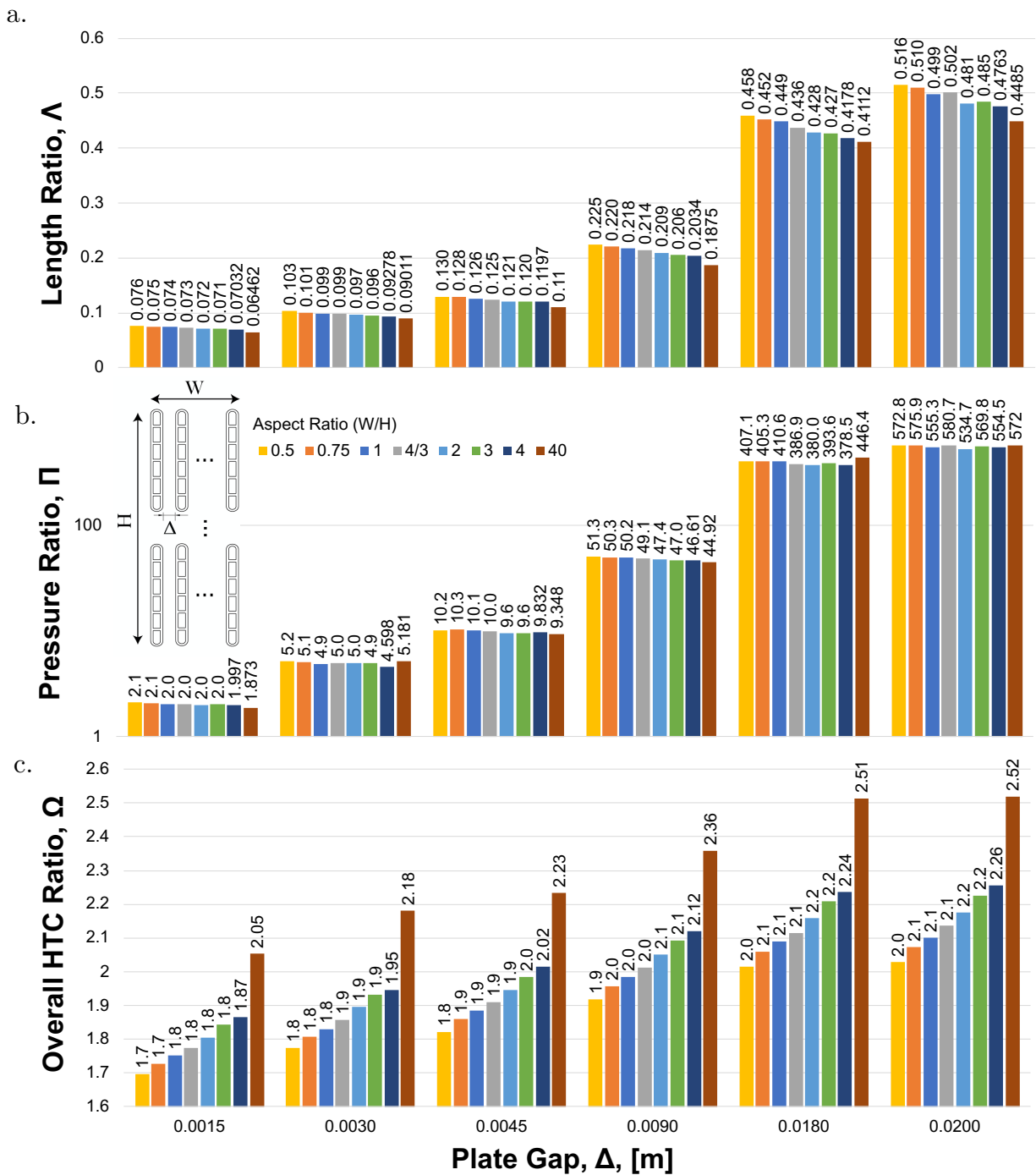


Figure 4-1. The effect of varied plate gap, and aspect ratio, on dimensionless a. length, b. pressure, and c. overall heat transfer coefficient

Due to the unknown factors pertaining to assembly, and footprint restriction of the proposed minichannel condensers, a sensitivity analysis varying condenser plate gap, and aspect ratio was performed.

The plate gap,  $\Delta$ , was varied from the minimum possible value, 1.5mm to 20mm. Additionally the aspect ratio,  $W/H$  was varied from 0.5 to 40 - this was done while fixing the available condenser footprint area  $W_{cc} \times H_{cc}$  to be identical to that of the conventional condenser.

The results of variation of compact condenser plate spacing,  $\Delta$ , and aspect ratio,  $W/H$ , on the non-dimensional length ratio, pressure drop ratio and overall heat transfer coefficient ratio,  $\Omega$ , are shown in Figure 4-1.a, b, and c respectively.

For any plate spacing,  $\Delta$ , the nondimensional overall heat transfer coefficient  $\Omega$  increases with increased in aspect ratio. (Figure 4-1.a) This effect is due to the fact that when going from an aspect ratio of 0.5 to 40, the number of plates stacked in the vertical direction decreases. Therefore, the interference of the falling film from the top row onto the next row is decreased as per equation (2-45), thereby resulting in an increase in the  $\bar{h}_{phx,Y}$ . While other resistances remained constant, this increase in  $\bar{h}_{phx,Y}$ , causes  $\Omega$  to increase. Other factors in equation (4-6) remaining constant, an increase in  $\Omega$  with varying  $W/H$  of the plate equates to a decrease in nondimensional length,  $\Lambda$ . For any given  $\Delta$ , the nondimensional pressure drop,  $\Pi$ , reduces slightly with aspect ratio (Figure 4-1.b). This reduction is a direct consequence of  $\Lambda$  reduction.

For any given aspect ratio, an increase in plate gap, reduced the number of plates, and hence caused higher internal fluid velocity inside the plates. This increased velocity

enhances the internal heat transfer coefficient and increases  $\Omega$ . On the other hand, the reduced number of plates decreases packing density. The competing effect of increased nondimensional heat transfer coefficient,  $\Omega$ , and decreased packing density,  $N$ , increases  $\Lambda$  in accordance with equation (4-7) (Figure 4-1.a). In contrast, the increased velocity inside each plate drastically increases the pressure drop across the minichannel condenser, which hence lead to large increases in the nondimensional pressure drop,  $\Pi$ ; indeed, the slight observed enhancement in  $\Lambda$  is not without adverse consequences to the increase in  $\Pi$ .

## 4.2. Effect of Condenser Material

Motivated to find alternative condenser material and manufacturing methods, the effect of the condenser material on the condenser parameters is analyzed in this subsection.

For stage vapor temperature of 59 °C, brine inlet temperature of 50 °C, plate spacing  $\Delta$  of 1 cm, and baseline aspect ratio, wall thermal conductivity was varied from that of Carbon Resin CE221, 0.167 W/m-K - a high temperature additively manufacturable plastic, to 10 W/m-K. Figure 4-2 depicts the results of varied wall thermal conductivity on nondimensional pressure drop, left ordinate, and nondimensional overall heat transfer coefficient, right ordinate.

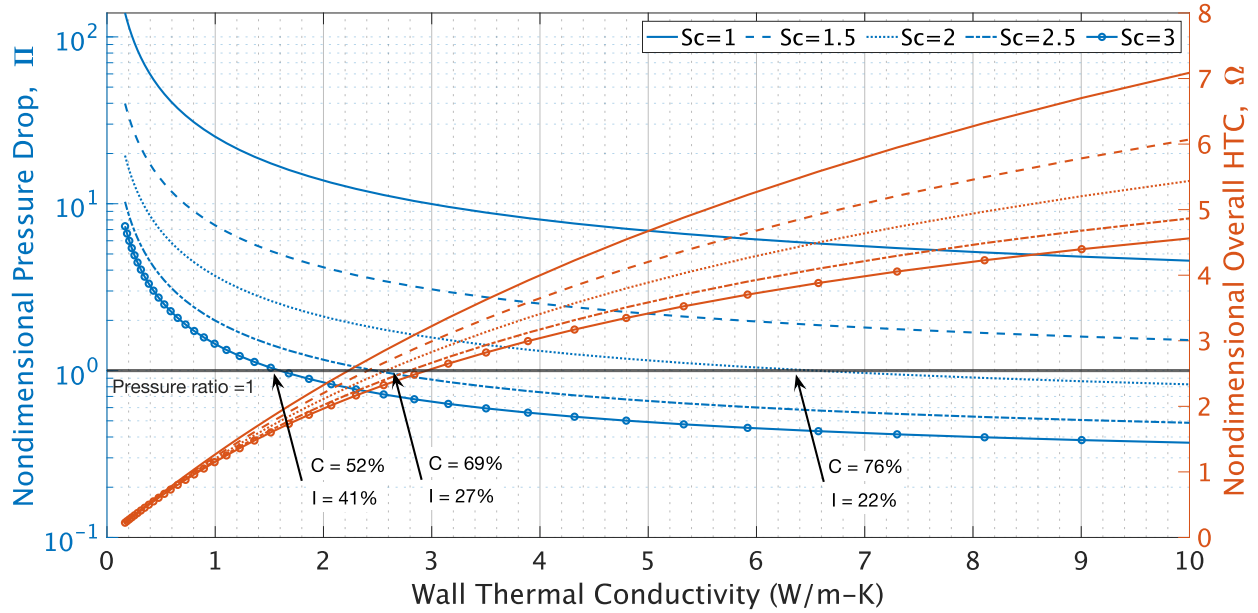


Figure 4-2. The effect of varied material thermal conductivity on condenser parameters for different scales.  $\Delta = 1 \text{ cm}$ ,  $T_v = 59 \text{ }^\circ\text{C}$ ,  $T_i = 50$ ,  $R_{\text{fouling,tube}} = 0.203 \text{ m}^2 - \text{k/kW}$ ,  $H_p = 4.3 \text{ mm}$ ,  $W_p = 1.8 \text{ mm}$ ,  $n_{\text{ch}} = 6$   $\Delta_p = 58 \text{ kPa}$ ,  $Th_w = 300 \text{ }\mu\text{m}$

For this analysis wall roughness was kept at zero for brine pressure drop calculation. it was assumed that for the compact condenser no fouling will occur on the inside and that condensation will occur as dropwise condensation.

From Figure 4-2 as the condenser material thermal conductivity increases so does the overall heat transfer coefficient, and hence  $\Omega$ . As in the cases discussed before, increased  $\Omega$  reduces the required heat transfer area, i.e  $\Lambda$ , which in turn reduces  $\Pi$ . Noting that the vertical axis for pressure drop is in logarithmic base, we observe that although  $\Omega$  increases with increased thermal conductivity its effect diminishes for larger values of thermal conductivity. A horizontal line with  $\Pi = 1$  is plotted, and its intersection with different pressure ratio for different aspect ratio is pointed to by arrows.



The significance of such intersects is that for any given scale, the thermal conductivity associated with the point indicates a minimum wall thermal conductivity requirement. In other words, a condenser obeying the initial assumptions set in this subsection and made from a material with the minimum thermal conductivity will provide the same product output for the same exact thermal, and electrical energy input. This minimum thermal conductivity is 1.6, 2.65, 6.4 W/m – K for scale ratio of 1, 1.5, 2 respectively. Plastics are good candidates that will not only inhibit fouling and corrosion, but also, due to their low surface energy, promote dropwise condensation. The problem with plastics, in general, is their low thermal conductivity. For example, one of highest thermal conductivity in plastics is found in high-density polyethylene with a thermal conductivity of 0.51 W/m – K, which is three folds smaller than the lowest minimum thermal conductivity found in this subsection.

At the tail end of the of intersection arrow, two values are reported: conduction resistance ratio, C, and internal resistance ratio, I. Conduction ratio is the wall thermal conduction resistance divided by the total thermal resistance, and the internal resistance ratio is the brine internal heat transfer resistance divided by the total thermal resistance. Absent fouling in this analysis, the sum of other three resistance is the total resistance, and hence them sum of the reported ratios subtracted from unity yields the phase change resistance ratio, Phx. In other words,  $Phx = 1 - CI$ . Phase change resistance is the same through this analysis, but larger scale condenser plates lead to lower internal flow rates, and hence higher internal resistance. That is why for any given wall thermal conduction overall heat transfer coefficient drops with increases scale ratio.

### 4.3. Dominant Resistance for Varied Fouling Resistance

To identify the dominant resistances, and due to the lack of sufficient data on the effect of increased brine velocity on fouling resistance, the effect of varied fouling resistance on the overall resistance we analyzed. The fouling resistance was varied from 0, no fouling, to that of one of the highest industry-reported values,  $0.1 \text{ m}^2 - \text{K/kW}$  [26]. indeed, the fouling thickness for the compact condenser might be different than the one reported for conventional bundle of tube exchangers, or even be negligible. The velocity inside the minichannel condenser is larger than the internal velocity of tubes. This increased velocity gives rise to higher shear stress at the walls, and is likely to thin the fouling layer, causing the fouling resistance to be lower than the maximum reported value.

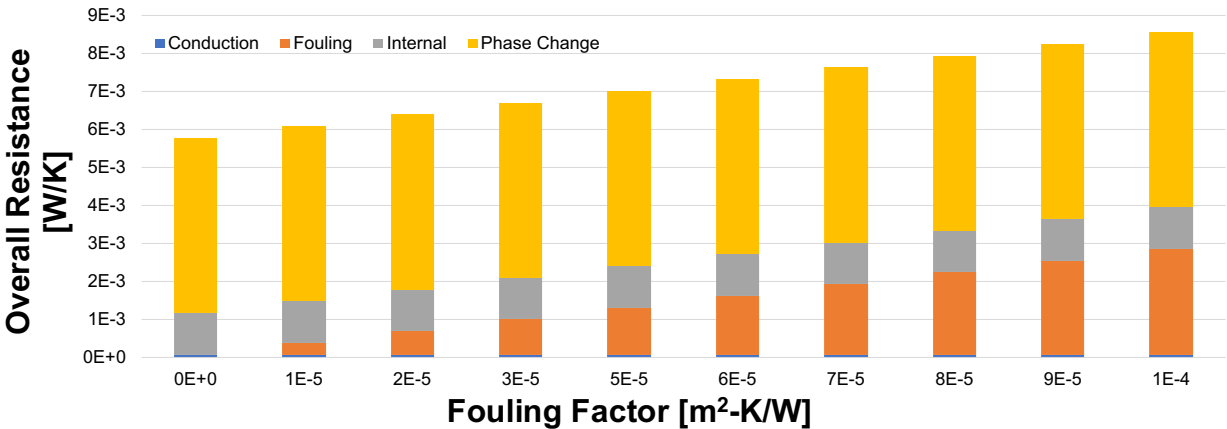


Figure 4-3. The effect of varied fouling resistance on overall resistance.

As we traverse along the direction of increasing fouling resistance, we notice that the overall resistance increases Figure 4-3. Among all the resistances conduction has the least

contribution, to resistance. Fouling resistances starts from no contribution at all, to almost matching to that of internal resistance at  $3 \text{ m}^2 - \text{K}/\text{kW}$ , beyond which it becomes the second most dominant resistance. An important note here is that, irrespective of the fouling resistance, phase change remains the dominant resistance. Figure 4-3 reveals that not only phase change resistance is the dominant resistance, but also that internal resistance does not substantially contribute to the overall resistance due to the reduction in single phase internal resistance by use of the minichannel geometry. This is one of the important motivating factors behind the proposed compact condenser and allows for further reduction in size by pursuing surface enhancements to reduce phase change resistance.

#### **4.4. Combined effect of phase change enhancement and channel size**

In this section, the impact of reducing phase-change resistance is presented. Since the baseline compact condenser has a higher pressure drop ratio,  $\Pi$ , in Figure 4-4. the channel dimensions were also varied to assess its impact on performance.

While keeping the stage conditions, fouling resistance, condenser material, and channel aspect ratio fixed at values noted in table 2-1, the minichannel condenser was scaled up to 2.5 times. Channel thickness was fixed at  $600 \mu\text{m}$ , and an aspect ratio of 4 was chosen. The plate gap was kept at 3mm.

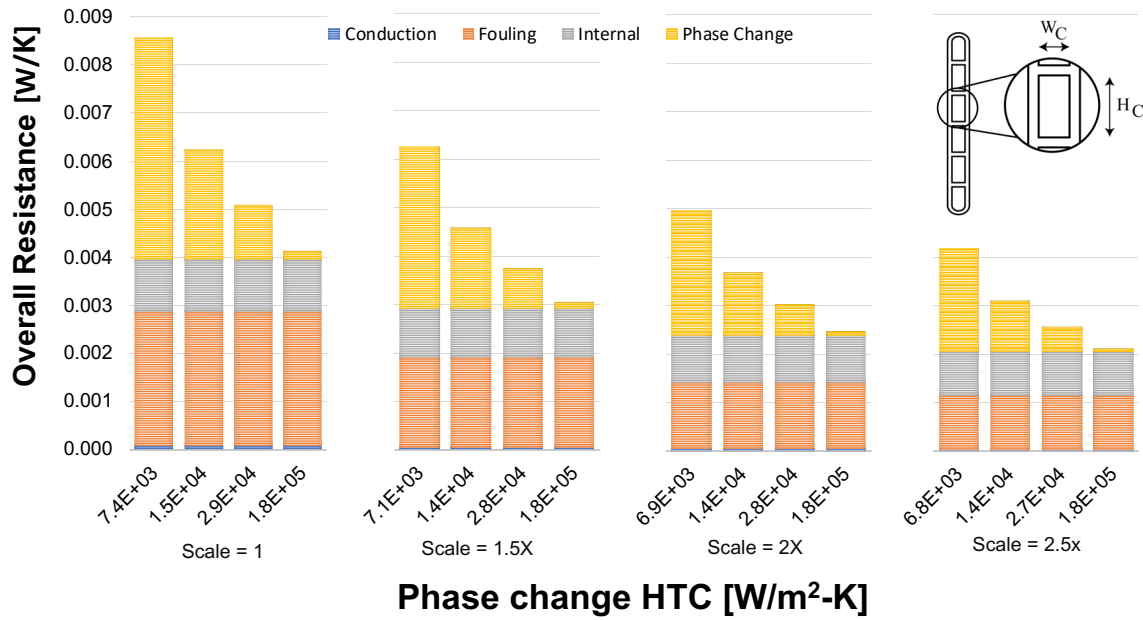


Figure 4-4. The combined effect of phase change and compact condenser scale on overall resistance. Top right inset: compact condenser scale factor,  $Sc = W_c/H_c$

Utilizing fins on condenser tubes, investigators have reported phase change coefficient of heat transfer enhancements of twice or, sometimes up to four times that of the film-wise condensation [27]. For dropwise condensation, Rose et al.'s empirical correlation for dropwise phase change coefficient in presence of steam (equation (2-44)) was used. Hence, four phase change coefficient of heat transfer consisting of film-wise condensation, twice the film-wise condensation, four times the film-wise condensation, and dropwise condensation were chosen.

For any given phase change heat transfer coefficient, we notice the overall resistance drops with increased compact condenser scale factor. This effect is pronounced at first, but it diminishes after a scale of 2x is achieved (Figure 4-4). Furthermore, we noticed that for any given scale factor, somewhere between twice and four times the film-wise

condensation, phase change resistance is no longer larger than the internal resistance. Internal resistance on the other hand, does not significantly increase due to larger channel dimensions. This is due to the fixed condenser area footprint which forces more brine mass flow rate into the larger channels with increased channel scale. Fouling resistance also decreases which can be explained by considering that while the fouling factor,  $R''_f$ , was fixed, according to equation (2-6) fouling resistance reduced with increased fouling area. The film-wise phase change heat transfer coefficient slightly decreased with increased scale due to the increased plate height as a direct consequence of equation (2-28) since phase change heat transfer coefficient is proportional to  $H^{-1/4}$ .

For the same variation in compact condenser scale factor of 2x, and phase change coefficient of heat transfer the condenser parameters were studied. With both increased minichannel scale and phase change heat transfer coefficient, the drop in  $\Pi$  is observed (Figure 4-5).

For a fixed compact condenser scale factor, a decrease in nondimensional pressure drop  $\Pi$  is observed with increased in phase change heat transfer coefficient. This decrease is caused by higher overall heat transfer coefficient which in turn lowers the required heat transfer area, or in this case heat transfer length, translating into lower values for the nondimensional length,  $\Lambda$ .

For a fixed phase change heat transfer coefficient with increasing compact condenser scale factor the hydraulic diameter increases. The increases hydraulic diameter has two effects on the condenser parameters: one is favorable, but the other is adverse. The favorable

effect is the reduced compact condenser pressure drop, and the adverse one is the decrease in internal heat transfer coefficient which leads to longer condenser lengths, and lower overall heat transfer coefficient. For a scale factor beyond of 2x, and phase change coefficient of heat transfer of twice of film-wise condensation the value of  $\Pi$  reaches unity.  $\Lambda$  decreases with increased phase change coefficient of heat transfer, and this is due to the reduction in overall resistance - observed in Figure 4-5 - and hence higher  $\Omega$ . On the other hand,  $\Lambda$  increases with scale and this is despite the overall resistance reduction observed in Figure 4-5. This phenomenon can be explained by revisiting equation (4-7). While the perimeter factor,  $\Gamma$ , slightly increases with increased channel dimensions, the packing density,  $N$ , decreases as bigger and bigger plates are forced to fit in the same available footprint area. Despite  $\Omega$  enhancement, the product  $\Gamma\Omega N$  reduces, and hence  $\Lambda$  increases. It is important to note that, for a 2x scale factor even without any advanced enhancements on the phase change side, the minichannel equivalent length is 0.1 of the conventional bank of tubes with almost matching pressure drops.

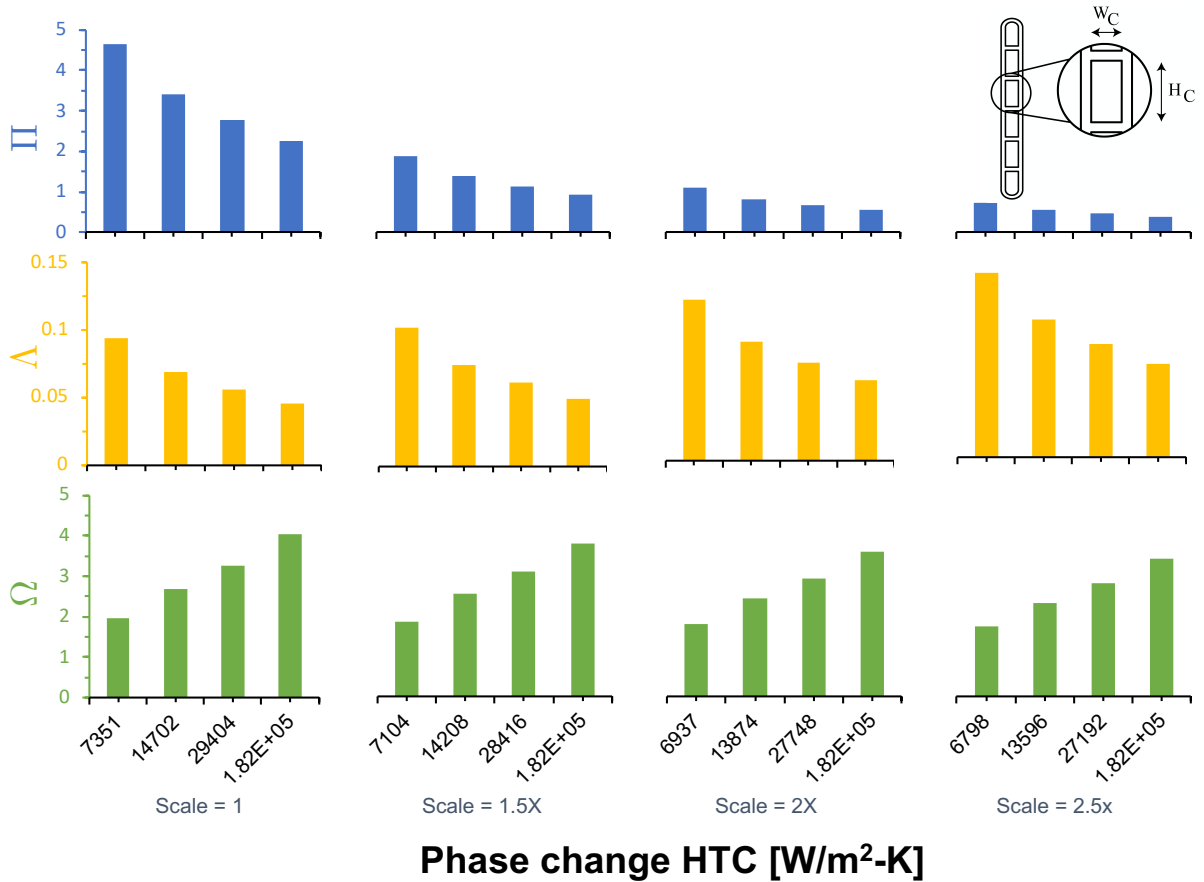


Figure 4-5. The combined effect of phase change enhancement and minichannel scale on the minichannel condenser parameters.

## 4.5. Chapter Conclusions

In this chapter a multistage flash condenser plant was defined with baseline operating conditions. Correlations set forth in the previous chapter were used to estimate the overall heat transfer coefficient and pressure drop across the compact condenser comprised of multiport plate condensers. Heat transfer correlations also were used to validate the conventional bank of tubes condenser. A parametric study comprised of varied plate gap from 1.5 to 20 mm, aspect ratio from 0.5 to 40, wall material thermal conductivity from 0.1 to 10 W/m – K, fouling resistance from 0-10 m<sup>2</sup> – K/kW, phase change heat transfer

coefficient from 7.4 to 180 kW/m<sup>2</sup> – K, and lastly a compact condenser scale factor of up to twice the original one was performed. The following are the salient results of this chapter:

1. Plate gap plays a significant role in the nondimensional
  - a. Overall heat transfer coefficient and hence length
  - b. pressure drop
2. Higher aspect ratio leads to higher overall heat transfer coefficient
3. Higher aspect ratios have negligible effect on nondimensional pressure and length
4. A compact condenser made from material with thermal conductivity of at least 1.6 W/m – K, and in accordance with geometry laid out in Figure 4-2 will most likely perform equally to the baseline model in half the length
5. Internal resistance is not the most dominant resistance in presence of filmwise condensation
6. Enhancements introduced by dropwise condensation decreases overall heat transfer resistance by a factor of two
7. Determination of the actual fouling factor is critical in accurate compact condenser performance predictions.
8. With similar energy inputs and operating conditions, a metallic condenser will perform equally as well as the baseline plant if it is made with internal geometry of
  - a.  $4.5 \times 10.75$  mm in presence of filmwise condensation, or



b.  $3.2 \times 8.6$  mm in presence of dropwise condensation

at lengths of 15%, and 9% of the original length respectively



## Chapter 5: Experimental Validation



## 5.1. Introduction

The total plant size reduction predictions made in chapter 5 are significant. As the great late Carl Sagan said once, extra ordinary claims require extra ordinary evidence, the following chapters provide such evidence.

In this chapter, the results of experiments on condensation using the multiport minichannel plate condensers are reported. Experiments were performed on a single plate of the condenser as well as on 5-plate, 2-row array configurations with two different plate spacings. Furthermore, condensation experiments with a hydrophobic coating are also performed. The results of the compact condenser are compared against a baseline tubular condenser. The experimental facility, the experimental and data analysis procedures, and uncertainty quantification is described. The experimental results are compared against the model developed in the prior chapter.

## 5.2. Experiment

### *5.2.1. Experimental Apparatus, and Facility*

To evaluate the thermal performance of the proposed compact condenser, and hence validate the predictive model, an apparatus (Figure 5-2.c) was fabricated in which three test article were tested (Figure 5-2.a and b.) only two of three articles showing). The apparatus consisted of two sections: a lower chamber where vapor was generated, and an upper chamber in which a test articles was located. The vapor generator section of the apparatus (item 10 in Figure 5-2.c) was flanged to the top portion sealed with a circular

O-ring compressed by bolts. The upper chamber was outfitted with three sight glasses for observation of the condensation process. Pressure release valves were set in place enabling rapid and safe chamber pressurization in case of an emergency. Vapor was generated in the lower chamber using a 4-kW nominal serpentine heater powered using an AC variac (Volteq 5KVA) (item 10 in Figure 5-2.c) actuated with a PID controller. A vacuum port, connected to a two-stage vacuum pump (Welch duo-seal 1400) connected to a 30-gallon (Speedaire) container were used to test condensation under sub-atmospheric conditions. On one side of the top section, bore-through plastic NPT fittings were utilized to provide sealed chamber connections to outside (items 8 and 9 in Figure 5-2.c). These fittings connect the internal flow loop to the compact condenser to be tested located within the chamber. The experimental test loop for the internal flow is shown in Figure 5-1. Cooling water was stored in an external reservoir and pumped through the condenser. The heat gain within the condenser was removed in the reservoir using submerged copper cooling coils connected to either a 4-kW recirculating chiller (Figure 5-1), or by room-temperature process water. Chamber pressure was measured through a capacitance-type pressure transducer (Validyne DP15) equipped with a max 120kPa sensing diaphragm (Validyne dash#42). To measure the cooling water flow rate, an positive displacement flow meter (Omega FPD3204-D-A) was used. Vapor temperature was measured in 3 locations throughout the chamber. Cooling water temperature in and out of the condenser, pool, and vapor temperature were measured via T-type (Omega TJ36-CAIN-18U-6) thermocouples. The thermocouples were connected to a data acquisition board (National Instrument NI-9211) data acquisition board (DAQ), and the flow meter, and pressure

transducer signals were connected to another DAQ (National Instruments NI-6009). Both DAQs were connected to a computer, and the received data was logged for later calculation, and plotted for real time monitoring for steady state condition.

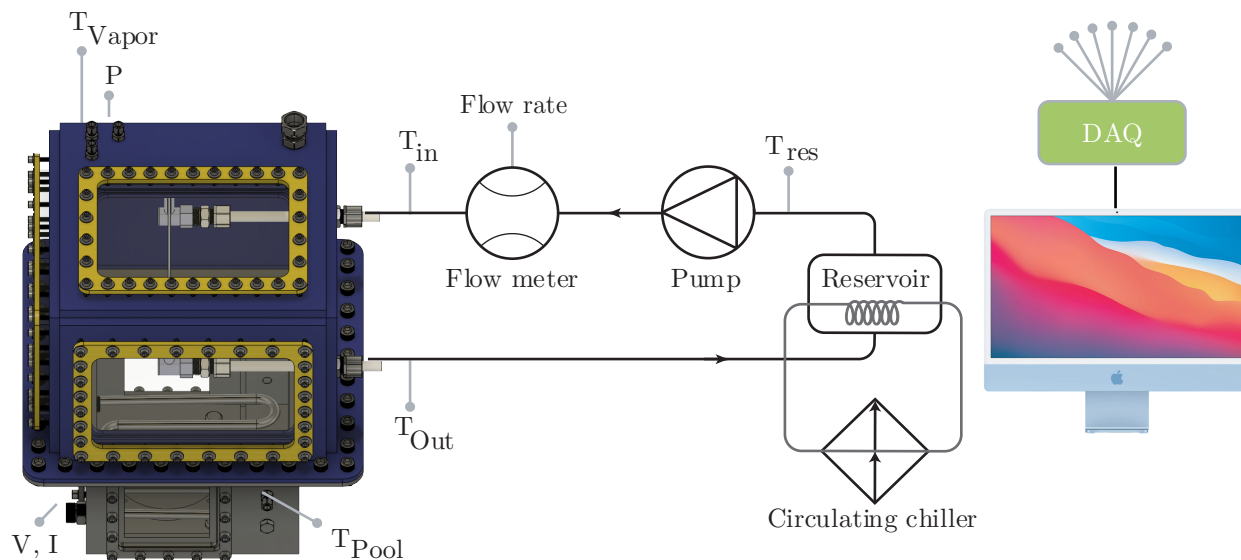


Figure 5-1. Experiment loop

### 5.2.2. Multiport Condenser Test Articles

One of the condensers comprised of a single mini-channel plate, and the other two of 5 similar single plates. The 5-plate condensers were identical to each other except for their horizontal plate spacing. One of the configurations had a 6 mm, and the other a 4 mm nominal plate-to-plate spacing,  $\Delta$ . The as-built individual condenser plate-to-plate spacings are  $\Delta_1 = 5.83$  mm,  $\Delta_2 = 6.07$  mm,  $\Delta_3 = 6.64$  mm for the 6 mm, and  $\Delta_1 = 3.78$  mm,  $\Delta_2 = 2.94$  mm,  $\Delta_3 = 2.96$  mm for the 4 mm configuration with  $\Delta_{1,2,3}$  defined in Figure 5-2.e. Each of the 30 mm by 3 mm slot-shaped aluminum mini-channel plate

architecture was comprised of 6 4.3 mm by 1.8 mm rectangular internal passages separated by 600  $\mu\text{m}$  walls (Figure 5-2.d).

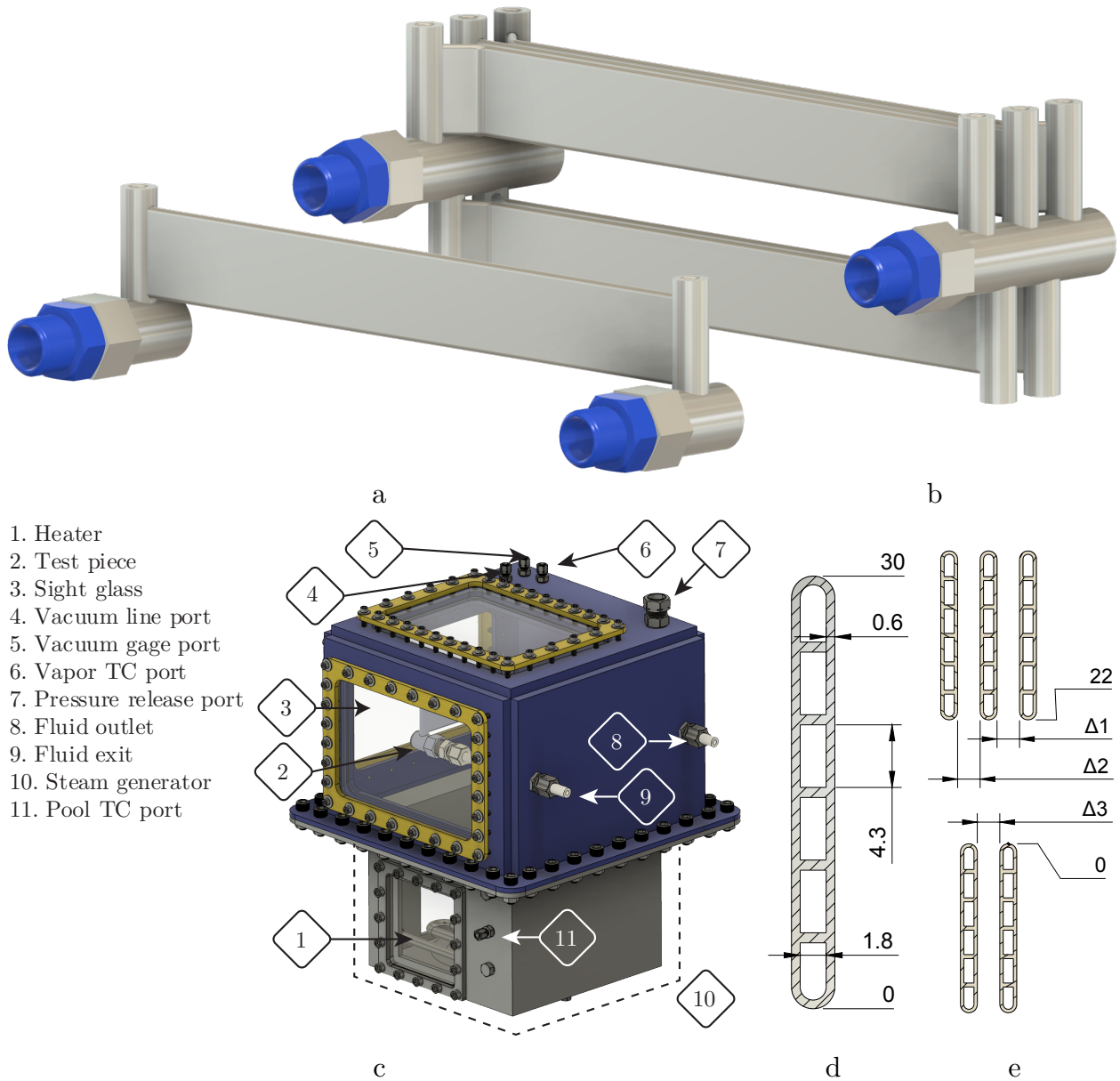


Figure 5-2. Experimental loop A 3D view of two of the testes articles, a) single plate and b) 5-plate condenser. c) Experiment apparatus. d) condenser plate internal dimensions. e) 5-plate plate configuration. All dimensions are in mm.

### 5.2.3. *Hydrophobic Coating*

It is possible to achieve higher contact angles if the effect of dropwise promoter and surface roughness is combined [35]. To determine the surface roughness which provides the highest contact angle, 4 plates were sanded with grits progressively leading up to 120, 320, 600, 1000, and 2000 with intermediate condenser plate cleaning via isopropanol alcohol. when the final grit sanding paper was used the plates were cleaned and coated with a superhydrophobic coating (NEI NANOMYTE® SuperCN Plus) using a high-volume low-pressure nozzle spray. The samples were then cooked for 30 mins at 160 °C inside a temperature-controlled oven. Sample substrates were tested for contact angle via 15  $\mu$ L sessile droplet tests performed on a Theta Optical Tensiometer (Attension, Biolin Scientific, Stockholm, Sweden). The contact angle measurement was performed at least 4 times for each substrate (Figure 5-3). For each measurement the native software detected and averaged the advancing contact angle over 10 seconds of data collected with a frequency of 2 Hz (total of 20 samples). The four advancing contact angles were average for each substrate and compared to the other substrates and an uncoated and unsanded baseline substrate, results of which are presented in table 5-1.

Table 5-1: 4-point average contact angle measurement for different surface roughness

<b>Grit</b>	<b>120</b>	<b>320</b>	<b>600</b>	<b>1000</b>	<b>2000</b>	<b>Baseline</b>
4-point average contact angle	122	111.3	114.7	115	113.4	76.5

As evident by the results in table 5-1, grit number 120 was found to yield the highest advancing contact angle. Hence the single plate, and the 4 mm 5-plate condensers were

sanded with 120 grit sandpapers and coated with an NEI NANOMYTE® SuperCN Plus dropwise-condensation promoter similarly to the procedure described in this subsection.

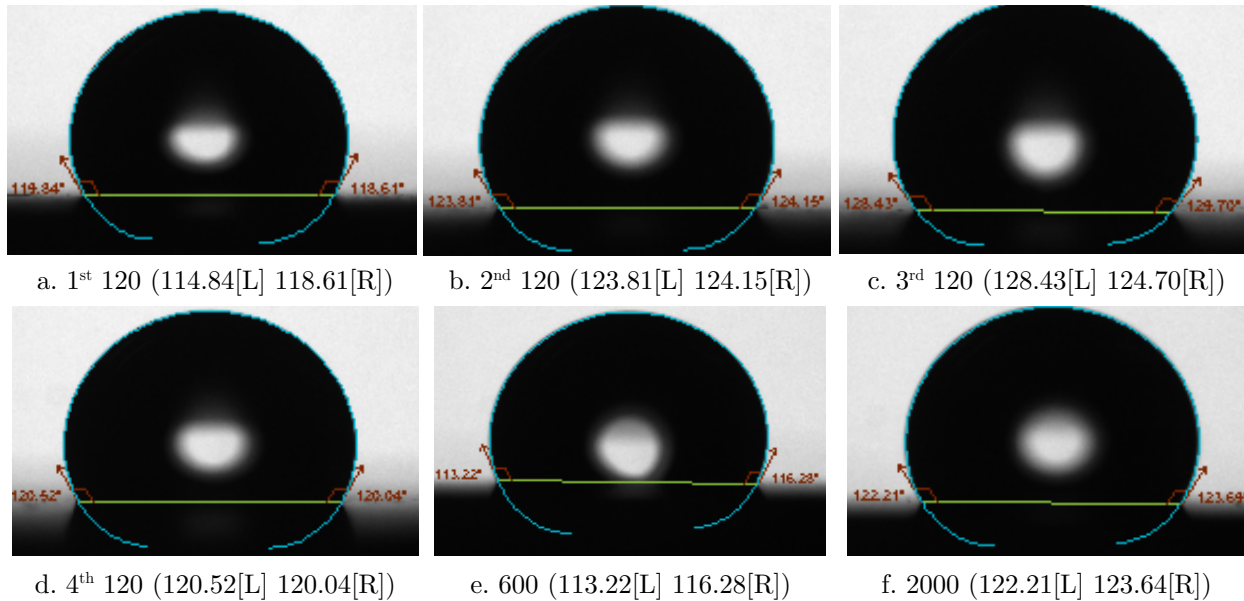


Figure 5-3. a-d repeated recorded advancing contact angle on the 120 surfaces. Recorded advancing contact angle on the e. 600, and f. 2000 surface

#### 5.2.4. *Experimental Procedure and Data Analysis*

Prior to the start of an experiment, the lower chamber of the apparatus was filled with deionized water to a marked location. Using the serpentine heater, the deionized water was boiled vigorously for at least an hour leading to the release of dissolved gasses. To initiate the degassing process, the heater, the circulating pump, and the chiller were turned on and the vacuum line was opened. A portion of the steam condensed on the test article and the remaining steam in addition to the non-condensable gases were continuously vented through the vacuum port. The degassed pool of water was later used to generate steam, imitating the multistage flash process.



After the degassing period, the desired subcooling was prescribed in the LabView program, and target flow rate was adjusted to the target value using a combination of the pump variable speed control, and a ball valve installed in-line downstream of the pump.

In this work subcooling (or supersaturation) is defined as the difference between the temperatures of chamber vapor and the average of the inlet and outlet, i.e.

$$\Delta T_{\text{sub}} = T_v - (T_{\text{out}} + T_{\text{in}})/2. \quad (5-1)$$

In accordance with equation (5-1), the serpentine heater was actuated to maintain a prescribed system subcooling.

The condensation heat transfer rate was obtained using the gain in internal energy of the fluid,

$$Q = \dot{m}c_p(T_{\text{out}} - T_{\text{in}}), \quad (5-2)$$

in which  $c_p$  is the specific constant-pressure thermal capacitance of water evaluated at the  $T_i$ .

Heat flux of condensation is calculated as

$$q = Q/n_p A_{\text{phx}}. \quad (5-3)$$

The overall heat transfer coefficient is determined based on equation

$$U = Q\Delta T_{\text{lm}}/A_{\text{phx}}, \quad (5-4)$$

where  $\Delta T_{\text{lm}}$  is the log mean temperature difference and defined as

$$\Delta T_{\text{lm}} = (T_{\text{out}} - T_{\text{in}})/\ln\left(\frac{T_v - T_{\text{in}}}{T_v - T_{\text{out}}}\right). \quad (5-5)$$

For each condition, the condensation heat transfer rate was calculated using equation (5-2), and monitored in real time for steady state conditions. When such conditions are met, experiment variables are recorded for at least 3 minutes and logged for later analysis. Throughout the experiment, chamber was subjected to vacuum via the suction line. Such measures are akin to those employed in multistage flash plants to battle the adverse effect of non-condensable gas accumulation [11] [26].

The experiment was concluded by stopping the circulating pump, vacuum pump, the heater, and the chiller. Outside air was introduced into chamber to prevent chamber from reaching low pressures induced by the condensation of the remaining chamber steam overnight.

#### 5.2.4.1 Routine Chamber Leak Check

Prior to the start of each experiment, chamber pressure was reduced to 20kPa, and its rate of increase was measured for 10 minutes. In addition to this, chamber pressure was monitored overnight. A pressure recovery rate of 80-100 mPa/s was observed. The pressure increase was converted to a leak mass flow rate by ignoring time variations in chamber volume,  $V$ , and temperature,  $T$ , i.e.  $\frac{\partial V}{\partial t} = \frac{\partial T}{\partial t} = 0$ , through the ideal gas law assumption:

$$V \frac{\partial P}{\partial t} + P \frac{\partial V}{\partial t} = R \left( m \frac{\partial T}{\partial t} + T \frac{\partial m}{\partial t} \right), \quad (5-6)$$

and hence,

$$\frac{\Delta m}{dt} = \frac{V}{RT} \frac{dP}{dt}, \quad (5-7)$$

which when integrated yields

$$\Delta m = \frac{V}{RT} \Delta P. \quad (5-8)$$

in which  $R$  is the specific gas constant for air. The 80-100 mPa/s pressure increase rate corresponded to 2-2.5 mg/s using equation (5-8).

## 5.2.5. Statistical Analysis

### 5.2.5.1 Experiment Uncertainty Analysis

Table 5-2 lists the uncertainty errors in the instruments used for temperature, pressure, and mass flow rate measurement.

Table 5-2: Measured value, their range, and uncertainty

Variable	Range	Uncertainty, $\delta$	Unit
Pressure	10-120	$\pm 1$	kPa
Flow rate	8-500	0.03%	g/s
Inlet temp	273-670	0.07	K
Outlet temp	273-670	0.09	K
Vapor temp	273-670	0.1	K

The uncertainty in temperature measurements is calculated to be 0.07, 0.09, and 0.1 °C for inlet, exit, and vapor temperatures respectively, and flow rate uncertainty is taken to be 0.3% of the flow rate, as per manufacturers documentation. This uncertainty, associated with each measured quantity, is the sum square of its constituent errors. For example, the uncertainty in temperature measurement is due to the following sources: calibration curve, calibrating standard, and steady state i.e.:

$$\delta T^2 = \sigma_{calibration}^2 + \sigma_{curve}^2 + \sigma_{s.s.}^2. \quad (5-9)$$

Uncertainty analysis for the calculated quantities, on the other hand, was performed through Engineering Equation Solver's (EES, F-Chart Inc) error propagation algorithm using the Kline and McClinton propagation of errors method [60].

As an example, EES determines uncertainty propagation for the condensation heat transfer rate formulated in equation (5-5), as

$$\delta Q^2 = \left( \frac{\partial Q}{\partial \dot{m}} \delta \dot{m} \right)^2 + \left( \frac{\partial Q}{\partial T_i} \delta T_i \right)^2 + \left( \frac{\partial Q}{\partial T_o} \delta T_o \right)^2. \quad (5-10)$$

in equation (5-10), it is assumed that the error due to constant pressure specific heat is negligible,  $\delta c_p = 0$ , and  $\delta$  accompanied by any quantity indicates the error in that quantity, see Table 5-2.

Carrying out the partial differentiation, equation (5-10) becomes

$$\delta Q^2 = [c_p(T_o - T_i)\delta \dot{m}]^2 + (\dot{m}c_p\delta T_i)^2 + (\dot{m}c_p\delta T_o)^2. \quad (5-11)$$

Equation (5-11) is the final form using which EES determines the calculated uncertainty.

### 5.2.5.2 Mean Absolute Error

In order to quantify the efficacy of the model, Mean Absolute Error (MAE) as defined below was used:

$$MAE = \sum_{i=1}^n |X_i - Y_i| / n, \quad (5-12)$$

in which  $X_i$  is the measured quantity,  $Y_i$  is the predicted value of the quantity of interest, and  $n$  is number of samples used to calculate the metric. An alternative form of equation (5-12) defined as

$$MAE_P = 2 \frac{\sum_{i=1}^n |X_i - Y_i|}{\sum_{i=1}^n (X_i + Y_i)} \times 100, \quad (5-13)$$

was used in this work.

### 5.2.6. Results and Discussion

The results of three test articles, two 5-plate staggered and a single plate, in addition to the coated single plate, and the coated-tightly packed condenser are presented in this section. The matrix of performed experiments and their corresponding measured quantities is shown in table 5-3.

Table 5-3: Experiment matrix, range, and results

Variable	$\dot{m}$	Re ( $10^3$ )	$\Delta T_{sub}$	$P_{ch}$	$T_{ch}$	$q$	$U_{phx}$
Units	g/s		K	kPa	$^{\circ}\text{C}$	$\text{kW}/\text{m}^2$	$\text{kW}/\text{m}^2 - \text{K}$
Uncoated single multiport condenser							
Range	13.2-132	1.51-14.7	4, 8, 12	12.3 -30.3	50.2-69.7	10.0-90.1	2.75-8.16
Uncoated 5-plate staggered condenser							
Range	20.1-55.2	2.31-6.72	4, 8	23.0-41.1	63.3-68.2	14.2-37.0	2.50-6.23
Coated single multiport condenser							
Range	24.3 - 264.1	3.01-36.1	4, 8	37.4-55.5	74.6-84.2	20.1-137	5.17-17.1
Coated 5-plate staggered condenser							
Range	13.8-52.2	1.81-6.23	4, 8	37.4-55.5	22.0-39.4	10.1-31.2	2.90-6.14

#### 5.2.6.1 Figure Interpretation

For brevity, a nomenclature with the following discription is adopted in this work. The nomenclature assigned to the 6 mm 5-plate configuration is  $\Delta 6$ , and for the 4 mm 5-plate configuration is  $\Delta 4$ , and the single multiport plate is denoted by P1. Furthermore, when

followed by the letter ‘H’ the nomenclature indicates that the configuration is coated with the hydrophobic promoter.

In Figures 5-4 - 5-9 , and Figures 5-16 - 5-18 mustard, green, and blue-shaped figures represent 4, 8, and 12 K subcooling respectively. Hollow square, upward, and downward triangle shapes represent P1,  $\Delta_6$ , and  $\Delta_4$  respectively. Model values are indicated by filled circles connected with dashed lines matching in color with their corresponding subcooling. Filled shapes with error bars indicate the results of hydrophobic coating. While Figures 5-4 - 5-9, and Figures 5-11 - 5-14 compare the model calculation, as described by the set of equations (2-1)-(2-5), to experiment results performed on a single test articles, Figure 5-16 - 5-18 are comparisons between different configuration. Figures 5-4 - 5-9 are the results of experiments with no dropwise promoter, and Figures 5-11 - 5-14 are the results of experiments with the dropwise promoter.

The abscissa either represents hydraulic-diameter based Reynolds,  $Re_D$ , number as defined in equation (2-21), or individual plate flow rate. Similarly, the ordinate either indicate the individual plate flux of condensation as defined in equation (5-3), or the overall heat transfer coefficient as defined in equation (5-4) is observed.

### 5.2.6.2 Single Multiport Plate

For P1 configuration, while Figure 5-4 depicts the effect of varied flow rate on condensation flux for different subcooling values, Figure 5-5 is a plot of hydraulic-diameter based Reynold number, as defined by equation (2-21), against overall heat transfer coefficient for the same subcoolings. The following observations are true for both the experimental and model calculation values.

For any given subcooling, as the flow rate increases so does the condensation flux, and the overall heat transfer coefficient. This effect diminishes as flow rate increases, suggesting a transition from internal flow resistance dominance to a phase change resistance one.

On the other hand, as subcooling increases so does the driving force,  $T_{sat} - T_s$ , in equation (2-28). This increase in driving force leads to a reduced phase change coefficient of heat transfer, and, for a fixed flow rate, lower overall heat transfer coefficient (Figure 5-5). In other words, for a fixed flow rate higher overall heat transfer coefficient is observed for lower subcooling values. For example, the overall heat transfer coefficient for P1 12K at  $Re_D = 12.5 \times 10^3$  is  $6.9 \text{ kW/m}^2$ , but it is  $8 \text{ kW/m}^2$  for P1 4K at the same  $Re_D$  (15% higher).

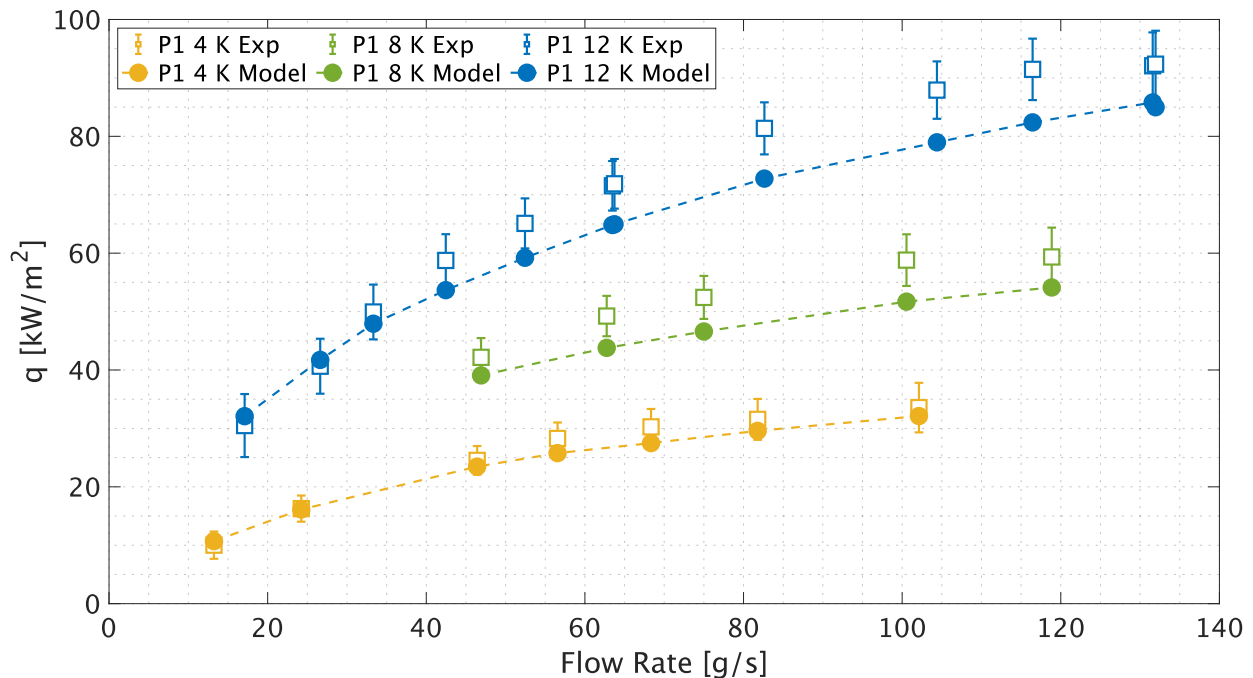


Figure 5-4. Condensation flux vs different flow rate for different subcooling for the single plate test article.

In the case of condensation flux, the competing effect of reduced overall heat transfer coefficient and increased driving force causes the transition from internal-resistance to phase-change-resistance dominance to occur at lower flow rates for lower subcoolings (Figure 5-4). The mean absolute error (MAE) of 2.34, 4.5, and 5.71 kW/m<sup>2</sup> for the flux of condensation was calculated for the 4, 8, and 12 K subcooling respectively.

For a fixed flow rate, on the other hand, while the condensation flux increases with increased subcooling, the overall heat transfer coefficient remains unaffected. The minor observed variations in overall heat transfer coefficient are due to different chamber pressure, and saturation conditions, which, among other factors, effect the latent heat of evaporations the most which in turn effect the phase-change coefficient of heat transfer (Figure 5-5). Reynolds numbers corresponding to 6200 and 14500 for 12 K subcooling are repeatability experiments performed after a routine flow rate sweep has been done. The overlapping results for these repeat experiment attest to high experimental repeatability.



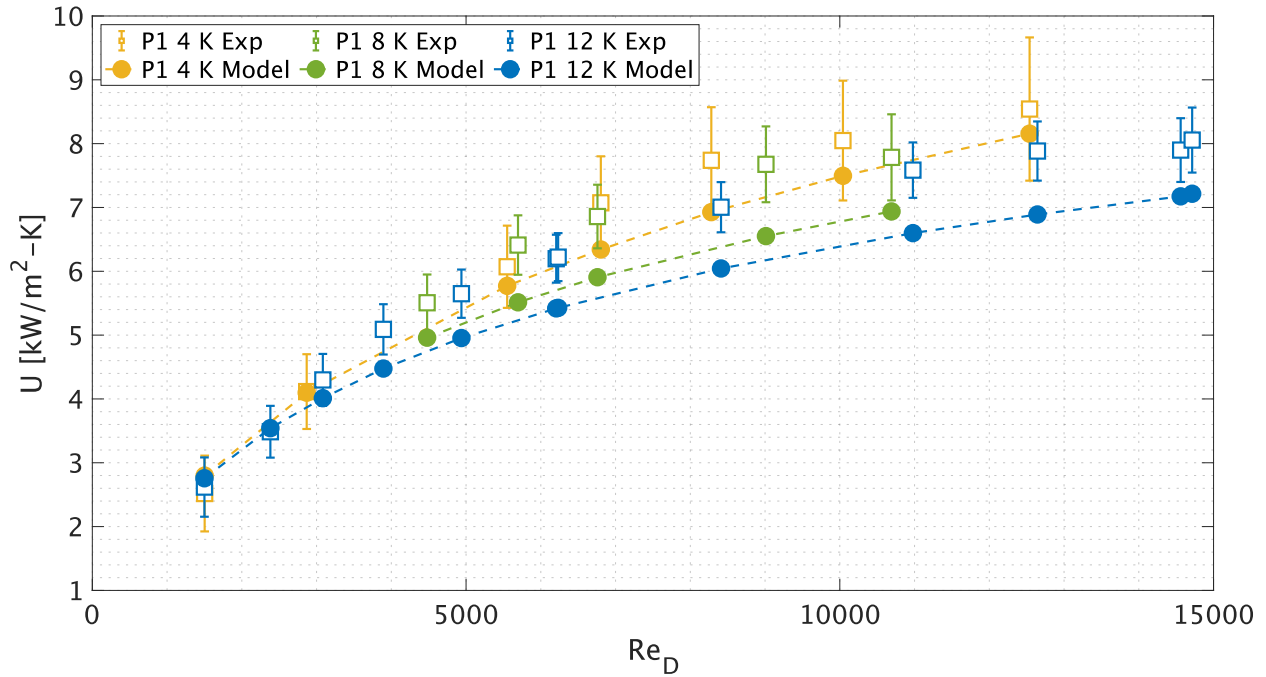


Figure 5-5. Overall heat transfer coefficient vs hydraulic-diameter based Reynolds number for different subcoolings for the single plate test article. Condensation length, and area for the single plate configuration was found to be  $234.9 \pm 0.01$  mm, and  $148.6 \pm 0.024$  cm<sup>2</sup> respectively. Chamber pressure varied between 25.6-28.5, 12.3-14.9, and 18.5-30.3 kPa for 4, 8, 12 K subcooling respectively during the experiment.

For low flow rates conditions of 12 and 8K subcooling ( $Re_D < 4000$ , 12K –  $Re_D < 6000$  8K) and for all the tested flow rates of the 4K subcooling, the experimental values are in good agreement with the model values. For high subcooling and mid flow rate ( $Re_D < 14500$ , 12K –  $Re_D < 12500$  8K) conditions the condenser outperforms the model predictions by at most 20%. An MAE of 0.68, 0.74, and 0.66 kW/m<sup>2</sup> – K for the overall heat transfer coefficient was calculated for the 4, 8, and 12 K subcooling respectively.

### 5.2.6.3 5-Plate Multiport Plate

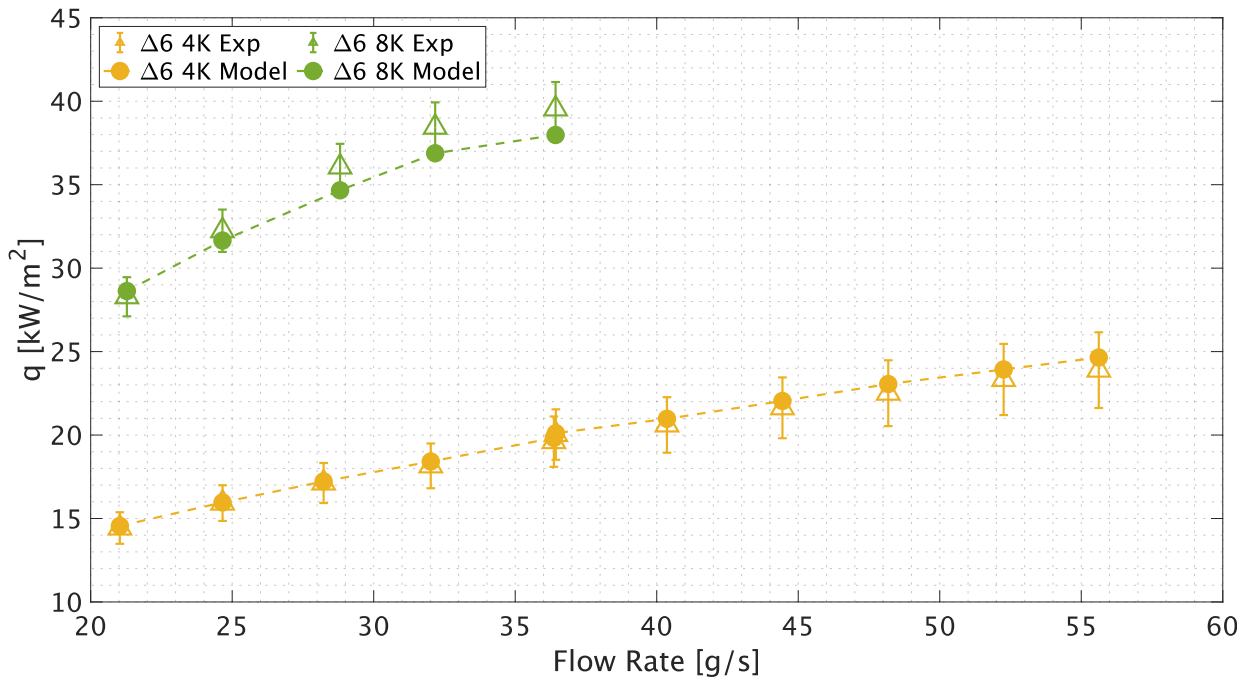


Figure 5-6. Per plate heat flux of condensation vs per plate flow rate for the 6 mm 5-plate test article.

Figures 11 - 14 represent the model vs experiment comparison for the 5-plate configuration test articles. While Figures 11, and 12 corresponding to the 6 mm vapor spacing,  $\Delta 6$ , Figures 13 and 14 correspond to the 4 mm plate spacing,  $\Delta 4$ .

Figure 5-6 is a plot of flux of condensation against individual plate flow rate. In this figure, as flow rate increases, for either of the subcoolings, condensation flux improves, albeit a linear increase for the 4 K subcooling, and a decaying one for the 8 K subcooling is observed. An MAE of 0.30, and 1.1 kW/m<sup>2</sup> for the flux of condensation was calculated for the 4, and 8 K subcooling respectively.

Figure 5-7 depicts the effect of hydraulic-radius based Reynold,  $Re_D$ , number on overall heat transfer coefficient. Either of the subcooling trends are steeply increasing with  $Re_D$ ,

suggesting highly internal-resistance-controlled heat transfer. The overall heat transfer coefficient decreases with increased subcooling for the same argument presented for the single plate test article.

There is a good agreement between the model prediction and the experiment values for both flux of condensation, and overall heat transfer coefficient for the case of 4 K subcooling. An MAE of 0.12, and 0.40 kW/m<sup>2</sup> – K for the overall heat transfer coefficient was calculated for the 4, and 8K subcooling respectively.

On the other hand, for the 8 K subcooling case while condensation flux model prediction lies within the experiment uncertainty, overall heat transfer

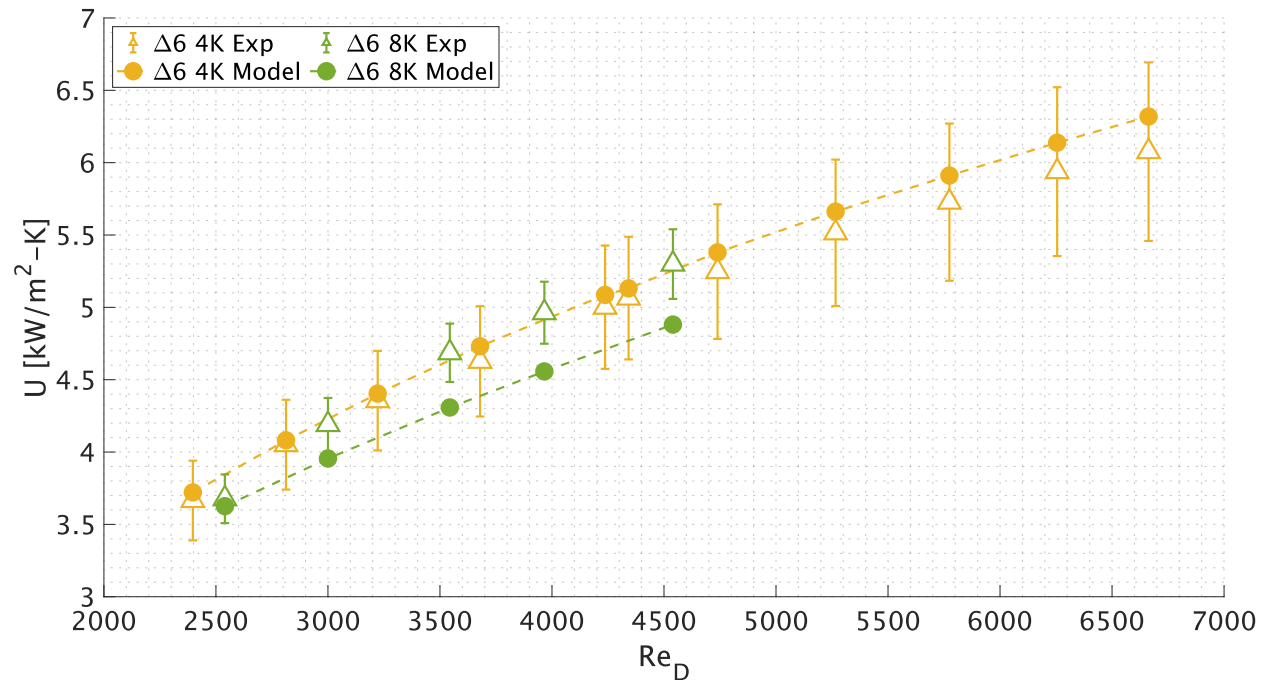


Figure 5-7. Overall heat transfer conductance vs hydraulic-diameter based Reynolds number for the 5-plate 6 mm plate spacing test article. For this article the plate-averaged length of condensation was measured to be 225.0±0.01 mm, and the entire condensation area to be 711.5±0.117 cm<sup>2</sup>. Chamber pressure varied between 23.02-26.14, and 32.89-37.20 kPa for 4, 8 K subcooling respectively during the experiment.

coefficient deviates, beyond the bounds of uncertainty, from model predictions as flow

rate exceeds  $Re_D > 3000$ . Albeit within experimental uncertainty, overall heat transfer coefficient increases with increasing subcooling, a phenomenon opposite to that predicted by the model. The 8 K subcooling case was performed at higher pressures than 4 K subcooling which is thought to be the reason for the observed higher overall heat transfer coefficient. Higher pressure increases latent heat of evaporation, lowering film thickness.

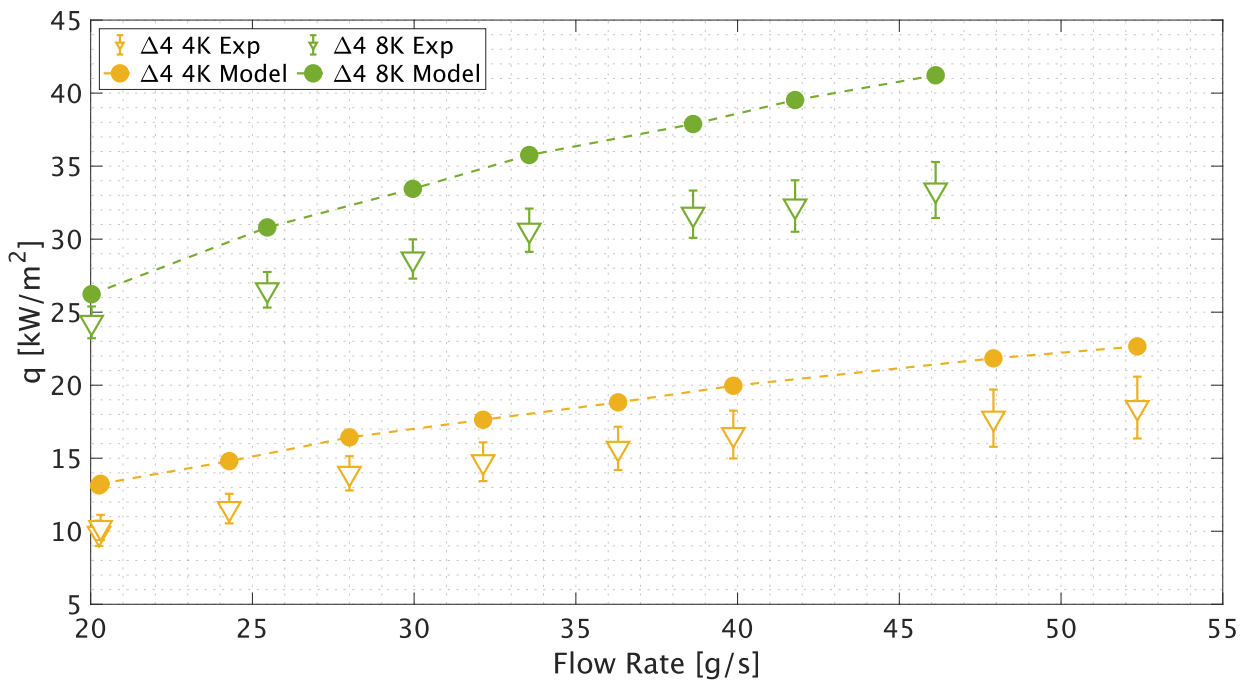


Figure 5-8. Per plate heat flux of condensation vs per plate flow rate for the 4 mm 5-plate test article.

Figure 5-8 depicts the effect of per plate flow rate to the condensation flux for the  $\Delta 4$  configuration. There is an increase in measured heat of condensation with increased flow rate for the 4 K subcooling case, but the 8 K subcooling reaches a plateau at around 35 g/s.

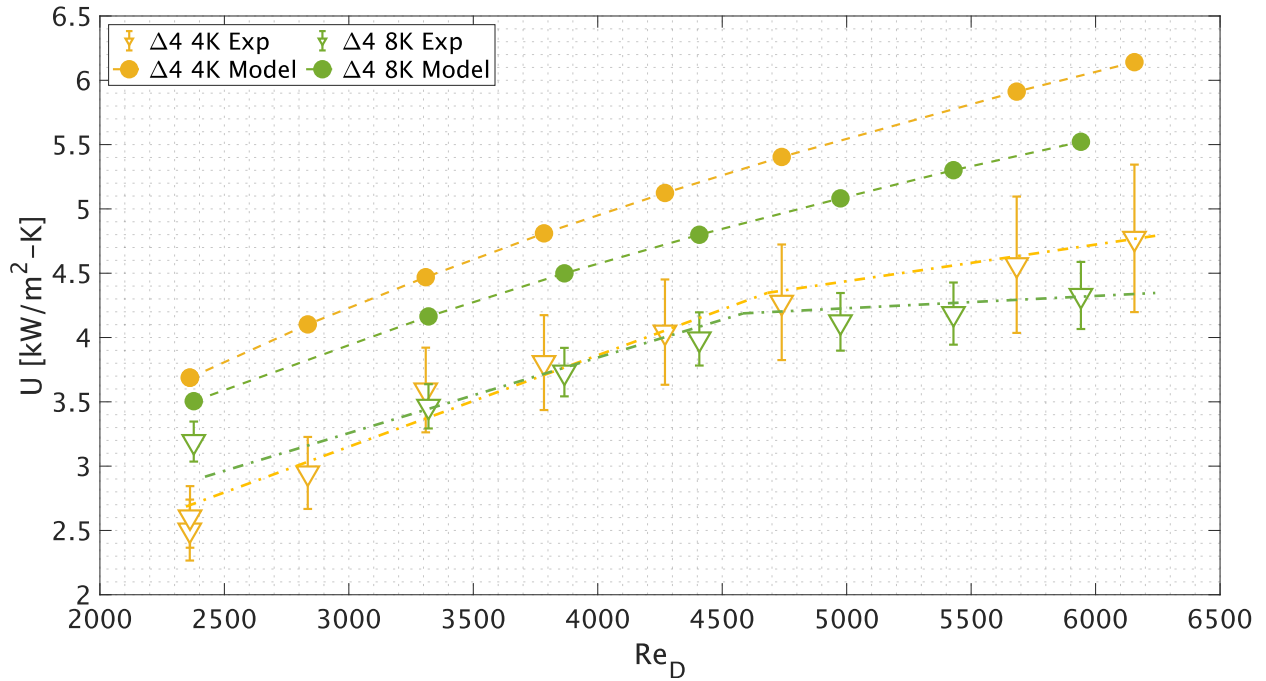


Figure 5-9. Overall heat transfer conductance vs hydraulic-diameter based Reynolds number for the 5-plate 4 mm plate-to-plate spacing test article. For this article the plate-averaged length of condensation was measured to be 230.1 mm, and the entire condensation area to be  $727.6 \pm 0.119 \text{ cm}^2$ . Chamber pressure varied between 31.04-41.07, and 23.26-23.66 kPa for 4, 8 K subcooling respectively during the experiment. The dotdashed lines represent arbitrary fit curves used for demonstration purposes.

For either of the subcoolings, an increase in overall heat transfer coefficient with increased  $Re_D$  for the  $\Delta 4$  test article is observed. The similarities between model prediction and the experiment results end here. The rate of increase of the measured values reduces with increased  $Re_D$ , while the model predicts a steady increase with  $Re_D$ . This gradual reduction in the rate of reduction suggests a phase-change-resistant dominant flow. This premature switching to phase change resistance dominance is believed to be the reason for the observed deviation of the measured and calculated values. An MAE of 3.30, and 5.3  $\text{kW/m}^2$  for the flux of condensation were calculated for the 4, and 8 K subcooling respectively. Due to this observed deviation from the model, another experiment

performed at both subcoolings was conducted on a different day, results of which were identical to the one presented here.

Visual observation of the condenser plates in operation revealed that the 4 mm plate-to-plate spacing configuration gives rise to dry patches formed on the internal condenser plate, and surfaces with stagnant droplets (Figure 5-10.b). In contrast, the outer most surfaces, those with direct line of sight to the chamber wall, form a film throughout the entire condensation surface (Figure 5-10.a). To contrast film versus dry patch formation, a frame with a minor dry patch created on the outer condenser plate was chosen. As seen in the dashed rectangle of Figure 5-10.a, this dry patch leads to curvature-caused white

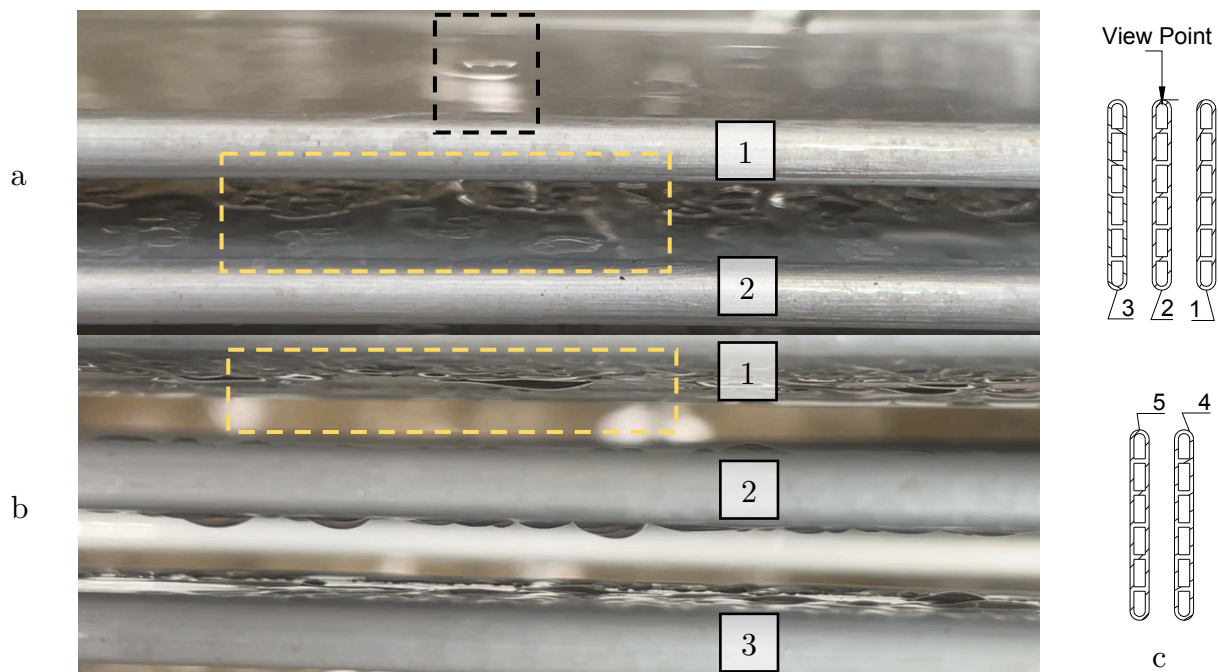


Figure 5-10. Top view of the 4mm plate-to-plate spacing article for 36 g/s 4 K subcooling condition. a. Film formation on the outer plate (top plate in the current picture) compared to dry patches observed on the inner plate (yellow dashed box). b. A more detailed picture of inner plates with apparent more dry patches in between the plates. c. point of view

reflection and hence indicates the presence of film condensation. Examples of dry patches can be seen throughout the boxed dashed rectangle in Figure 5-10.a.

## Hydrophobic Coating

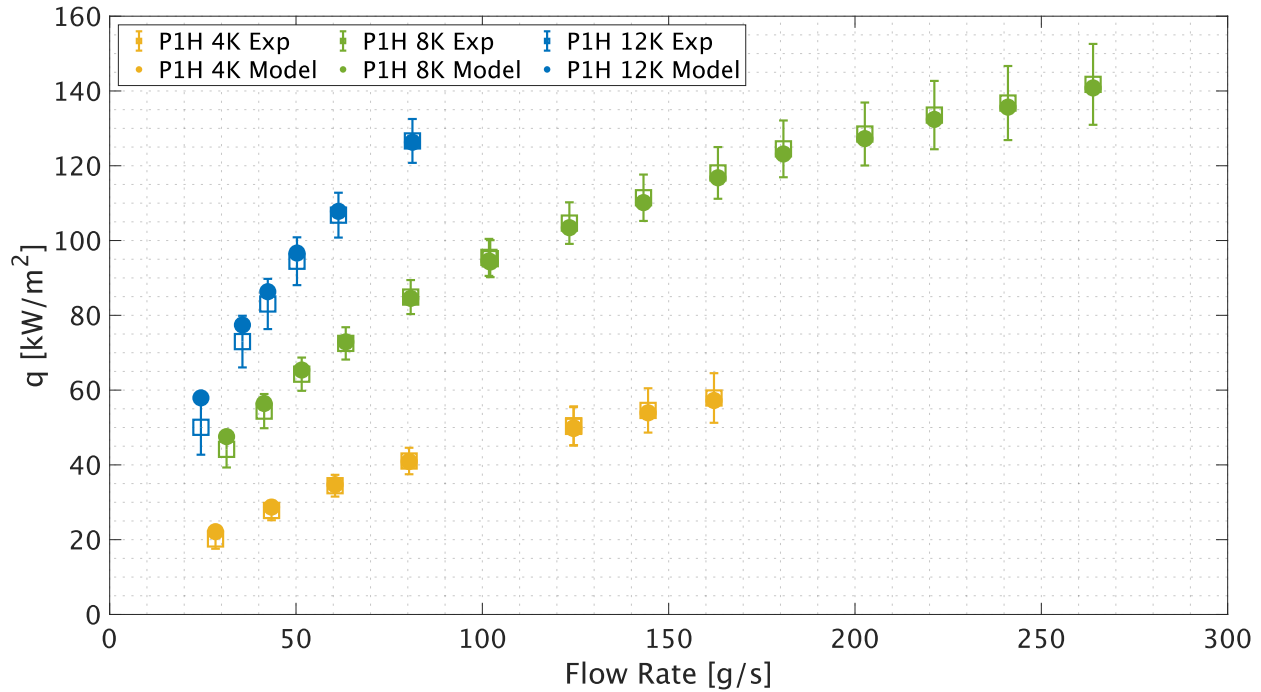


Figure 5-11. Condensation flux vs different flow rate for different subcoolings for the single plate test article with hydrophobic promoter.

The single plate condenser was coated with a hydrophobic promoter and was tested at different subcoolings with varied inlet flow rates, the results of which are presented in Figures 5-11, and 5-12. Heat flux of condensation, and overall heat transfer conduction was modeled by replacing filmwise condensation resistance (2-28) with dropwise condensation resistance (2-44), and the addition of promoter resistance equation (2-9). Promoter thickness assumption of  $5.5 \mu\text{m}$  lead the lowest  $R^2$  value between model and measured heat of condensation, and overall heat transfer coefficient.

For any subcooling, condensation flux increases when flow rate increases with larger observed slopes for higher subcoolings (Figure 5-11). The 4, and 8 K subcooling receive a diminishing effect from increased flow rate, yet the following trend is not observed for the

12 K condition. As mentioned earlier, due to the limitation on the steam generator heater higher flow rates could not be tested for the 12 K subcooling condition. For 4 K subcooling, the highest flux of condensation is achieved when the second lowest flux of condensation at 8 K is achieved. Similarly, the condensation flux achieved for 200 g/s at 8 K subcooling is equal the measured flux of condensation at for only 80 g/s at 12 K subcooling.

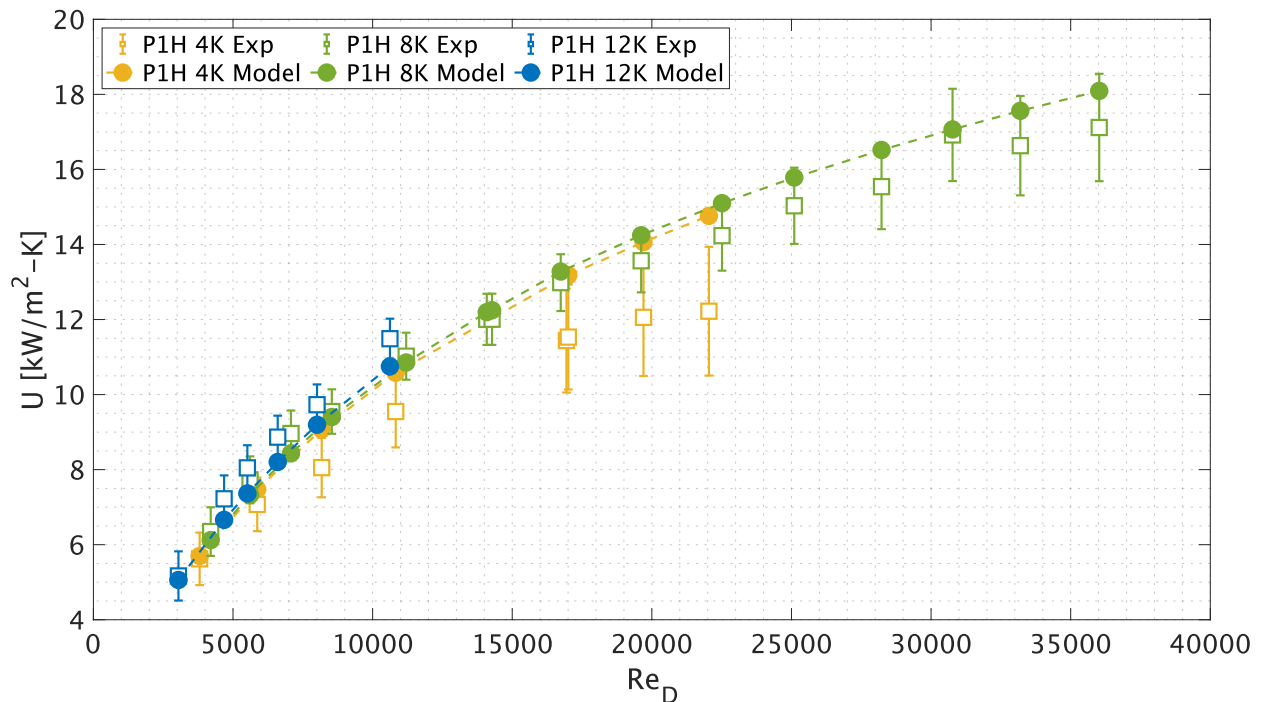


Figure 5-12. Overall heat transfer coefficient vs hydraulic-diameter based Reynolds number for different subcoolings for the single plate test article coated with the dropwise promoter. Condensation length and area for the coated single plate configuration was found to be  $235.1 \pm 0.01$  mm, and  $148.7 \pm 0.024$  cm<sup>2</sup> respectively. Chamber pressure varied between 37.5-38.9, 64.5-49.7, and 51.1-55.5 kPa for 4, 8, and 12 K subcooling respectively during the experiment. A  $5.5 \mu\text{m}$  promoter thickness and a thermal conduction of  $0.25 \text{ W/m-K}$  was assumed for the calculated values.

Except for low flow rate values at 12 K, the model prediction is in excellent agreement with the measured values. An MAE of 0.4, 0.78, and 1.98, kW/m<sup>2</sup> for the flux of condensation was calculated for the 4, 8 and 12 K subcooling respectively.

As Reynolds number increases from 3000-37000, so does the overall heat transfer coefficient from 5 to 17 kW/m<sup>2</sup> - K (Figure 5-12). While the model values overlap for



all the subcoolings, the measured values for a fixed flow rate have the highest overall heat transfer coefficient for the highest subcooling, and the lowest overall heat transfer coefficient for the lowest subcooling. An MAE of 1.30, 0.50 and 0.55,  $\text{kW/m}^2 - \text{K}$  for the overall heat transfer coefficient was calculated for the 4, 8 and 12 K subcooling respectively.

Measured fluxes of condensation, and consequently measured overall heat transfer coefficient, are an order or two orders of magnitude lower than the values usually reported for dropwise condensation as found in the literature [32]. This apparent discrepancy is resolved when the internal-resistance-dominant measured values here are contrasted to almost zero internal-resistance values obtained through wall-temperature-control experiments utilized in most literature.

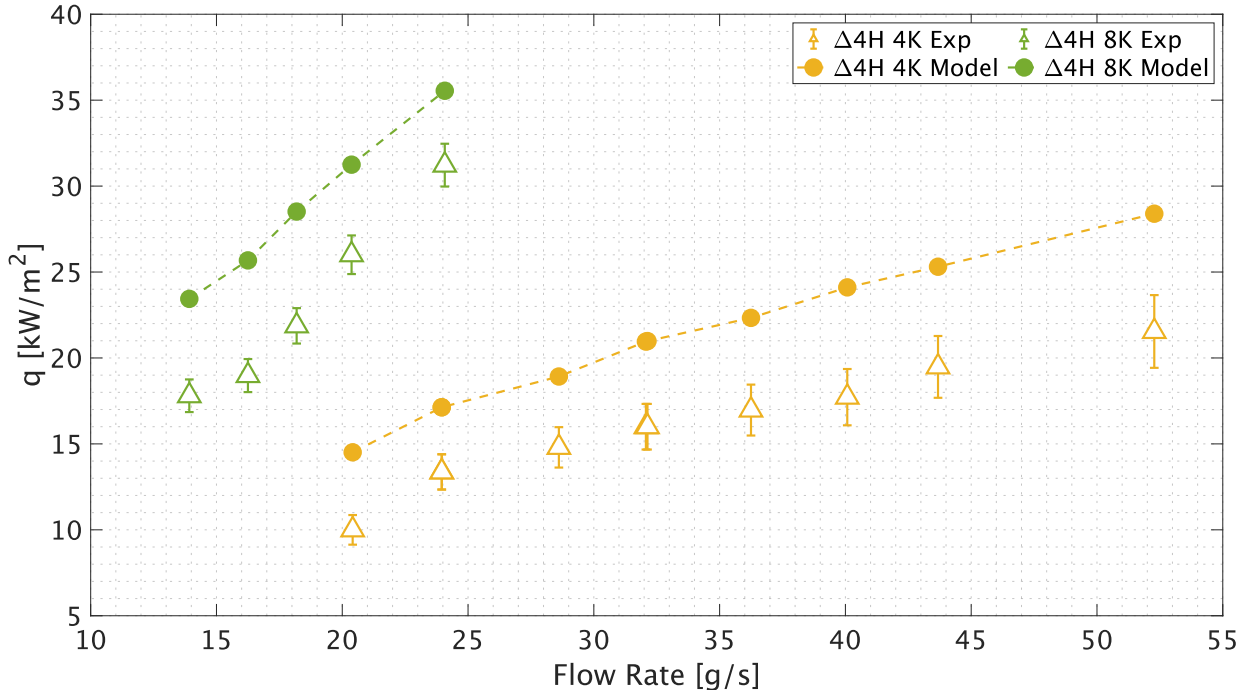


Figure 5-13. Condensation flux vs different flow rate for different subcoolings for the single plate test article with hydrophobic promoter.

One of the 5-plate configurations,  $\Delta 4$ , was coated with the same hydrophobic promoter and was tested at different subcoolings for different flow rates. Figures 5-13, and 5-14 are the depiction of the effect of said variation on measured and calculated flux of condensation, and overall heat transfer coefficient respectively. Both measured and calculated condensation flux increase for increased flow rate at either subcoolings. However, there is a large difference between the measured, and calculated fluxes of condensation. An MAE of 2.4, and 2.1 kW/m<sup>2</sup> for the flux of condensation was calculated for the 4, and 8 K subcooling respectively. For the case of 4 K subcooling the difference decreases initially, but later increases. Similar trend is observed at 8 K subcooling.

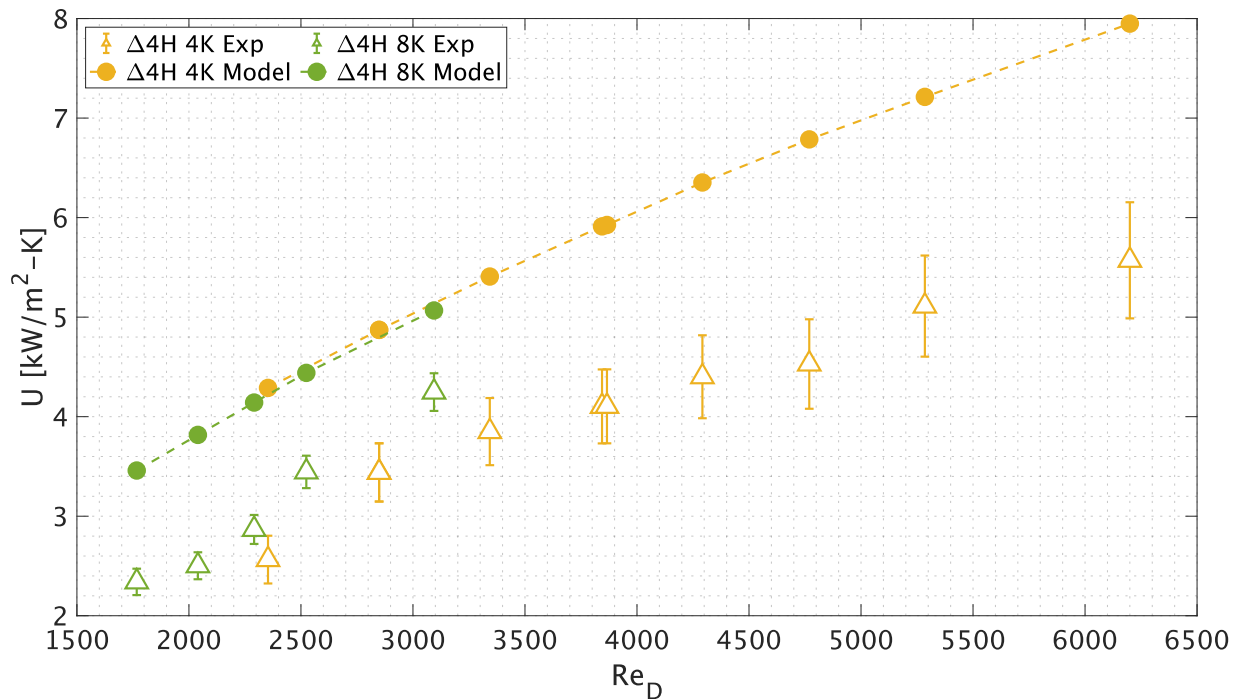


Figure 5-14. Overall heat transfer coefficient vs hydraulic-diameter based Reynold number for different subcoolings for the single plate test article coated with the dropwise promoter. For this article the plate-averaged length of condensation was measured to be 229.2 mm, and the entire condensation area to be  $724.7 \pm 0.119$  cm<sup>2</sup>. Chamber pressure varied between 37.3-38.9, 64.2-65.7 kPa for 4, and 8 K subcooling respectively during the experiment. A 5.5  $\mu$ m promoter thickness and a thermal conduction of 0.25 W/m – K was assumed for the calculated values.

The overall heat transfer coefficient increases almost linearly for the calculated values, but the measured value at 8K face a reduction in their rate of growth. Initially, flux is flow controlled, but later it switches to phase-change controlled. The difference between the measured and calculated values increases with increased Reynold number pointing to a heat transfer hindering mechanism linked to phase change. An MAE of 0.43, and 0.73  $\text{kW/m}^2 - \text{K}$  for the overall heat transfer coefficient was calculated for the 4, and 8 K subcooling respectively.

### 5.2.6.4 Comparison Plots

Figure 5-15 depicts the positive effect of dropwise promoter on the flux of condensation for the single plate configuration.

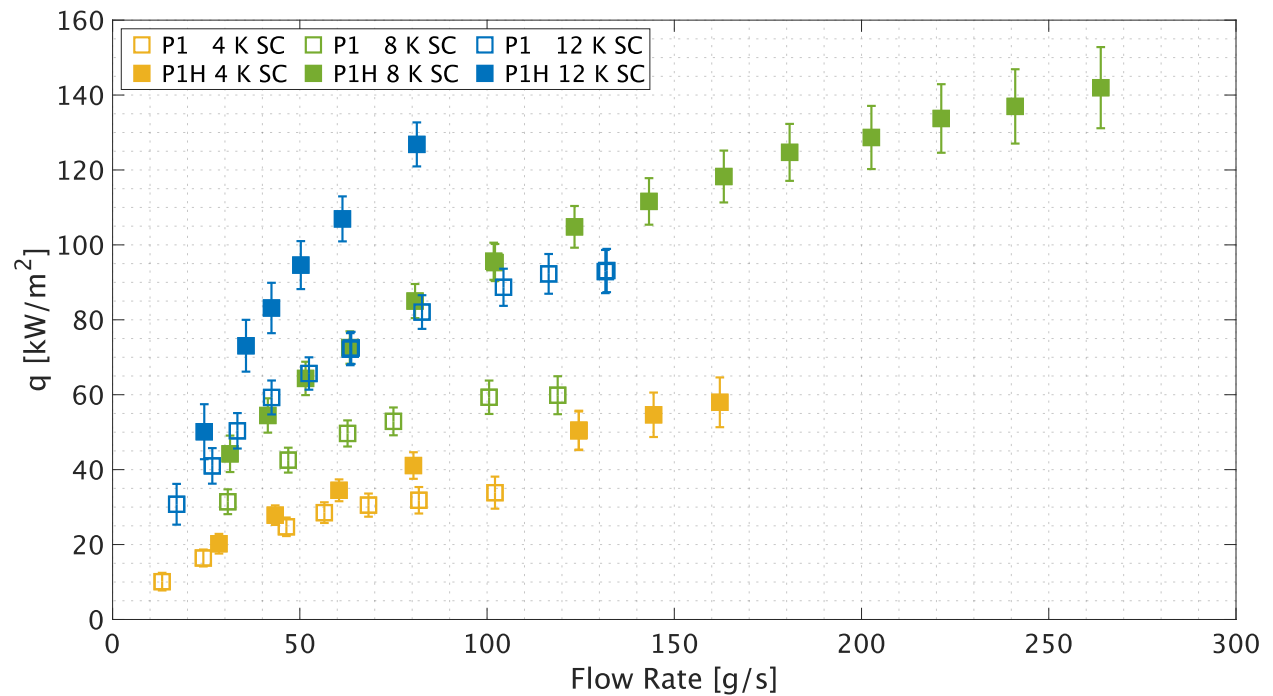


Figure 5-15. Flux of condensation vs plate flow rate comparison between P1H and P1 for different subcoolings.

Filled squares represent the coated plate, and the hollow ones correspond to the uncoated plate. Due to observed plateau during experimentation, the single non-coated plate was only tested for flow rates ranging between 15-132 g/s. Such observations were absent for the coated plate and hence higher flow range of 30-260 were tried. For the un-coated plate, flux of condensation varied from 10-90 kW/m<sup>2</sup> while the coating enabled higher flux of condensation in the range of 20-130 kW/m<sup>2</sup> to be achieved. For example, at 80 g/s, and 12 K subcooling the coated plate condenses about 80 kW/m<sup>2</sup>, whereas for the same conditions the coated plate condenses about 130 kW/m<sup>2</sup> - a 63% increase.

For any given subcooling, as the flow rate increases the difference between condensation flux increases. There is a maximum difference of 5, 30, and 24 kW/m<sup>2</sup> between the measured value for the flux of condensation at subcooling values of 4, 8, 12 K respectively. non-coated plate performance plateaus with increased flow rates, yet due to higher phase change coefficient of heat transfer the coated plate still is flow controlled for the tested values.

Figures 5-16, and 5-17 are the overall heat transfer coefficient comparisons of the single plate experiment to the 6 mm, and 4 mm plate-to-plate spacing respectively. For comparison, single plate modeling prediction is also included in both figures. The following remarks are true for suspended experiment uncertainty.

In Figure 5-16 for the case of 4 K subcooling, focusing on the mustard-colored shapes, it is obvious that, for the few available comparison data points, although the two test articles have equal overall heat transfer coefficient at the beginning, the single plate outperforms the  $\Delta 6$  configuration as  $Re_D$  increases. The same is true for the 8 K subcooling case.

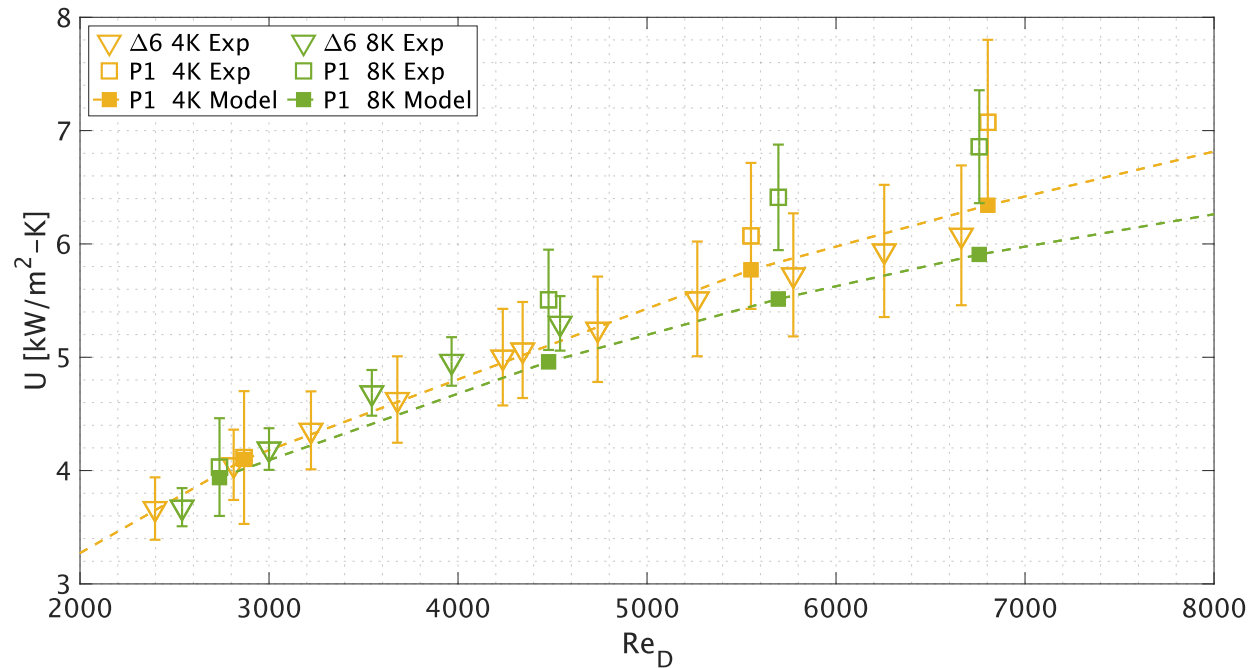


Figure 5-16. Overall heat transfer coefficient vs hydraulic-diameter based Reynolds number comparison between 6 mm plate-to-plate spacing configuration and the single plate.

In the comparison done on P1 versus  $\Delta 4$ , while it is true that both test articles benefit from an increased overall heat transfer coefficient for higher  $Re_D$ , the single plate is flow-resistance dominated, whereas  $\Delta 4$  is phase change dominated (Figure 5-17).

For the case of 4 K subcooling overall heat transfer coefficient is at least  $0.66 \text{ kW/m}^2 - \text{K}$  – K, and at most  $1.9 \text{ kW/m}^2 - \text{K}$  lower than the single plate.

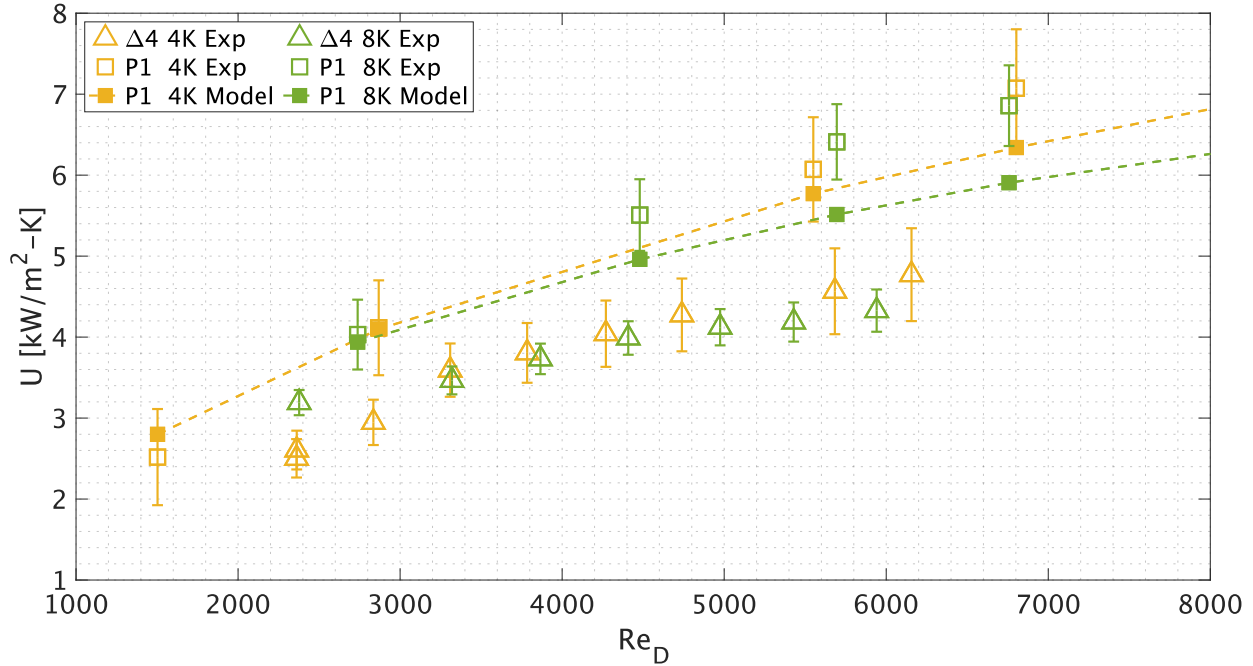


Figure 5-17. Overall heat transfer conductance vs hydraulic-diameter based Reynolds number comparison between  $\Delta 4$  and P1.

And, for the case of 8 K subcooling the heat transfer coefficient difference range is larger with a minimum and maximum difference  $0.1 \text{ kW/m}^2 - \text{K}$  of  $2.27 \text{ kW/m}^2 - \text{K}$  respectively.

Similarly, to understand the effect of hydrophobic coating on the 4 mm plate-to-plate spacing the overall heat transfer coefficient for the coated and uncoated variation of this configuration is contrasted with the 6 mm plate-to-plate spacing. In Figure 5-18 hollow shapes correspond to uncoated configurations, while the filled shapes represent the coated configuration. Downward, and upward triangles belong to the  $\Delta 6$ , and the  $\Delta 4$  configuration, respectively. At 4 K subcooling although there is an improvement in the overall heat transfer coefficient from dropwise condensation, the improvement is not

enough to overcome the underlying heat-transferring-hindering mechanism for low Reynold numbers.

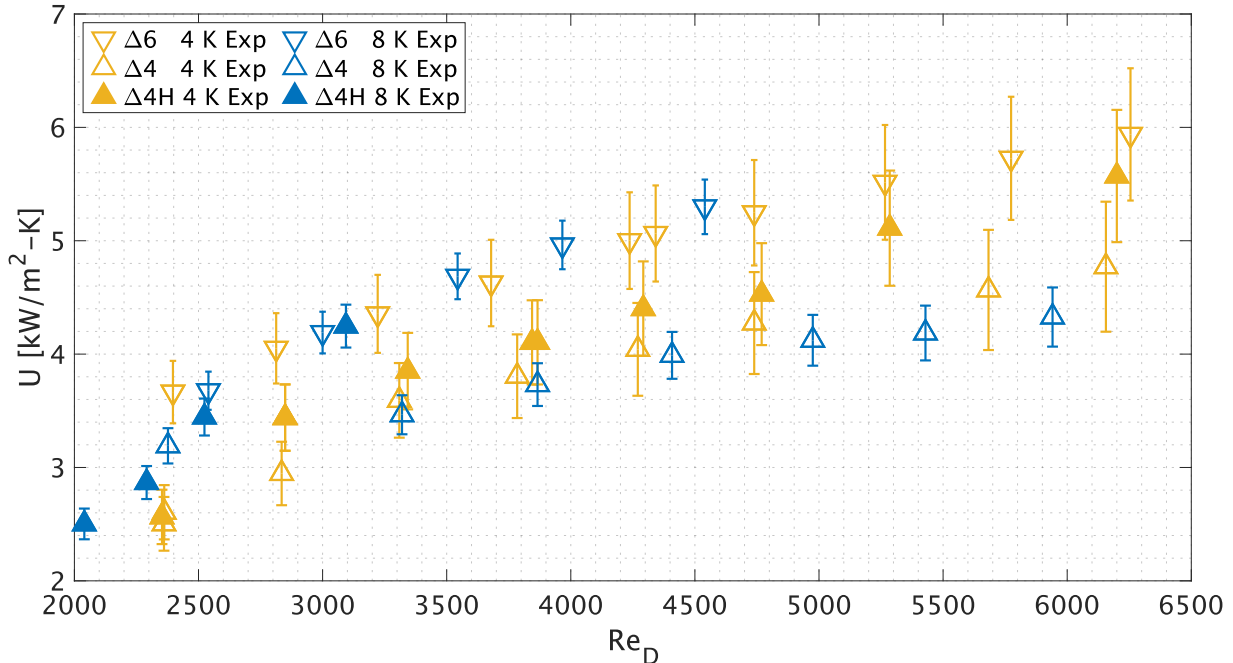


Figure 5-18. Overall heat transfer coefficient vs hydraulic-diameter based Reynolds number comparison between  $\Delta 6$ ,  $\Delta 4$ , and  $\Delta 4H$ .

For the same subcooling, hydrophobic overall heat transfer coefficient approaches the sparsely spaced configuration, indicating the possibility of matching or even higher values for faster flow rates. On the other hand, at 8 K subcooling the effect of dropwise condensation is pronounced. At this subcooling the denser-packed and coated configuration,  $\Delta 4H$ , reaches the performance of the sparsely packed uncoated configuration,  $\Delta 6$  at Reynolds number of 3200. Due to heater limitation, higher heat fluxes could not be tested attesting to even higher overall heat transfer coefficients for the  $\Delta 4H$  configuration at higher flow rates at 8 K subcooling.

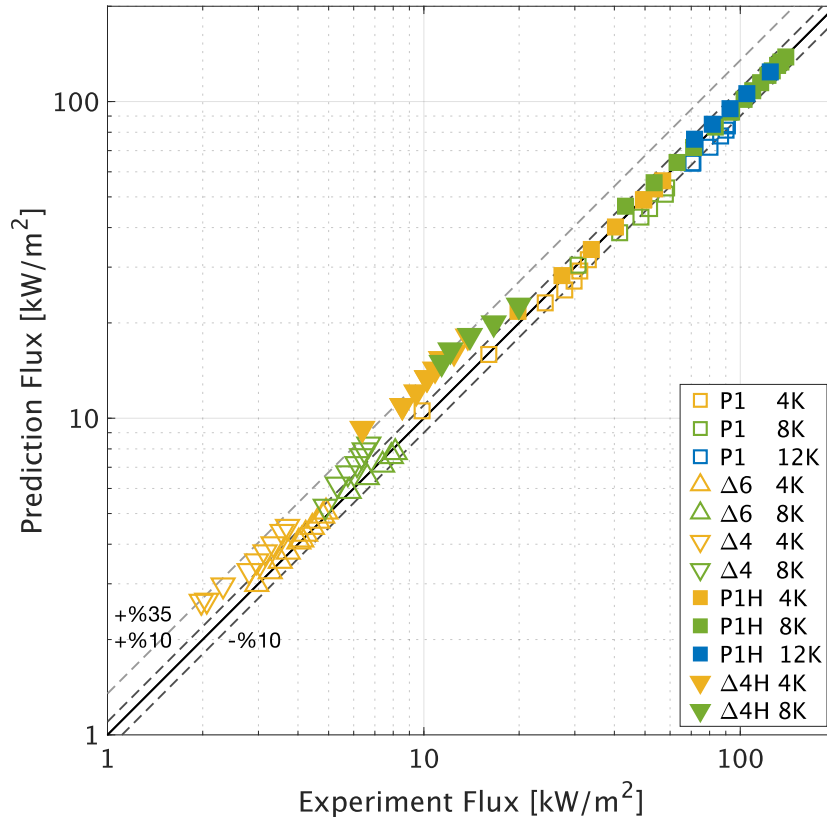


Figure 5-19. Log-log Heat flux of condensation parity plot for all the test configuration at any available subcooling. %35, %10, and -10% error lines.

Figures 5-19 and 5-20 are, respectively, the log-log parity plot for the heat flux of condensation, and overall heat transfer coefficient for all the configurations and conditions. On the abscissa, lie the experimental value, while on the ordinate are the model prediction values.

For reference the  $\pm 10\%$  error interval, as well an %35 upper error limit has been added as dashed lines. Nomenclature to interpret the data points is similar to that laid out in section 5.2.6.1. Excluding  $\Delta 4$ , and  $\Delta 4H$  configurations, the rest of the data lay well within the %10 interval suggesting a strong agreement between the measured and predicted values. The tight plate spacing used in the  $\Delta 4$  configuration leads to an actual heat transfer hindering not predicted by the model, and, thus, a model overprediction is



observed. This overprediction is observable when considering the downward facing triangles in Figures 5-19 and 5-20. These data points are within the  $\pm 3\%$  neighborhood of the 35% dashed line indicating that the model prediction is accurate with a 38% uncertainty.

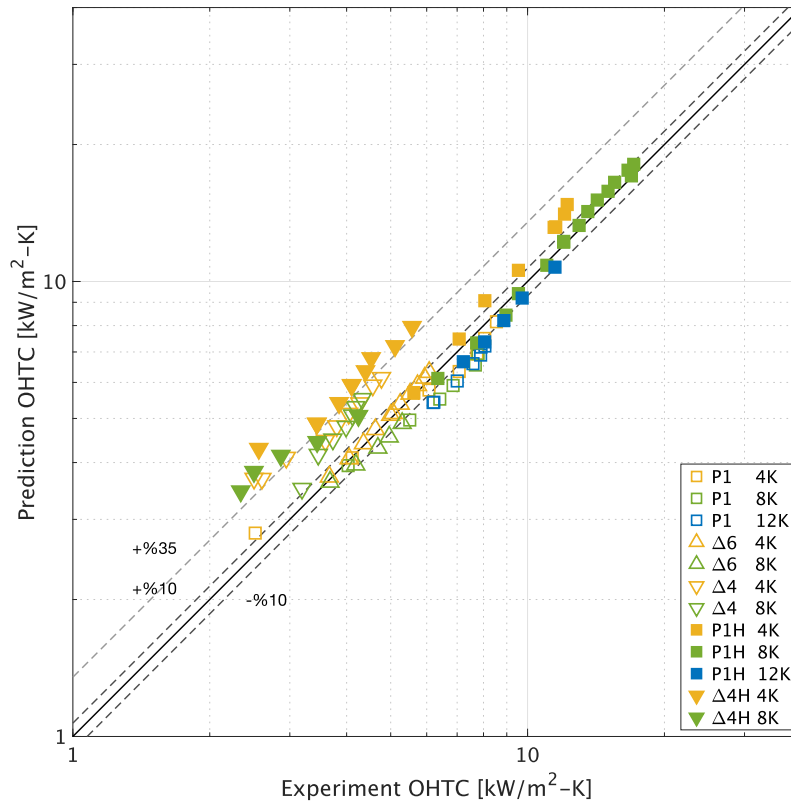


Figure 5-20. Log-log overall heat transfer coefficient parity plot for all the test configuration at any available subcooling. %35, %10, and -10% error lines.

During experimentation, multiple videos and pictures were taken at different experiment conditions which were used to visually confirm the presence of dropwise condensation.

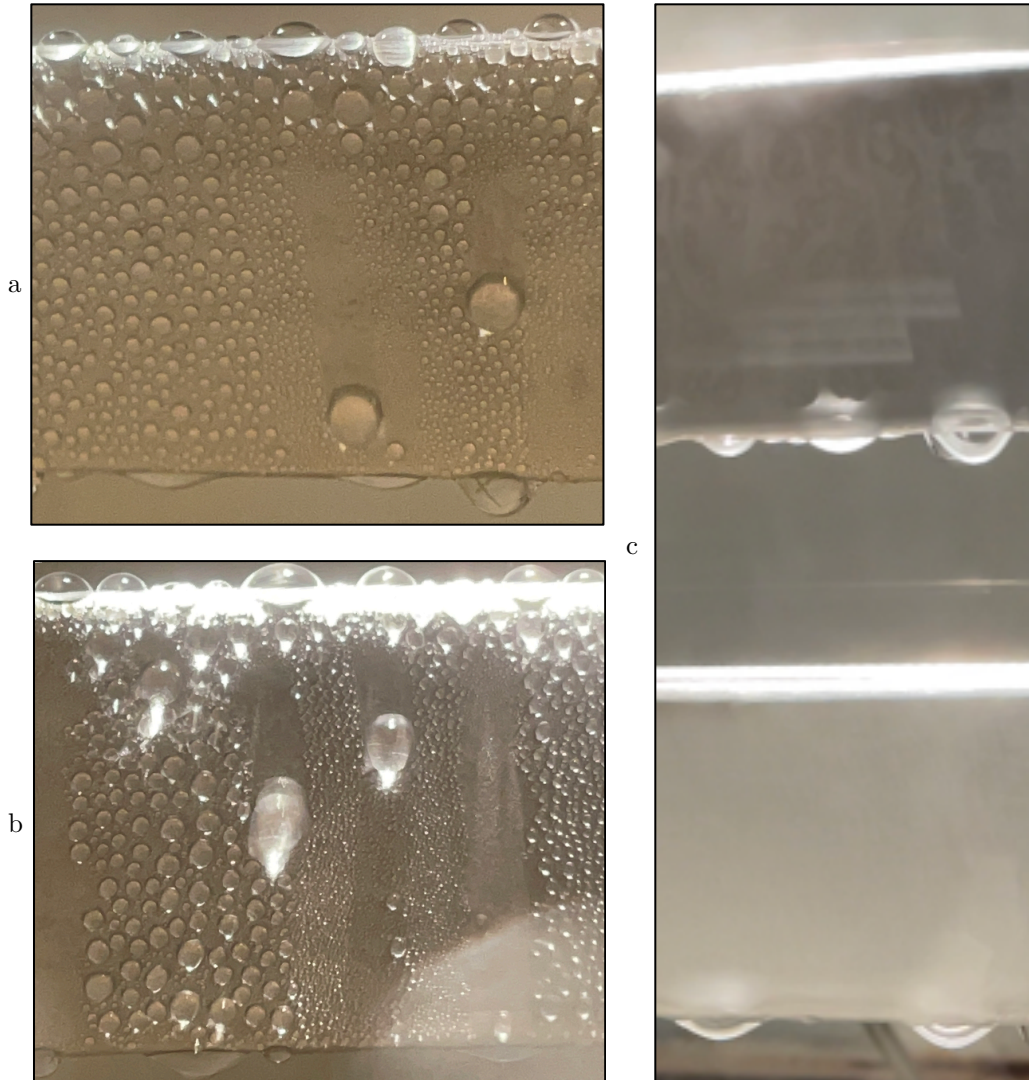


Figure 5-21. a., and b. Effect of dropwise condensation promoter at  $\Delta T_{sub} = 16K$ ,  $T_{in} = 42.7\text{ }^{\circ}C$ ,  $T_{out} = 44.53\text{ }^{\circ}C$ ,  $P_{sat} = 19.54\text{ kPa}$ ,  $\dot{m}_{plate} = 24\text{ g/s}$ . c. No dropwise promoter presence at  $\Delta T_{sub} = 4K$ ,  $T_{in} = 61.12\text{ }^{\circ}C$ ,  $T_{out} = 63.3\text{ }^{\circ}C$ ,  $P_{sat} = 23.8\text{ kPa}$ ,  $\dot{m}_{plate} = 44\text{ g/s}$ . Images shot using iPhone 12

For plates coated with the dropwise promoter (Figure 5-21. a. and b.) clear hemispherical droplets with different size distribution are observed. What is also observable from these frames is the sweeping motion of droplets draining under the influence of gravity. On the contrary, filmwise condensation gives rise to complete wetting of the condenser plates, and creation of a liquid film submerging the condenser plates (Figure 5-21. c.).

### 5.3. Chapter Conclusion

In this chapter the results of the correlation driven model used to predict the size reduction for multistage flash was experimentally Tested. The effects of plate spacing, and PTFE hydrophobic coating on multiple subcoolings pertaining to variable MSF plant conditions at different flow rates were tested. The following are the salient findings of this chapter:

1. The sparsely packed  $\Delta 6$  perfumes as well as the single plate P1 configuration.
2. The tightly packed  $\Delta 4$  is not performing as well as the sparsely packed  $\Delta 6$  configuration.
3. Dry inner plates are observed both for  $\Delta 4$  configuration
4. Strong enhancement of heat transfer coefficient and heat flux of condensation is observed for the coated condenser.
5. Although hydrophobic coating enhances  $\Delta 4$  performance, dry patches are still visible for this configuration
6. The  $\Delta 4H$  condenser performs as well as, if not in some cases better than, the  $\Delta 6$ .
7. For the case of P1 and  $\Delta 6$  condensers, the model predicts measurement with impeccable accuracy or  $MAE_P < 7\%$ .
8. Calibrated with a dropwise promoter thickness, the model predictions of hydroponic coating are highly accurate  $MAE_P < 10\%$ .
9. In the case of the densely packed 5-plate condenser, both coated and non-coated, a model overprediction of at most 35% is observed.

Due to either the limitation imposed by the heat input, or the maximum flow rate achievable neither the single plate nor the 5-plate configuration was tested at MSF equivalent flow rates or Reynolds numbers. However, from the strong agreement between the single plate experiment and the model for the tested ranges it is reasonable to accept that an actual condenser running at even higher flow rates corresponding to MSF condition, a fabricated condenser with plate-to-plate spacing of at least 6mm, will perform in agreement with the condensation model proposed here. Furthermore, it is possible that the behavior of a multiport plate condenser having a 4 mm plate-to-plate spacing and coated with 5.5  $\mu\text{m}$  of the PTFE coating is predictable if an experimentally calibrated phase change coefficient of heat transfer is used instead of the one suggested by Rose.



## Chapter 6: Fouling



## 6.1. Background

The accumulation of unwanted deposit on the heat exchanger surface is referred to as fouling. As discussed earlier, the presence of such deposits introduces a resistance to heat transfer, thereby reducing the overall heat transfer coefficient. Foulant is categorized into crystalline, biological material, product of chemical reactions, or particulate matter. [61] All types of fouling are caused by contaminants, albeit in small quantities, present in the working fluid. Crystalline foulant causes crystallization fouling which occurs when certain salts dissolved in the working fluid deposit on the surface of the heat exchanger. Biological material contaminant adheres to the surface, and promotes biological organism growth, i.e. bacterial growth. Literature on fouling categorizes chemical reaction to corrosive chemical reaction, leading to wear of heat exchanger surface, and organic chemical reaction, the reaction of organic chemicals. In this work we shall combine both types and refer to the combination simply as chemical fouling. Particulate matter deposition is caused when particles dissolved from elsewhere in the process travel beyond that location and deposit on the heat exchanger surface.

Around the globe fouling costs industries millions of dollars [61]. An extensive study done on the cost of fouling in the refinery industry, it was found out that adjusted for inflation \$50-100 million are spent in a refinery processing 100,000 barrels of crude oil per day [62] for fouling abatement. Another study performed in the UK suggests that the cost of fouling was in the range of £300-500 million at 1979 [63]. A study done throughout the EU concluded that the cost of fouling around year 1992 was about 10 billion ECU out of which 20% was due to increased fuel cost. In a more recent study, it was found that

fouling is estimated to cost the industrialized countries roughly 0.25% of their gross domestic product. [64]

Fouling can impose greater costs in a few ways. To account for the reduction in overall heat transfer coefficient caused by fouling, heat exchangers must be made larger than what they would have been absent fouling. This requirement not only increases the size, but also increases the equipment requirements, such as pumping, to operate the heat exchangers which in turn drives up the total cost. On top of that, this larger equipment requires more footprint and typically more power and energy, and hence there is a need to account for larger land and utilities costs.

It is often the case with heat exchangers that complete mitigation of fouling is not possible, and either because the heat exchangers are completely clogged, or because the continued operation would push the performance below the acceptable financial limit the heat exchangers are regularly shutdown and cleaned. Shutdowns leads to production downtime which ultimately translates into reduced income. If the continuous operation of heat exchanger is curtailed during the downtimes, heat exchanger redundancy is incorporated into the design. This redundancy is in the form of additional similar heat exchanger units which, although not proportionally, will increase the final cost of the system.

During operation, an initially clean heat exchanger will accumulate fouling mass, and in doing so its cross section will reduce. Lower cross section will give rise to higher fluid velocity inside the heat exchanger and hence higher fluid-wall shear stress. It is usually the case that higher shear stress leads to lower fouling deposition, and hence a spatial

steady state fouling thickness is achieved. While a steady state usually is usually observed, it is not guaranteed.

In situations in which the fouling factor has not accurately been captured, fouling can also drive up the cost post-design. In the case of overestimated fouling factor, i.e oversized equipment is used, the flow cross section area is larger and flow rate is slower. The slower flow rate reduces the rate of deposition removal, induced by fluid shear, leading to either a higher steady state fouling thickness or reaching no steady state condition at all. In either case, the main heat exchanger needs to be cleaned up sooner than anticipated. This increased cleaning frequency will cause the backup heat exchanger to eventually undergo cleaning at the same time the regular heat exchanger is cleaned, causing complete production halt.

If the fouling factor is underestimated, i.e undersized equipment is used, the heat exchanger cannot maintain the design requirements which leads to more frequent shutdowns, and ultimately to loss of productivity. Arguably, choosing the right value for fouling factor is the difference between profit or loss. The literature in fouling of heat exchangers consists of suggested values for different applications. For example, Tubular Exchanger Manufacturers Associated (TEMA) in their 1979 edition provide tabulated values for a handful of applications conditions. Kakaç and Liu and Rohsenow do provide extensive tabulated value as well [65, 66, 67]. Of particular interest are the fouling factors provided for brackish water, city or well water, hard water, and river water which vary from 0.262 to 0.528E m<sup>2</sup> – K/kW for shell and tube heat exchangers operating at 1.22 - 1.83 m/s on the tubes side and 0.61 m/s on the shell side the heat exchangers. As it is



with most industries, application results from one industry rarely translate well to another, a well-recognized fact by TEMA in their ninth edition in which they point out different factors effecting fouling, such as local velocities, tube material, and heat exchanger geometry.

Mwaba et al. performed crystallization fouling experiment with quasi salt-water containing  $3 \text{ kg/m}^3_{\text{H}_2\text{O}}$  concentration of  $\text{CaSO}_4$  at inlet temperature of  $40 \text{ }^\circ\text{C}$ , and Reynolds number set to 23,00 corresponding to  $0.6 \text{ m/s}$  on a stainless-steel channel with dimension of  $620 \times 46 \times 16 \text{ mm}$  and produced a semiempirical correlation for the local time rate change of foulant resistance based on local wall temperature using which a steady state local foulant thickness can be evaluated [68]. Ritter et al. performed over 2000 experiments on two different quasi salt-water solutions one made with  $\text{CaSO}_4$ , and the other with  $\text{Li}_2\text{SO}_4$ , both of which are inversely soluble salts as discussed in detailed in section 6.3.1 [69]. Constant composition salt solution was pumped through brass or carbon steel 12280 mm-long tubes with inside diameters of 13, 25, and 51 mm. Solution concentration ranged from  $1.73\text{-}2.11 \text{ kg/m}^3_{\text{H}_2\text{O}}$ ,  $305\text{-}338 \text{ kg/m}^3_{\text{H}_2\text{O}}$  and surface supersaturation,  $\Delta C^*$  defined in section 5.3.1, from  $0.065\text{-}0.173$ , and  $22.8\text{-}25.2$ , wall shear stress from  $0.15\text{-}17 \text{ Pa}$ , and  $0.077\text{-}36 \text{ Pa}$ , and salt solution velocity from  $0.3\text{-}3 \text{ m/s}$ ,  $0.18\text{-}4 \text{ m/s}$  for  $\text{CaSO}_4$ , and  $\text{Li}_2\text{SO}_4$  respectively. Salient findings were that crystallization fouling is characterized by a no-fouling period, induction period, which is inversely proportional to square of fouling rates, and that supersaturation and surface temperature, but not the wall shear stress or the fluid velocity were the major factors affecting both the induction period and the fouling rates.

The troublesome presence of fouling has been known ever since the first heat exchangers were deployed. Fouling is one of the challenges, if not the most challenging part, in maintaining and operating any heat exchanger. While other fouling mechanisms contribute to fouling in general, due to their operating conditions thermal desalination heat exchangers are mostly susceptible to crystallization fouling. Although fouling mechanisms differ from each other there are fundamental similarities which will be discussed in the following subsection.

Mayer et al. performed supersaturated  $\text{CaCO}_3$  fouling experiments on microchannels with dimensions 0.2 mm deep, 0.4 mm wide, and 24 mm long for three different flow rates corresponding to  $\text{Re} = 66, 198, 264$  for a controlled inlet temperature set to  $25^\circ\text{C}$ , and recorded surface as well as fluid inlet and outlet temperatures, in addition to pressure drop across the test piece [70]. They concluded that fluid velocity is inversely correlated to the rate of fouling, and although, due to higher wall shear stresses, pressure drop starts at higher values for the fastest moving fluid, but as the fouling continues and the fluid passage becomes smaller, the pressure drop from the slowest moving fluids catches up and reaches a value of up to 13 times larger than the corresponding fastest moving fluid. Steady state fouling factors are reported to be in the range of ( $10^{-5}$  to  $10^{-3}$  W/K) in this work.

Pääkkönen et al. performed a non-linear regression fitting on a few  $\text{CaCO}_3$  modeling of crystallization fouling of infinitely long parallel flat plates using their experimental data points [71]. Out of the four studied models, the model assuming a reaction-controlled process and considering the effect of velocity on deposition rate had the highest  $R^2$  number. Due

to the relatively low fluid velocity, between 0.15 and 0.35  $m/s$ , the models only accounted for the deposition rate, and not the removal rate. The results of both the model and the experiment attest to the inverse relation between deposit rate and fluid velocity.

In an investigation of optimize dosage requirement for different antifouling agents for MSF, Hamed et al. state that the industry design value for fouling resistance is of the orders of  $0.215 \text{ m}^2 - \text{K/kW}$  [72], and emphasizes the environmental and obvious economic benefits of having reduced antifouling treatments.

## 6.2. General Theory of Fouling

Conservation of mass dictates that for a control volume around the foulant, the rate at which the foulant accumulates is equal to the rate at which it deposits, less the rate at which it is removed from the surface, i.e

$$\frac{dm_f}{dt} = \phi_d - \phi_r, \quad (6-1)$$

in which  $m_f$  is the mass of foulant,  $\phi_D$ ,  $\phi_R$  are the rates of foulant deposit and removal respectively.

As the process of deposition continues, the fluid cross section declines. Although surface roughness is going to alter from that of clean surface, if constant surface roughness assumption is made, the reduction in cross section area is going to impose a greater pressure drop across the heat exchanger, and, for a constant flow power of the pump, cause lowered mass flow rate, subsequently lower fluid velocity. On the other hand, the reduction in cross section area will increase the fluid velocity for a fixed pressure drop within the heat exchanger. The reduced mass flow rate due to increased pressure drop,

and increased velocity caused by lowered cross section are two competing effects that will impact the process in different ways dependent upon the pump curve. It usually is the case that the reduction in mass flow rate due to increased pressure drop is lower than that of velocity increase due to cross section reduction.

Reduced local supersaturation - discussed later in this chapter - reduces the rate of deposition,  $\phi_D$ , while the elevated fluid velocity increases the rate of foulant removal,  $\phi_R$ , to an extent both rates become equal. When this happens, the rate of deposit accumulation would equal to zero, and the system is said to have reached an equilibrium as far as fouling is concerned, i.e,

$$\frac{dm_f}{dt} = 0 \quad (6-2)$$

A challenge remains to quantify the steady state thickness of the foulant. Simplified models to account for the foulant thickness,  $x_f$ , has been proposed by Kern and Seaton [73], suggesting the rate change of foulant removal is proportional to the wall shear stress,  $\tau$ , and the thickness of the foulant,  $x$ ,

$$\phi_r = K_2 \tau x_f, \quad (6-3)$$

in which  $K_2$  is the constant of proportionality.

On the other hand, the rate change of fouling over time can be recast in terms of foulant thickness. For a constant deposit area, and foulant deposit density we have

$$\frac{dm_f}{dt} = \frac{d(\rho_f x_f A)}{dt} = \rho_f A \frac{dx_f}{dt}. \quad (6-4)$$

Substituting equation (6-3) and (6-4) in equation (6-1) yields

$$\rho_f A \frac{dx_f}{dt} = \phi_d - K_2 \tau x_f. \quad (6-5)$$

Upon assumption of constant deposition rate, wall shear stress, along with previous assumptions made leading to equation (6-4), equation (6-5) can be integrated once with the initial condition of  $x_f|_{t=0} = 0$  to yield:

$$x_f = \frac{\phi_d}{K_2 \tau} \left( 1 - e^{-\frac{K_2 \tau}{\rho_f A} t} \right). \quad (6-6)$$

Equation (6-6) suggests that there is a finite value for the foulant thickness which is equal to the limit of that equation as  $t \rightarrow \infty$ :

$$x_{f,\infty} = \lim_{t \rightarrow \infty} \left[ \frac{\phi_d}{K_2 \tau} \left( 1 - e^{-\frac{K_2 \tau}{\rho_f A} t} \right) \right] = \frac{\phi_d}{K_2 \tau}. \quad (6-7)$$

The value of  $\tau$  for a given mass flow rate and cross section is readily available, and hence the real challenge lies in quantifying the values of  $K$ , and  $\phi_D$ . Kern and Seaton's model is an attempt to generalize fouling, and in doing so it neglects the fouling mechanism specific to each mode of fouling. While the deposit removal mechanism can be thought of as similar across different fouling mechanisms - with the exception of foulant adhesion force - fouling deposit rate depends highly on the deposition mechanism. With the general theory of fouling briefly discussed here the next subchapter is dedicated to crystallization fouling, and its implication on thermal desalination.

## 6.3. Modeling of Crystallization Fouling

### 6.3.1. Type of Salts

Aqueous salts come in two forms: inversely soluble, and normally solubility. Normal solubility salts, such salt is NaCl, MgCl<sub>2</sub>, are salts which their capacity to dissolve in the solute increase with the increased solute temperature,

$$\frac{dC_{sat}}{dT} |_{normal} > 0. \quad (6-8)$$

Opposite to normal solubility salts, some salts lose their ability to dissolve in solution with increased temperature, i.e.,

$$\frac{dC_{sat}}{dT} |_{inverse} < 0. \quad (6-9)$$

In equations (6-8) and (6-9)  $C_{sat}$  is the saturation concentration, and  $T$  is the solution temperature.

When heat is applied to an inverse-soluble salt with a given concentration the temperature initially rises to  $T_1$  at which point the salt solution is at its maximum solubility limit i.e. saturated. If the heating process continues and the salt solution temperature is increased even further, to  $T_2$ , the solution is oversaturated with the salt, point C in Figure 6-1.a. At this point the solution has a large tendency to remove the oversaturated amount. The removal can occur either heterogeneously, or homogeneously. A heterogeneous removal occurs when the material deposits on a surface surrounding the solution. In contrast homogenous deposition occurs when crystals nucleate from within the solution itself, and after some initial period start growing. Heterogeneous nucleation requires less

supersaturation to activate than homogeneous nucleation does, and as such surface this surface nucleation mechanism is more common. Due to commonality of heterogeneous nucleation, or rather rarity of homogeneous nucleation, the prefix is usually omitted from fouling literature, and heterogeneous crystallization fouling is simply referred to as crystallization fouling.

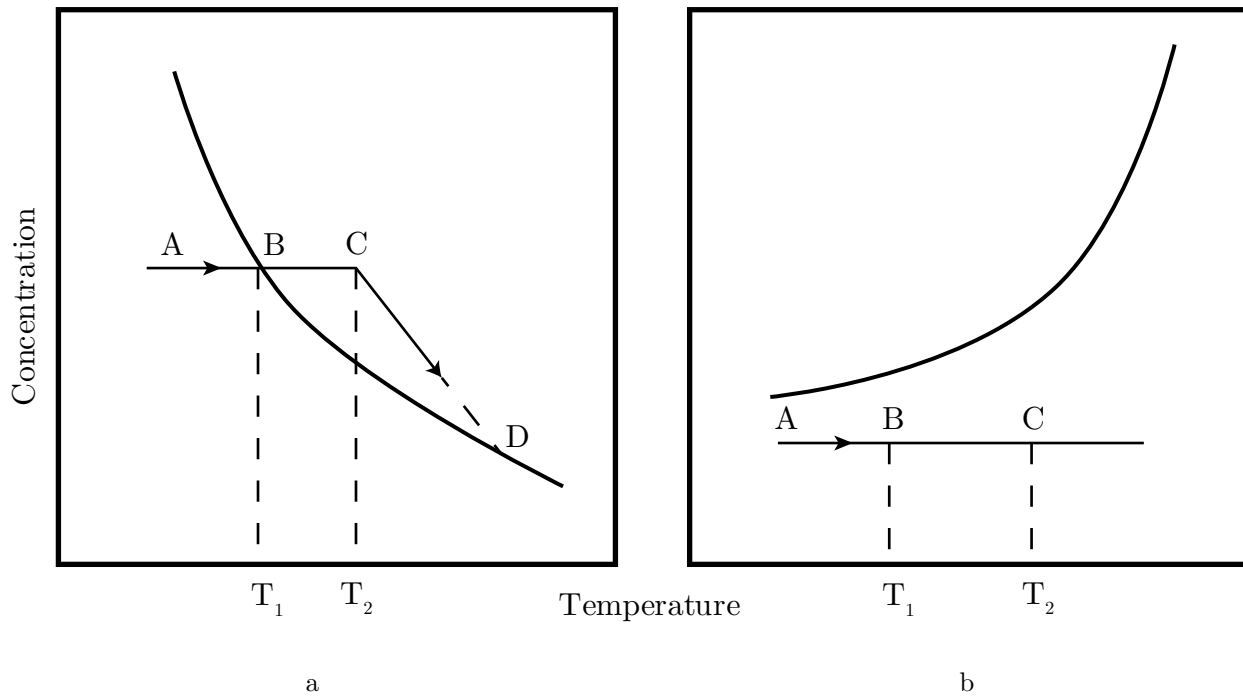


Figure 6-1. Concentration vs temperature graph for: a. invers-solubility salt, b. normal solubility salt.  
Solid line indicates equilibrium salt concentration

When heat is applied to a normal solubility salt solution (Figure 6-1.b), the temperature increases from  $T_1$  to  $T_2$ , and increases the solubility without causing any supersaturation to occur at any point in the process. For this reason, only the inversely soluble salts are problematic in heating processes such as those found inside and MSF condenser.

Table 6-1 contains some inversely soluble salts most of which are *Ca* salts. *Li*<sup>+</sup> and *Mg*<sup>2+</sup> ions are the next to follow. Seawater, the main source of feedwater for MSF plants, contains mostly NaCl (55 % of the total 2.5 % salt present in seawater [74]), which is not an inversely soluble salt and hence not a fouling agent for MSF heat exchangers. However, ocean water salinity contains 7.7 % Mg and 1.2 % Ca which when combined with their corresponding anion, albeit present at low mass fractions, form the salts responsible for the most common cause of fouling: CaCO<sub>3</sub>, Mg(OH)<sub>2</sub>, and CaSO<sub>4</sub>.

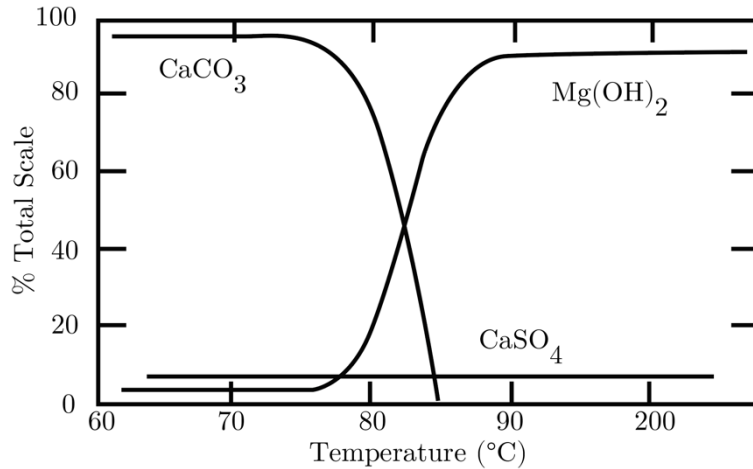


Figure 6-2. Total scale composition vs temperature for common seawater figure adopted from [75]

For low temperatures of up to 77 °C Delyannis and Delyannis report that most of scale crystallized on MSF heat transfer surfaces is composed of CaCO<sub>3</sub> with slight presence of CaSO<sub>4</sub> [75]. In the range of temperatures between 77 – 85 °C both alkaline scales, CaCO<sub>3</sub> and Mg(OH)<sub>2</sub>, are present. As the temperature exceeds 85 °C Mg(OH)<sub>2</sub> becomes the dominant form of scale. CaSO<sub>4</sub> remains only a minor fraction of total scale irrespective of operating temperature. In the interest of completion, it should be mentioned that ground water in certain areas contain Li ions which is used to extract lithium for lithium-



ion batteries. Of work done on Li ions the work of Ritter et al. on  $\text{LiSO}_4$  briefly discussed in this piece can be mentioned [69].

Literature available on crystallization fouling is vast, and in the interest of time and effort, the author has decided that the henceforth this work should be dedicated to the effects of  $\text{CaCO}_3$  only, as an example of salt fouling.

Table 6-1: Some inverse solubility salts [61]

Salt	Chemical formula
Calcium carbonate	$\text{CaCO}_3$
Calcium hydroxide	$\text{Ca}(\text{OH})_2$
Calcium phosphate	$\text{Ca}(\text{PO}_4)_2$
Calcium silicate	$\text{CaSiO}_3$
Calcium sulphate	$\text{CaSO}_4$
Lithium carbonate	$\text{Li}_2\text{CO}_3$
Lithium sulphate	$\text{Li}_2\text{SO}_4$
Magnesium hydroxide	$\text{Mg}(\text{OH})_2$
Magnesium silicate	$\text{MgSiO}_3$
Sodium sulphate	$\text{Na}_2\text{SO}_4$

### *6.3.2. Solubility of $\text{CaCO}_3$ in solutions with different temperatures.*

From initial reasoning provided for crystallization fouling it is understood that the rate of fouling is proportional to supersaturation. A formal definition of supersaturation is due, and given as follows:

$$\Delta C_j = C_j - C_{sat}, \quad (6-10)$$

Where  $\Delta C_j$  is the supersaturation,  $C_j$  is the solution concentration, and lastly  $C_{sat}$  is the saturation concentration of the solution. The subscript  $j$  represent the location at which supersaturation is gaged.

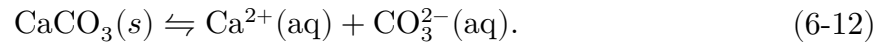
Nondimensionalized supersaturation sometimes is defined as

$$\Delta C_j^* = \frac{C_j - C_{sat}}{C_{sat}}. \quad (6-11)$$

### 6.3.3. $Ca^{2+}$ Equilibrium Concentration

In order to evaluate equation (6-10) saturation concentration must be known. Since saturation concentration turns out to be a function of temperature and this work is focused on the effect of fouling for different operating temperatures, it is imperative to develop a relationship with saturation limit and temperature. One way of achieving this goal is to look at reported values for solubility product values for  $CaCO_3$  disassociation in water.

A simplified disassociation reaction of  $CaCO_3$  in water is as follows:



Defining solubility product as

$$K_{sp} = [Ca^{2+}][CO_3^{2-}], \quad (6-13)$$

in which  $K_{sp}$  is the solubility product, and the bracketed terms are the molar concentration of the ions and understanding that at equilibrium equation (6-12) indicate

that for every mole of  $Ca^{2+}$  ion produced there is a mole of  $CO_3^{2-}$  produced, i.e.,  $[Ca^{2+}] = [CO_3^{2-}]$ , or

$$K_{sp} = [Ca^{2+}]^2 = [CO_3^{2-}]^2, \quad (6-14)$$

Tabulated values of solubility product for calcium carbonate at different temperatures can be used to calculate the equilibrium saturation concentration. Calcium carbonate solubility products for selected temperatures are retrieved and gathered in table 6-2.

Table 6-2: Solubility product,  $K_{sp}$  for  $CaCO_3$  as a function of temperature. [7]

Temperature [°C]	$K_{sp}$ [mol <sup>2</sup> /L <sup>2</sup> ]
10.0	$8.13 \times 10^{-9}$
15.0	$7.08 \times 10^{-9}$
20.0	$6.03 \times 10^{-9}$
25.0	$4.57 \times 10^{-9}$
40.0	$3.09 \times 10^{-9}$
60.0	$1.82 \times 10^{-9}$

Table 6-2 and equation (5-13) can be used to calculate the equilibrium, or saturation, concentration of  $Ca^{2+}$ . For instance, at 10 °C the saturation concentration of  $Ca^{2+}$  is

$$[Ca^{2+}] = \sqrt{K_{sp}}_{10\text{ }^\circ\text{C}} = \sqrt{8.13E-9} = 9E-5 \text{ M. This number corresponds to 9 mg/L of}$$

$CaCO_3$  dissolved in pure water with no atmospheric air present.

The following curve fit equation is used to find  $CaCO_3$  disassociation constant for a given temperature T [K], and salinity, S [g/kg<sub>H<sub>2</sub>O</sub>]:

$$\begin{aligned}
K_{sp} = & \ln (-171.94 - 0.0779T + 71.59 \log(T) \\
& + (-0.7771 + 0.0028426T + 178.34/T)S^{0.5} - 0.07711S \quad (6-15) \\
& + 0.0041249S^{1.5} \text{ [76]})
\end{aligned}$$

In reality, the solubility of  $CaCO_3$  occurs in sea water exposed to  $CO_2$  dissolved in air. The 31.6 Pa atmospheric partial pressure of  $CO_2$  is in equilibrium with the dissolved gas in the ocean water

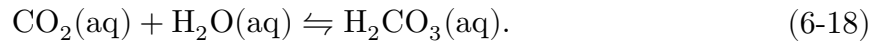


and controlled by Henry number such that:

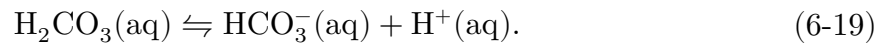
$$H_{CO_2} = \frac{[CO_2]}{P_{CO_2}}, \quad (6-17)$$

in which  $[CO_2]$  is the concentration, and  $P_{CO_2}$  is partial pressure of carbon dioxide in the environment.  $H_{CO_2}$  is Henry number for carbon dioxide which is tabulated as a function of temperature.

The dissolved carbon dioxide quickly hydrates to form carbonic acid



The formed carbonic acid quickly breaks into bicarbonate anion, and hydrogen cation



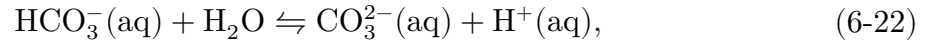
If concentration of species in equation (6-19) are cast in the form of

$$K_1 = \frac{[\text{H}^+][\text{HCO}_3^-]}{[\text{H}_2\text{CO}_3] + [\text{CO}_2]}, \quad (6-20)$$

they can be related to each other through first carbonic acid disassociation constant,  $K_1$  which for a given salinity, and temperature, can be determined using Millero correlation [77],

$$K_1 = \exp(2.128 - 2275/T - 1.468 \ln(T) + (-0.138 - 9.33/T)S^{0.5} + 0.07264S^{1.5}). \quad (6-21)$$

Bicarbonate itself disassociates into carbonic, and hydrogen ion



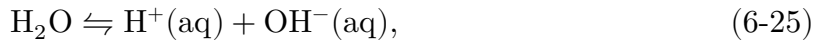
proportional in accordance with second disassociation constant for carbonic acids,  $K_2$ :

$$K_2 = \frac{[\text{H}^+][\text{CO}_3^{2-}]}{[\text{HCO}_3^-]}. \quad (6-23)$$

Much like  $K_1$ ,  $K_2$  can be calculated for a prescribed salinity,  $S$ , and temperature,  $T$ , using the following curve fit equation:

$$K_2 = \exp(-0.84226 - 3741.12/T - 1.4371 \ln(T) + (-0.1284 - 24.41/T)S^{0.5} + 0.1195S - 0.00912S^{1.5}). \quad (6-24)$$

Sea water dissociates into hydrogen, and hydroxyl ions



and becomes in equilibrium with the ions according to

$$K_w = [\text{H}^+][\text{OH}^-], \quad (6-26)$$

where the water disassociation constant,  $K_w$ , is given by

$$\begin{aligned} K_w = \exp(2148.98 - 13487/T - 23.652 \ln(T) \\ + (-5.977 - 118.67/T + 1.0495 \ln(T))S^{0.5} \\ - 0.01615 \cdot S^{1.5}). \end{aligned} \quad (6-27)$$

In order to balance the charges in the solution the sum of charges of the solution at any given time should be zero for this to be true the sum concentration of each ion multiplied by its corresponding charge is zero, i.e.:

$$z_i[x_i] = 0, \quad (6-28)$$

where  $z$  is the charge, and  $[x]$  is the concentration of ion  $x$  represented in Einstein notation.

Applying equation (6-28) to the charges present in  $\text{CaCO}_3$ -water system, the following is true:

$$2[\text{Ca}^{2+}] + [\text{H}^+] = [\text{OH}^-] + [\text{HCO}_3^-] + 2[\text{CO}_3^{2-}]. \quad (6-29)$$

For a prescribed temperature, salinity,  $\text{CO}_2$  partial pressure, the system of equations (6-14), (6-15), (6-17), (6-20), (6-21), (6-23), (6-24), (6-26), (6-27), and (6-29) can be solved iteratively, to find the concentration of dissolved  $\text{Ca}^{2+}$  in the carbonate-sea water system.

As the sea water acidity goes up, pH goes down, and there are more  $[\text{H}^+]$  ions present than there are  $[\text{OH}^-]$ . One key element which can be gleaned from equation (6-29) is that

the reduced concentration of the hydroxy ion and increased concentration of hydrogen ion due to increased acidity reduces the  $[Ca^{2+}]$  concentration requirement to balance the equation. So as the acidity increases, concentration of  $[Ca^{2+}]$  reduces. In fact, acid treatment, the act of increasing feed water acidity, or acid dosing, as seen in desalination literature, is a widely utilized method to mitigate  $CaCO_3$  crystallization in MSF plants. For the sake of full disclosure, it should be mentioned that real sea water chemical equilibrium is more involved than that captured by equation (6-29). Web-based application FITEQL is a computer program for determination of chemical equilibrium constants from experimental data which can be used for sea water chemical equilibrium. Another commercial program available for chemical equilibrium is MINEQL+ 4.5.

### 6.3.4. Rate of Deposit

The rate of deposit was simply treated as a time invariant quantity in the generalized theory of fouling. Here we will take a closer look at the rate of fouling deposition.

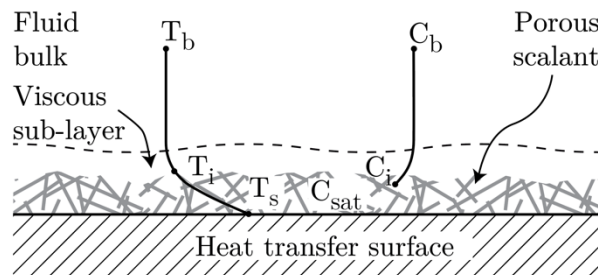


Figure 6-3. Temperature and concentration gradient for an inverse solubility salt in vicinity of a heated surface

As the solution of an inverse soluble salt traverses across a heated surface it gains temperature, and after exceeding the saturation limit some of its salt deposits on the heat transfer layer creating a saturated porous layer of crystallized fouling layer. Heat is

conducted from the hot surface at  $T_s$  through the fouling layer which raises the fluid-foulant<sup>3</sup> interface temperature to  $T_i$ . Neglecting radiation - a reasonable assumption given low working temperatures, low sea water emissivity, and absorptivity - only convection takes place between the interface and the bulk of the fluid raising its temperature to  $T_b$ . The heat of reaction occurring at the interface is neglected. On the other hand, concentration gradient between fluid bulk,  $C_b$ , and interface concentration,  $C_i$ , drives mass diffusion as given by the following:

$$\phi_d = \mathcal{G}_{m1}(C_b - C_i), \quad (6-30)$$

in which  $\phi_d$ , is the mass transfer flux and  $\mathcal{G}_{m1}$  is the mass transfer conductance of species 1 which in this case is  $CaCO_3$ .

The diffused salt at the interface now goes through a chemical reaction to form hard porous fouling layer according to the following equation:

$$\phi_d = k_r(C_i - C_{sat})^n, \quad (6-31)$$

where  $k_r$  is the chemical reaction coefficient, and  $n$  is the order of reaction. Studies done on the order of reaction show that it is a function of the number of participating ions and

---

<sup>3</sup> For the sake of brevity, fluid-foulant interface is referred to as interface hence forth.



is usually taken to be  $n = 2$  for calcium carbonate reaction. [78, 79, 80]. The chemical reaction coefficient is a function of temperature, and can be calculated using the Arrhenius relation

$$k_r = k_{r,0} e^{-Ea/RT_s}, \quad (6-32)$$

for a known preexponent,  $k_{r,0}$ , reaction activation energy,  $Ea$ , universal gas constant,  $R$ , and surface temperature.

Considering equation (6-32) and the considering order of reaction for  $CaCO_3$ , equation (6-31) becomes

$$\phi_d = k_{r,0} e^{-Ea/RT_s} (C_i - C_{sat})^2. \quad (6-33)$$

In order to eliminate the interfacial concentration, equations (6-30) is solved for and inserted into equation (6-33). After some algebra manipulation equation

$$\phi_d = \mathcal{G}_{m1} \left[ \frac{1}{2} \left( \frac{\mathcal{G}_{m1}}{k_r} \right) + C_b - C_{sat} - \sqrt{\frac{1}{4} \left( \frac{\mathcal{G}_{m1}}{k_r} \right)^2 + \left( \frac{\mathcal{G}_{m1}}{k_r} \right) (C_b - C_{sat})} \right] \quad (6-34)$$

emerges. As the reaction rate increases and eventually overcomes mass transfer conductance, the limits of equation (6-34) tending to infinity becomes

$$\lim_{k_r \rightarrow \infty} \phi_d = \mathcal{G}_{m1} (C_b - C_{sat}) \quad (6-35)$$

simply indicating that the reaction is diffusion controlled. However, the same cannot be said when mass transfer conductance tends to infinity as

$$\lim_{g_{m1} \rightarrow \infty} \phi_d = \infty. \quad (6-36)$$

Although equation (6-34) performs well in predicting cases where simultaneous mass transfer and reaction occurs, its capability is inadequate in cases where the rate of deposit is heavily diffusion dependent, such as those in equation (6-36). To alleviate this problem, equation (6-34) is usually complemented with a modification of equation (6-30) in which the interface concentration is assumed to be saturation concentration, i.e:

$$\phi_d = g_{m1} (C_b - C_{sat}). \quad (6-37)$$

Another form of equation (6-34) found in the literature is the one proposed by Epstein 1994 in which fluid residence time is accounted for by a non-dimensional term named friction factor

$$f_f \equiv \frac{\mu_s}{\rho_s v^2}, \quad (6-38)$$

where  $\mu$ ,  $\rho$ ,  $v$  are the fluid dynamic viscosity, density, and bulk velocity respectively.

To paraphrase Epstein's words, within the viscous sublayer, friction factor is inversely proportional to the fluid velocity and directly proportional to the shedding period of that sublayer. Friction factor varies as the fluid residence time near the wall, and it integrates the idea that the longer the fouling material spends at the heat transfer surface, the greater the chances that it will adhere to that surface [81]. Consideration of Epstein's argument transforms equation (6-31) into

$$\phi_d = k'_r(C_i - C_{sat})^2 \frac{\mu_s}{\tau_w}, \quad (6-39)$$

and, consequently, equation (6-34) into

$$\phi_d = \mathcal{G}_{m1} \left[ \frac{1}{2} \left( \frac{\mathcal{G}_{m1} \mu_s}{k'_r \tau_w} \right) + C_b - C_{sat} - \sqrt{\frac{1}{4} \left( \frac{\mathcal{G}_{m1} \mu_s}{k'_r \tau_w} \right)^2 + \left( \frac{\mathcal{G}_{m1} \mu_s}{k'_r \tau_w} \right) (C_b - C_{sat})} \right], \quad (6-40)$$

the mass transfer coefficient is obtained from Sherwood number

$$\mathcal{G}_{m1} \equiv \frac{\text{Sh} \mathcal{D}}{D_h}, \quad (6-41)$$

in which  $\text{Sh}$ ,  $\mathcal{D}$ ,  $D_h$  are Sherwood number, binary diffusion coefficient, and hydraulic diameter accordingly. Sherwood number for a flow inside a smooth tube is found from the analogy drawn between heat and mass transfer as follows

$$\text{Sh}_{D_h} = 0.023 \text{Re}_{D_h}^{0.8} \text{Sc}_s^{0.4}, \quad (6-42)$$

in which  $\text{Sc}_s$  is the solution Schmidt number.  $\text{Re}_{D_h}$  is the hydraulic diameter-based Reynolds number defined as

$$\text{Re}_{D_h} \equiv \frac{\rho_s v D_h}{\mu_s}. \quad (6-43)$$

With the consideration of a smooth pipe the wall shear stress,  $\tau_w$  in equation (6-39), for a given flow rate and fluid viscosity is given by many correlations. One such equation is [Petukhov] correlation: following equation

$$C_f = (0.197 \ln Re_{D_h} - 0.41)^{-2}. \quad (6-44)$$

in which  $C_f$  is the friction coefficient given by:

$$C_f \equiv \frac{\tau_w}{\rho_f v^2 / 2}. \quad (6-45)$$

### 6.3.5. Rate of Removal

As fouling continues, and fluid cross section area reduces, for a fixed flow rate wall shear stress increases. The elevated fluid friction on the fouling surface can in some cases lead to the weakening of scalent and, subsequently, its removal. This mechanism is called removal rate and for crystallization based on the provided argument is directly proportional to wall shear stress, and inversely proportional to foulant strength. Alsaehaie et al. suggest the following equation appropriate to multistage flash desalination:

$$\phi_d = k_{rem} \frac{\tau_w}{\sigma_f} \rho_f (\mu_s g / \rho_s)^{1/3}, \quad (6-46)$$

stating  $k_{rem}$  is the constant of proportionality,  $\rho_f$  is the density of the deposit,  $\rho_s$  is the density of the solution,  $\mu_s$  is the kinematic viscosity of the solution, and  $\sigma_f$  is the foulant shear strength calculated as

$$\sigma_f = K_r \frac{\mathcal{P}}{Nx(1 + \alpha\Delta T)d_p}, \quad (6-47)$$

where  $\mathcal{P}$  is the crystalline adhesion force,  $K_r$  the constant of proportionality,  $N$  is the number of defects in fouling layer,  $\Delta T$  is the temperature drop across the fouling layer,  $\alpha$  is the coefficient of linear thermal expansion, and  $d_p$  is the crystal size [76]. Substituting equation (6-47) into (6-46) yields

$$\phi_d = \frac{k_{rem}N}{K_r\mathcal{P}} x(1 + \alpha\Delta T)d_p\tau_w\rho_f(\mu_s g/\rho_s)^{1/3}. \quad (6-48)$$

For a given heat flux with a known foulant thermal conductivity,  $k_f$ , the temperature difference across the layer is known:

$$\Delta T = \frac{q\mathcal{x}}{k_f}$$

For constant heat flux condition,  $q$  is readily available, and if heat is being supplied through other means, correlations can be used to find local heat flux into the plate/condenser.

As per Kraus's suggestion the first group of parameters in the former equation are inversely proportional to a power of velocity such that:

$$K_{rem}\mathcal{P}/k_rN = 83.2 \times v^{0.54}. \quad [82] \quad (6-49)$$

When combined with equation (6-49), equation (6-48) takes the form of

$$\phi_d = \frac{x(1 + \alpha\Delta T)d_p\tau_w}{83.2 \times v^{0.54}} \rho_f(\mu g/\rho)^{1/3}. \quad (6-50)$$

### 6.3.6. Fouling growth

Expanding the rate of crystallization fouling in terms of density of the foulant times the thickness of the foulant layer, equation (6-1) becomes:

$$\phi = \rho_f \times \frac{d\mathbf{x}}{dt} = \phi_r - \phi_d. \quad (6-51)$$

Inserting equations (6-50) and (6-40) into equation (6-51) we have:

$$\begin{aligned} \rho_f \times \frac{d\mathbf{x}}{dt} = \mathcal{G}_m \left[ \frac{1}{2} \left( \frac{\mathcal{G}_m v^2}{k'_r \mu} \right) + C_b - C_{sat} \right. \\ \left. - \sqrt{\frac{1}{4} + \left( \frac{\mathcal{G}_m v^2}{k'_r \mu} \right)^2 + \left( \frac{\mathcal{G}_m v^2}{k'_r \mu} \right) (C_b - C_{sat})} \right] \\ - \mathbf{x} (1 + \alpha \Delta T) \frac{d_p \tau_f}{83.2 \times v^{0.54}} \rho_f \left( \frac{\mu_s g}{\rho_s} \right)^{\frac{1}{3}}. \end{aligned} \quad (6-52)$$

For a given  $d_p$  and the initial condition of  $\mathbf{x}|_{t=0} = 0$ , and with the assumption of unchanged fluid velocity, mass transfer coefficient, wall shear stress, and temperature drop across the foulant, equation (6-52) can be integrated to yield an expression of foulant layer thickness as a function of time. For ease of integration equation (6-52) can be molded in the form of

$$\frac{d\mathbf{x}}{dt} = a - b\mathbf{x}, \quad (6-53)$$

which when integrated becomes

$$\mathbf{x} = \frac{a}{b} (1 - e^{-bt}) \quad (6-54)$$

in which

$$a = \mathcal{G}_m \left[ \frac{1}{2} \left( \frac{\mathcal{G}_m v^2}{k_r \mu} \right) + C_b - C_{sat} - \sqrt{\frac{1}{4} + \left( \frac{\mathcal{G}_m v^2}{k_r \mu} \right)^2 + \left( \frac{\mathcal{G}_m v^2}{k_r \mu} \right) (C_b - C_{sat})} \right],$$

$$b = (1 + \delta \Delta T) \frac{d_p \tau_f}{83.2 \times v^{0.54}} \rho_f \left( \frac{\mu_w g}{\rho_w} \right)^{\frac{1}{3}}.$$

Equation (6-54) has a steady state value of:

$$\lim_{t \rightarrow \infty} x = \lim_{t \rightarrow \infty} \frac{a}{b} (1 - e^{-bt}) = \frac{a}{b}, \quad (6-55)$$

suggesting that there is a point in which the rate of deposition equals the rate of foulant removal.

At any given bulk temperature and surface temperature the supersaturation for a water system can be calculated. Solution density, and wall shear stress, binary diffusion coefficient, and lastly mass transfer coefficient can be calculated as well. The problem, however, lies in quantifying the preexponent and the activation energy a priori. Many researchers have in fact conducted experiments at different temperature, and fluid velocities to quantify the two unknowns. Pääkkönen et. al performed multiple experiments for a fixed inlet temperature and varying heat fluxes and fluid flow translating into different surface temperatures on saturated  $\text{CaCO}_3$  system. They found that for their set of experiments a regression bases on a Levenberg–Marquardt algorithm has the lowest  $R^2$  and second lowest value when considering negligible diffusion resistance coupled with friction factor, equation (6-40), and not considering friction factor, equation (6-34), accordingly. Fahimian et al. performed a series of experiments to quantify the values of

activation energy for a series of velocity and surface temperature using sensible heating on centi-meter scale tubes [83]. They found that in some cases for fixed inlet surface temperature, and controlled inlet temperature the activation energy increases by 60% when inlet velocity is increased by 40%.

Table 6-3: Values of  $E_a$ ,  $K_0$  used in the literature for  $\text{CaCO}_3$ ,  $\text{CaSO}_4$

Author	$E_a$ [kJ/mol]	$k_{r,0}$	Notes
Pääkkönen [71]	148	$1.62 \times 10^{20}$ [m <sup>4</sup> /kg.s <sup>2</sup> ]	Reaction controlled + friction factor. $\text{CaCO}_3$
	179	$1.65 \times 10^{20}$ [m <sup>4</sup> /kg.s]	Reaction controlled. $\text{CaCO}_3$
Alsaaiem [76]	68	$1.8 \times 10^{10}$ [m <sup>4</sup> /kg.s <sup>2</sup> ]	$\text{CaCO}_3$
Epstein et al. [83]	176		$v_f = 0.44$ m/s $T_w = 98-100$ °C
	1248		$v_f = 0.84$ m/s $T_b = 73-74$ °C $\text{CaSO}_4$

In conclusion, despite all the effort in finding a suitable model to predict crystallization fouling a few unknowns cannot be determined a priori, and as apparent from the literature can heavily depend on fluid velocity, and surface temperature. For this matter, despite the existence of a large body of knowledge on crystallization fouling in microscale, and centimeter-scale there is a gap in knowledge for mini scale condensers. Even for mini-scale heat transfer surfaces, fouling characterization is a vast knowledge base, requiring a detailed experimental and modeling effort. Since the focus of this dissertation is to determine the prospects of compact minichannel condensers for MSF, only a preliminary experimental study of fouling is undertaken.



Absent exact experimental values, the designer is left to make a judgment call based on the gathered information from available literature that may or may not be suitable to the application and conditions at hand. Due to the lack of available reference points intended for minichannel condensers operating under conditions similar to that of multistage flash, a preliminary experimental investigation into fouling was performed.

## **6.4. Experimental Investigation**

### *6.4.1. Procedure:*

A 55-gal (~208L) barrel was cleaned and filled with DI water. The barrel was insulated using R-40 pink insulation and covered with a plastic wrap to protect against accidental liquid spillage. An immersion heater was used to maintain constant reservoir temperature. A twin blade 60cm long mixer rod attached to a lab stirrer was used to agitate the mixture during the entire experimentation period. 200L of DI water was pumped into the reservoir. Using two-part epoxy, the test piece, a mini-channel plate, was mounted into a flange and bolted to a 3-D printed ABS plenum, compressing a custom laser-cut 5mm gasket (Figure 6-4). The plenum had 1/2" npt inlet and outlet ports, as well as 1/8" npt ports for plenum pressure drop.

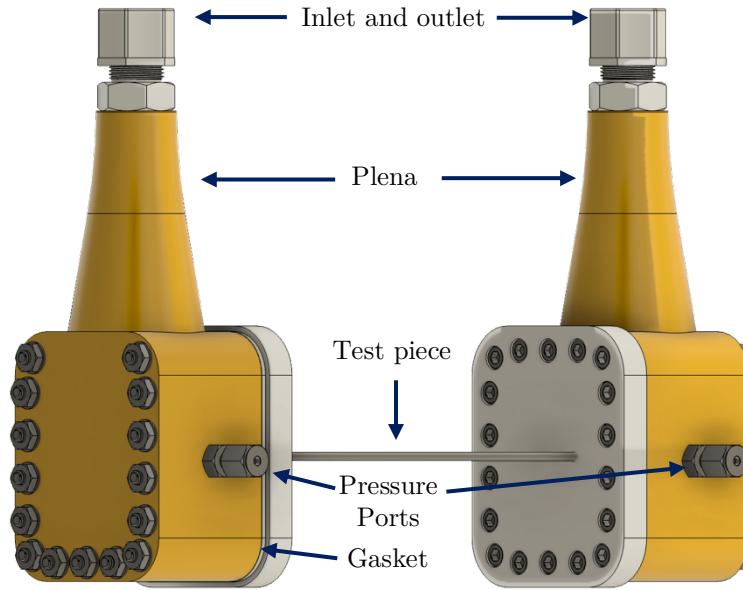


Figure 6-4: Test piece assembly

Two K-type thermocouples (Omega FPD3204-D-A) monitored the inlet and exit fluid temperature connected to the main line via a 1/2" plastic T located 5 cm above fluid inlet and outlet. Four K-type (Omega SA3-T-SRTC) surface mounted thermocouples (SMTC) were utilized to measure plate temperature. Two plate type pressure transducers (Validyne DP15, diaphragm 32, 40) pressure transducers were used to measure pressure drop across plena, one low range (14kPa max), and the other high range (86kPa max). The assembled test piece was placed inside a circulating water bath heater with a fixed temperature set to 68 °C (Figure 6-4). The bath temperature was fixed such that for a determined location of the assembly a temperature gain of 0.3°C across the plena would be achieved. Such determination required running the experiment with DI water at the desired flow rate and adjusting the water bath temperature such that the target goal is reached. Solution salinity was monitored and controlled via a benchtop salinity meter (Thermo Scientific™ Orion Star 212) connected to an Orion two cell conductivity probe.

Two peristaltic pumps were controlled via the salinity meter and actuated using a solid-state relay to dispense 6 g/L, and 4.3 g/L solutions of  $\text{CaCl}_2$ ,  $\text{NaHCO}_3$  from individual containers at an equal rate. A pump (make and model) was used to circulate the solution from the reservoir through the test assembly, back to the reservoir. A positive displacement flow meters (Omega FPD3204-D-A) was used to measure solution flow rate. The pressure transducer, thermocouple, salinity meter, and the flow meter voltage output were connected to a LabVIEW<sup>TM</sup> program for and converted to their corresponding value for real time monitoring. The converted values, peristaltic pump status, and salinity set point were saved for post processing.

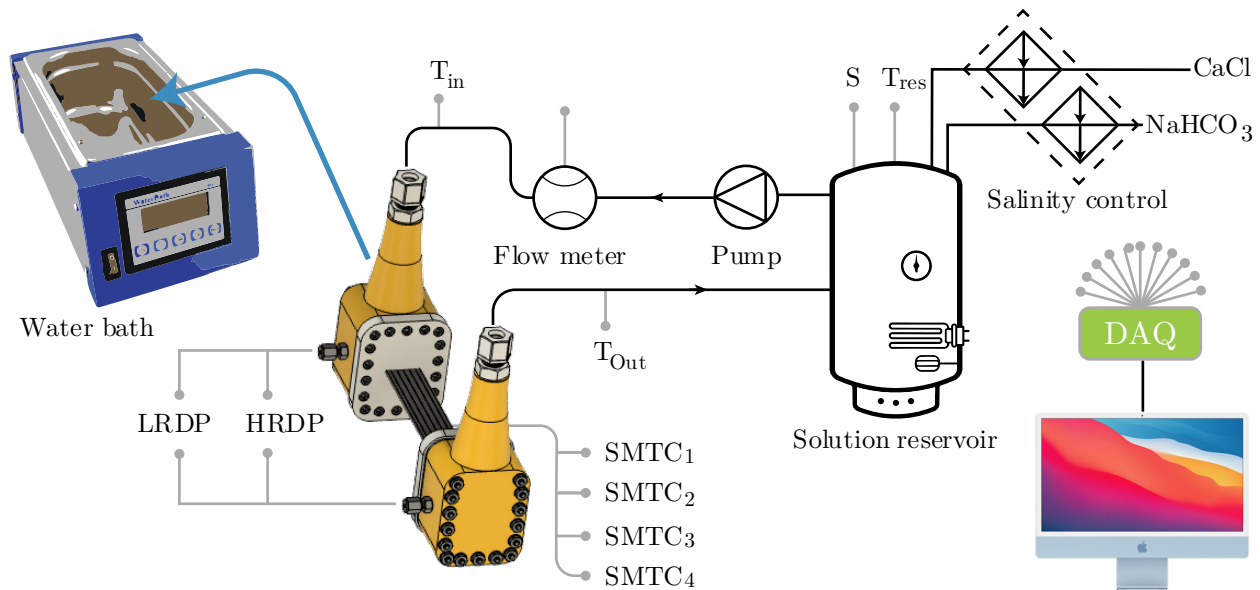


Figure 6-5: Long term salt deposition test assembly schematic

### 6.4.2. Experiment Initiation

200L of DI water was mixed with 100.1170g of 99% pure  $\text{NaHCO}_3$  (CAS# 144-55-8), 71.4353g of 99% pure  $\text{CaCl}_2$  (CAS# 10043-52-4). An initial salinity of 1291  $\mu\text{s}/\text{cm}$  was

achieved, but due to deposition on reservoir heater salinity level quickly decreased. Peristaltic pumps were actuated to increase the salinity level back to the initial level. Reservoir immersion heater was adjusted such that the inlet temperature of 52 °C was achieved. Solution pH was measured to be about 7.1.

### *6.4.3. Daily Startup Procedure*

The water bath was turned on, and the test assembly was removed from the water bath, and its bolts retightened. Due to the applied thermal stresses, despite the use of split lock washers the bolts on the test assembly would loosen up; failure to adhere to the former procedure increased the likelihood of a leak from salt solution to the water bath. The experiment data was saved to a file every 3 seconds (maximum inquiry frequency is 1/3 Hz for the salinity meter). Upon reaching the predetermined set point and achieving SMTC steady state, the loop pump was turned on.

### *6.4.4. Daily Shutdown Procedure*

Data saving process was stopped, and the water bath was turned off. To remove the solution from inside the test piece a line connection from before the pump was disconnected and left open, exposed to the atmosphere. Running the pump in this condition for 30 seconds de-primed the pump and emptied the line of solution replacing it with air. The pump was then stopped, concluding the shutdown procedure.

### *6.4.5. Data Processing*

A MATLAB<sup>TM</sup> code was utilized to combine and plot daily experiment data. Data noise reduction was achieved through a running average algorithm with radius 5 applied 32 times to the data. Data trend was monitored daily for potential inconsistencies.

### *6.4.6. Experiment Results and Discussion*

The long-term salt deposition experiment was carried out for about 38 hours. The experiment was then completely stopped, and the test article was removed from the assembly, and stored for farther examination. The following set of graphs are the results of combined daily data collection. On the vertical axis the data of interest is plotted, and on the horizontal axis total experiment time is presented. A moving average with neighborhood of 5 has been applied forty times to the data. A black dashed vertical line with a day title has been added to the graphs, indicating the end of experimentation for that day. Data collection frequency is every 1/3 Hz for the first two days, and 1/9 Hz for the rest of experiment. Figure 6-6 correspond to pressure drop across plena. Early in the course of experimentation, it was noticed that there is a large difference between the end and start value for pressure drop for two consequent days. Observe the sudden increment in Figure 6-6 at the end of day 1 experiment mark. To increase the confidence in the data collection method, a second low range transducer was added in series to the original pressure transducer. On the start of the sixth day of experiment, inadvertently, the flow pump was set to an rpm corresponding to an average flow rate of 123 g/s instead of the original 111 g/s. This mistake led to higher pressure drop value than expected from

the previous data trend which was corrected for by calculating the corresponding pressure drop for the original flow rate with the plausible assumption of a constant density and friction factor,

$$\Delta P_{111} = \Delta P_{123} \left( \frac{v_{111}}{v_{123}} \right)^2. \quad (6-56)$$

Equation (6-56) was used to find the corrected pressure drop. In this equation in indexes refer to the flow rate, and the corrected value of flow rate was obtained by offsetting the recorded flow rate values  $v_{123}$  such that their mean equals  $v_{111}$ .

$$|v_{123}| - 111 = \text{offset}. \quad (6-57)$$

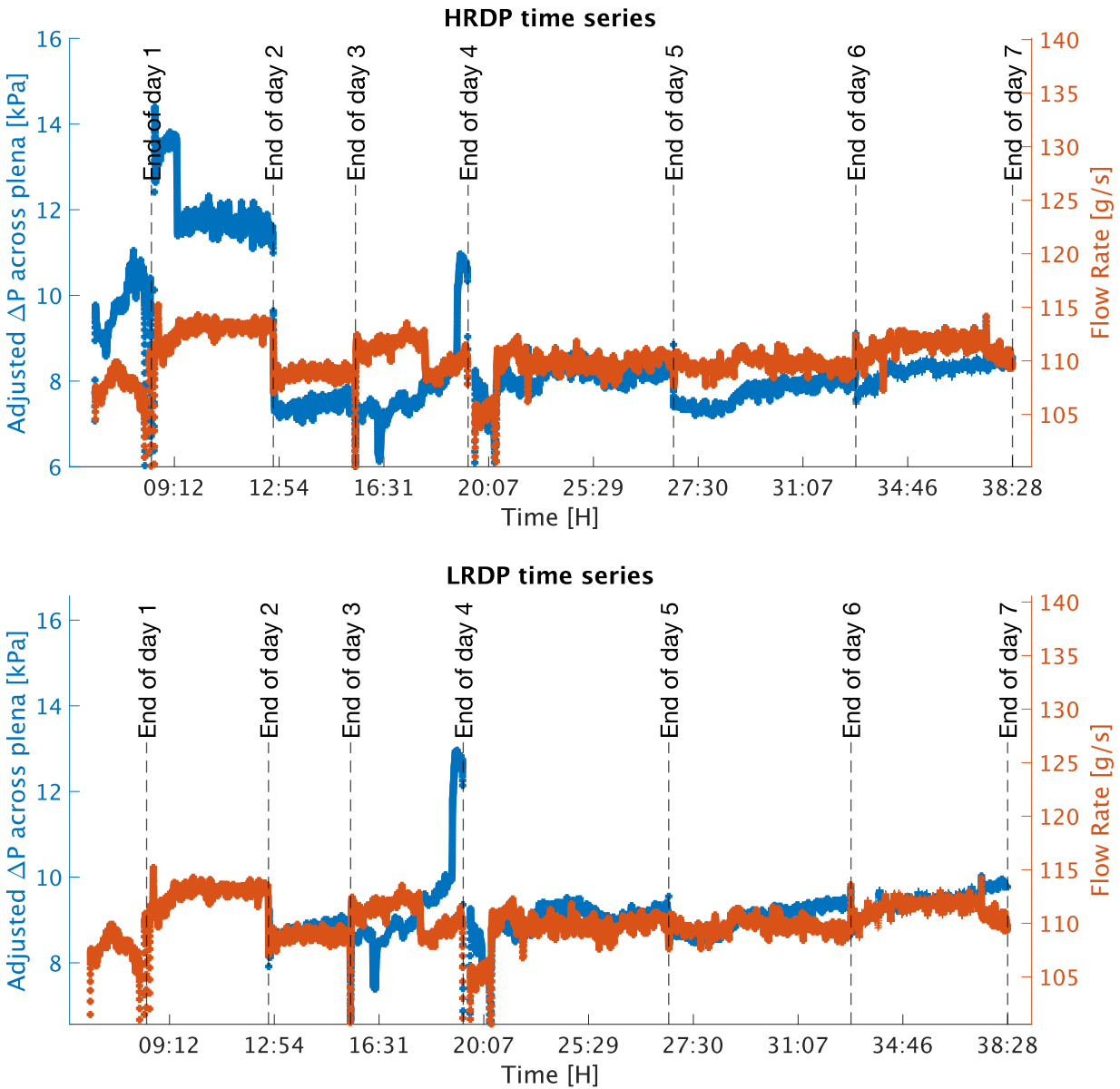


Figure. 6-6: High Range (HRDP) Pressure Drop, top, and Low Range Pressure Drop (LRPD), bottom, time series for the first experiment. The abscissa is cumulative operating time.

Overall, despite a few data fluctuation in between experiment days, pressure drop values are steady suggesting that little or no scale-build-up induced cross section reduction.

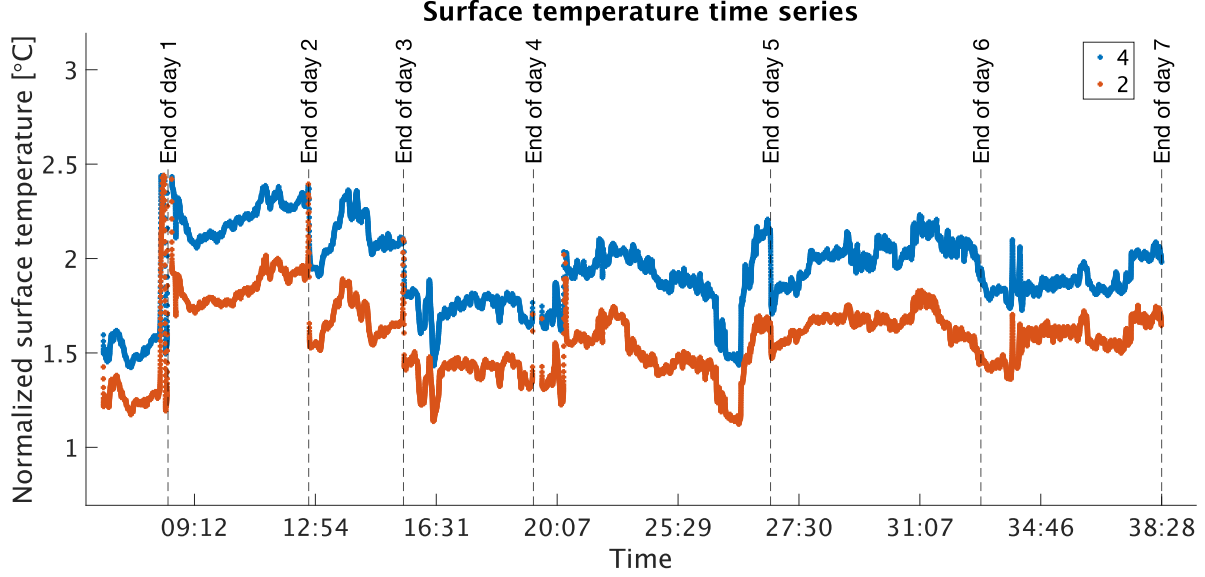


Figure 6-7: Normalized surface temperature time series for the first experiment. Normalization was achieved by subtracting surface temperature from inlet temperature. SMTC<sub>2</sub> is the closest and SMTC<sub>4</sub> is the furthest from the inlet. The abscissa is cumulative operating time.

Despite heavy insulation of both the reservoir, and the inlet lines the rigid duty cycle of the reservoir immersion heater prohibited tight inlet temperature control ( $T_{in} - |T_{in}| = \pm 0.6$  °C/h). To account for the variation in the inlet temperature, the values of SMTC were normalized by subtraction from inlet temperature for the same time stamp. Same time stamp data can be used because given the short distance between the inlet thermocouple and any of the SMTC it is unlikely that the temperature values at any given time,  $t$ , would be different than their  $\Delta t$  seconds later, i.e:

$$\text{SMTC}_n(t) = \text{SMTC}_n(t + \Delta t),$$

$$T_{in}(t) = T_{in}(t + \Delta t),$$

$$\text{SMTC}_n(t + \Delta t) - T_{in}(t) = \text{SMTC}_n(t + \Delta t) - T_{in}(t + \Delta t).$$



Initially, four SMTC were utilized, but soon after the first day of experimentation SMTC<sub>1</sub> detached from the surface while immersed in bath water. SMTC<sub>3</sub> followed suit on the third day. Although restoration efforts were made, they either failed completely for SMTC<sub>1</sub>, or short-lived for SMTC<sub>3</sub>. Figure 6-7 is a depiction of the normalized SMTC values.

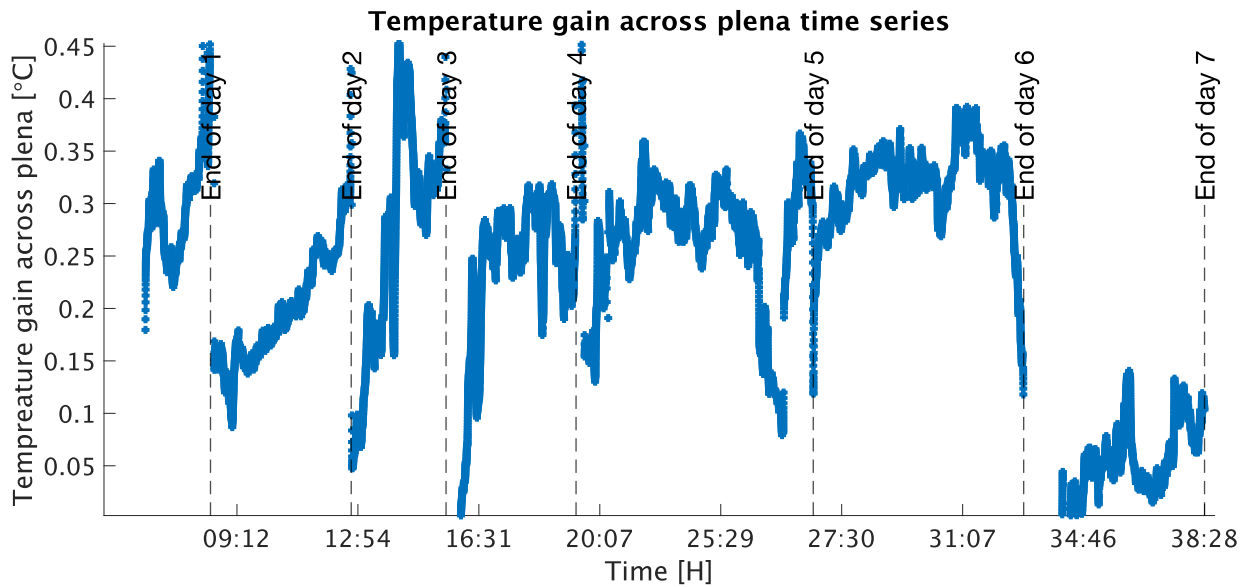


Figure 6-8: Temperature gain across plena time series for the first experiment. The abscissa is cumulative operating time

Figure 6-8 depicts the temperature gain across the plena. In the initial stages of the experiment, it was found that the location of the test assembly inside the water bath has a large effect on the temperature gain across the plena. For repeatability, the location of the test assembly inside the water bath was marked on the second day, and the future experiments started from the marked location. Although the same cannot be said about the first 3 days of experiment, during days 4-6 the desired 0.3 °C was tightly maintained. On the 7<sup>th</sup> day, the value of temperature gain was different than any other day throughout the experiment. This anomaly was traced to a fault in outlet temperature thermocouple.

As evident from Figure 6-7, day 7 data, heat transfer between the hot bath fluid and the salt solution occurred at least up to the point where SMTC<sub>4</sub> is mounted, but the faulty thermocouple could not capture the increase in fluid temperature accurately. Comparing the last days of experiment on Figures 6-7, and 6-8 it can be concluded that the temperature gain across plena would follow the previous daily trend. Temperature gain seem to have reached a steady state value after the second day.

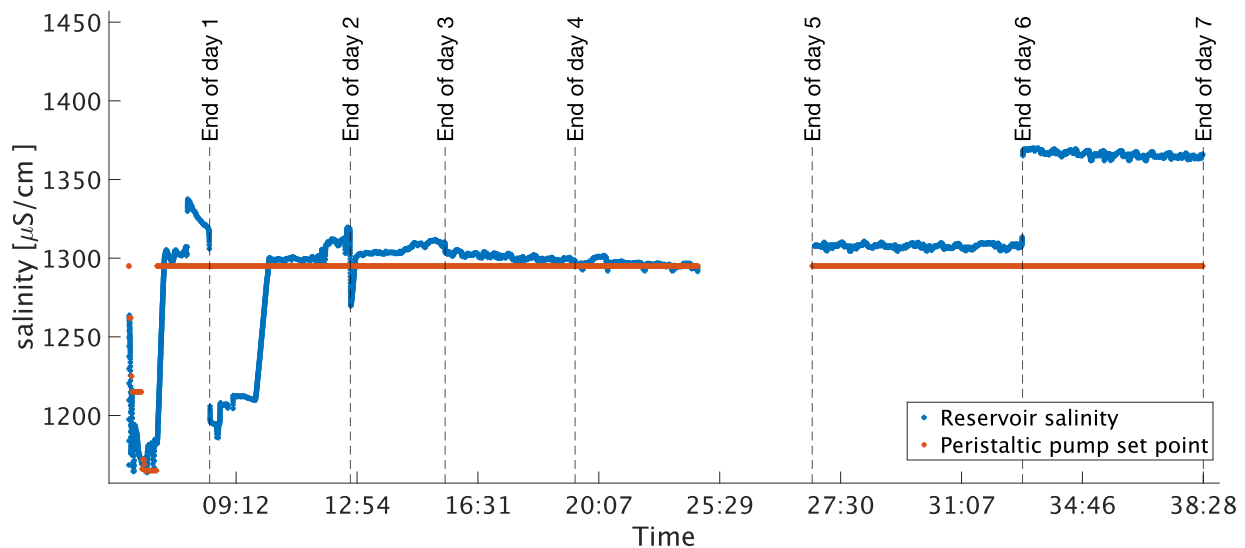


Figure 6-9: Reservoir salinity time series as well as the peristaltic pump set point. Data for last portion of the 5<sup>th</sup> day was not recorded. Data has been cleaned up to remove the effect of moving average applied to data adjacent to zero values.

Figure 6-9 indicates the reservoir salinity level throughout the experiment. Data is presented from the time reservoir is initially introduced to the salts. There is an initial steep decline in salinity level which is believed to be due to calcium depositing on the immersion heater surface. To battle this, the peristaltic pumps were turned on until the salinity level reached back to the original post mixing value of 1291  $\mu\text{S}/\text{cm}$ . At the end portion of the first day of the experiment the level of salinity was increased 50 units. This

increment was done to understand the sensitivity of experiment to increased salinity level. No direct effect was observed. A large decline is observed between the end of the first and start of the second day of experiment. This large drop is also believed to be related to prolonged immersion heater surface deposition. On the second day, the reduced salinity level opened the doors to test the experiment sensitivity to lower salinity levels. The effect of 50 units reduction in salinity was later determined to be non-existing. After about halfway through the second day of experiment, more salt solution was added to the reservoir increasing the salinity to the post mix value. At the last portion of the second day, due to a fault in the control system the pumps continued to dispense salt solution beyond the set point. Without any salt addition, the reservoir reached equilibrium during the between day 2 end point and day 3 start point. A steady gradual decline in salinity level is observed between days 3-5, followed by an absence in salinity values for the last portion of the 5<sup>th</sup> day. Salinity jumps of 20, and 60  $\mu\text{s}/\text{cm}$  are observed at the beginning of the 6<sup>th</sup> and 7<sup>th</sup> day respectively. In the interest of time, the reservoir heater was left on during hour of inactivity which led to minor evaporation of reservoir liquid and consequent salinity increase in between experiment days. There is a single-day time difference between the 5<sup>th</sup> and 6<sup>th</sup> day of experiment, whereas this time difference is 3 days between the 6<sup>th</sup> and the 7<sup>th</sup> day of experiment. Should the rate of natural evaporation be considered equal, and the amount of liquid evaporated assumed small in comparison to the total reservoir liquid, the three times as much delay explains the three times as much salinity increase.

## 6.5. Chapter Conclusion

In this chapter a background of fouling, was given. It was established that crystallization fouling is one of the most dominant forms of fouling and hence it was chosen as focus of this chapter. Crystallization fouling theory was discussed. Additionally, it was realized that crystallization fouling is highly application and geometry specific. Neither available design values nor models pertaining to MSF and the proposed compact condenser exist. Due to this lack of appropriate models capable of providing accurate trans-scale predictions, and in pursuit of satisfying objective 5, a preliminary experiment designed to outline the long-term effects of  $\text{CaCO}_3$  deposition in MSF desalination application was devised.

The experiment tightly controlled the temperature gain across condenser plate, reservoir salinity, and the flow rate. Considering the steady daily value for pressure transducers, and steady surface temperature measurements, there is no evidence to suggest that a solution made with the recipe described in this work will precipitate on the inside of the condenser plate when operated at the maximum temperature of  $60\text{ }^\circ\text{C}$  gaining  $0.3\text{ }^\circ\text{C}$  running at internal velocity of  $110\text{ [g/s]}$  at least within the time frame of 38 hours.



## Chapter 7: Conclusions and Future Work



## 7.1. Conclusions

In Chapter 1, of this dissertation, a brief history of desalination was presented. Two principal desalination modes, thermal desalination, and separation desalination were introduced, and contrasted. In-depth details of multistage flash (MSF) desalination were presented, and it was established that due to its reliable history, and proven track record, multi-stage flash will continue to be one of the main thermal desalination methods for the foreseeable future.

In Chapter 2, related technical and financial background information on a particular MSF pas was provided. A correlation model for an MSF condenser was formulated in which dominant heat transfer modes were understood and outlined. Considering design bottlenecks, as identified by the model, a compact condenser comprised of multiport minichannel plates was proposed.

In Chapter 3, the effect of plate spacing on co-current condensation was considered. It was found that while condensation flux either stayed the same or reduce, in the case of 1 mm plate spacing as much as 90%, co-current condensation enhances condensation by 5% under geometry, and conditions similar to the proposed compact multiport condenser. It was further argued that the positive effects of co-current condensation would balance out the adverse effects of the counter-current condensation, and hence Nusselt falling film model is a practical option for modeling purposes.

In Chapter 4 using the developed model a parametric study including variations in condenser geometry, fouling factor, as well as modes of condensation was performed on the proposed compact condenser. The parametric study led to the conclusion that under identical operating conditions, maintaining same performance requirements, and requiring the same electrical and thermal energy, the condenser size of the studied MSF desalination plant can be reduced by a factor of 10. This size reduction is achieved by 1) enhancement of the overall heat transfer coefficient achieved by the combination of employing smaller internal flow passages and dropwise condensation, and 2) by tighter plate packing. Together the two factors contributed to an estimated overall capital investment reduction of 22.9% made available due to direct material cost reduction. Additionally, the model was utilized to understand the prospects of a compact condenser made with composite material. It was found that although polymers are potential candidates as far as having favorable condensation surfaces, their thermal conductivity needs to be improved by at least a factor of 3 to replace the studied baseline MSF condenser. Furthermore, it was established that knowledge of accurate fouling factor accurate for the proposed multiport condenser is imperative.

In Chapter 5, the underlying model leading to the predicted performance improvements of the multiport minichannel condenser was validated under different flow rates and MSF-matched subcooling conditions. Three different condenser configurations comprised of the previously introduced multiport plates with and without dropwise promoter (total 5 test articles) were tested. A sub atmospheric pressure chamber was fabricated to test the

condenser configurations. Model predictions for the single plate and sparsely spaced 5-plate are within 10% margin of error, while the tightly packed condenser underperforms model prediction by up to 35%. The dropwise promoter in some cases increases heat flux of condensation by 65%. It was found that plate gap has a critical role in condenser performance, so much so that the tightly packed condenser had an overall heat transfer coefficient 20% lower than that of the sparsely packed condenser for the highest tested flow rates. This reduction in performance was resolved when the underperforming condenser was coated with the dropwise promoter, suggesting that dropwise condensation can combat condenser reduced performance caused by tight packing. The results validate the analytical model created in chapter 2. This salient finding indicates that should a condenser be made as described in the concluding section of Chapter 3, it will most likely lead to a capital cost savings similar to predicted compared to a conventional condenser.

In Chapter 6, crystallization fouling, a principal challenge in small scale heat exchangers, was investigated. Modeling of crystallization fouling was extensively reviewed with the conclusion that crystallization fouling, among other factors, is highly size dependent and a complete model capable of making predictions pertaining to the compact condenser evaluated is missing. Additionally, neither experimental values nor design suggestions corresponding to the compact condenser were found in the literature. For these reasons, a preliminary experiment was performed on a condenser with similar geometry as the ones studied in this work. The experiment was conducted using a supersaturated  $\text{CaCl}_2$  salt solution flowing at 110 g/s with an inlet temperature of 60 °C and gaining 0.3 °C across



the condenser. Over the 38 hour duration of the experiment, no crystallization fouling occurred on the inside of the condenser, although longer operating times would be needed to fully assess the fouling potential on these types of heat exchangers.

## 7.2. Future Work

In Chapter 4 the possibility of a compact polymer condenser on which dropwise condensation naturally occur was discussed. It was outlined that for such a condenser to work it would need to have 300  $\mu\text{m}$  thick walls and have a thermal conductivity of 1.6  $\text{W/m} - \text{K}$  which is 3 times as high as the highest thermally conductive plastic in the market. Composite material made from polymer-metal or carbon-fiber composites can be a promising solution, combining the natural dropwise condensation observed on plastics with the higher thermal conductivity of metals are known for. Additionally, the thin walls need to be able to withstand the design fluid pressures.

In this work only a preliminary crystallization fouling experiment was conducted on  $\text{CaCO}_3$  at 60  $^\circ\text{C}$ . Higher temperature, those exceeding 120  $^\circ\text{C}$ , experiments should be done on  $\text{CaCO}_3$  and other dominant inversely soluble salts such  $\text{Li}_2\text{SO}_4$ , and  $\text{NaOH}$  given that the success or failure of the proposed compact heat exchanger design strongly depends on the fouling characteristics. Fouling experiments are the beginning steps in adopting compact condensers. In the event that fouling is a large hindering factor, fouling mitigation techniques tailored to the proposed compact condensers will need to be developed or assessed. Comprehensive studies on fouling at higher temperatures with inversely soluble salt as well as subsequent fouling mitigation techniques as highlighted by the fouling experiments specific to minichannel condensers are needed.

# Chapter 8: Extra

## S

### 8.1. Nomenclature

#### 8.1.1. English

$A$	Area	[m <sup>2</sup> ]	$k_{r,0}$	Chemical reaction coefficient	[m <sup>4</sup> /kg - s], or [m <sup>4</sup> / kg - s <sup>2</sup> ]
$b$	Plate length	[m]	$k_r$	Proportionality constant	
BTM	Bottom Brine Temperature	[°C]	$K_{sp}$	Solubility product	
$C$	Concentration	[kg/m <sup>3</sup> ]	$K_1$	First disassociation constant for $H_2CO_3$	
$C_f$	Coefficient of skin friction		$K_2$	Second disassociation constant for $H_2CO_3$	
$C_p$	Specific heat at constant pressure		$K_2$	Constant of proportionality	[s]
$\dot{c}$	Condensation rate in each control volume	[kg/m <sup>2</sup> - s]	$K_w$	Disassociation constant for water	
$D$	Diameter	[m]	$L_c$	Adiabatic tip Length	[m]
$D$	Binary diffusion coefficient	[m <sup>2</sup> /s]	MSF	Multistage Flash	
$Ea$	Activation energy	[kJ/mol]	MAE	Mean Absolute Error	
$g$	Gravitational constant	[m/s <sup>2</sup> ]	$m$	Chamber vapor mass, mass flux, Pin	[kg], [kg/s]
$g$	Mass conductance coefficient	[m/s]		characteristic number	
$h_{fg}$	Latent heat of evaporation	[J/kg]	$\dot{m}$	Mass flow rate	[kg/s]
$h$	Coefficient of convective heat transfer	[W/m <sup>2</sup> -K]	$n$	Order of reaction, number	
$H$	Henry Constant for $CO_2$ , Condenser plate height, Condenser bundle height	[Pa - m <sup>3</sup> /kg], [m], [m]	$N$	Number of defects in fouling layer, number of stages, number of control volumes	
$i$	Index		$Nu$	Nusselt Number	
Ja	Jacob Number		$Pr$	Prandtl Number	
$k$	Conductivity	[w/m - k]	$\mathcal{P}$	Crystalline adhesion force	[N]
			$P$	Perimeter, Pressure	[m], [Pa]
			$q$	Heat transfer, heat flux	[w], [w/m <sup>2</sup> ]
			$R$	Heat transfer resistance	[m <sup>2</sup> -K/W]
			RMS	Root Mean Square	
			RO	Reverse Osmosis	
			RTD	Resistance Temperature Detector	
			Re	Reynold number	
			$R''_f$	Fouling factor	[m <sup>2</sup> - K/W]
			$R$	Gas constant	[J/K]
			$S$	Salinity	[g/kg <sub>H<sub>2</sub>O</sub> ]
			$t$	Time	[s]
			$T, \bar{T}$	Temperature, Average Temperature	[°C] or [K]

TBT	Top Brine Temperature	[°C] or [K]
BBT	Bottom Brine Temperature	[°C] or [K]
TD	Thermal Desalination	
$th$	Condenser wall thickness	[m]
$u$	Horizontal velocity	[m/s]
$v$	Vertical velocity	[m/s]
$V$	Vapor velocity between two plates, chamber volume	[m/s], [m <sup>3</sup> ]
$W$	Condenser bundle width	[m]
$x$	Foulant thickness	[m]
$Y$	Number of vertical plates	
$z$	Charge number	

### 8.1.2. Greek

$\alpha$	Coefficient of linear thermal expansion	[K]
$\Delta$	Difference	
$\rho$	Density	[kg/m <sup>3</sup> ]
$\sigma$	Shear strength	[Pa]
$\eta_0$	Overall efficiency	
$\Gamma$	Mass flow rate per unit plate length, Perimeter ratio	[kg/m <sup>3</sup> ], []
$\delta$	Boundary layer thickness	[m]
$\eta$	Efficiency	
$\Lambda$	Length ratio	
$\mu$	Dynamic viscosity	[Pa.s]
$N$	Packing density ratio	
$\Pi$	Pressure drop ratio	
$\tau, \tau_0$	Shear stress, Interfacial shear stress	[Pa]
$\phi$	Foulant mass flux	kg/m <sup>2</sup> .s]
$\Omega$	Overall conductance ratio	

### 8.1.3. Sub-and Superscript

$0$	Overall
$b$	Brine
$c$	Cross section
$c$	Channel
$Cond$	Conductive
$Conv$	Convective
$dc$	Dropwise condensation
$f$	Fluid, fouling
$fin$	Fin
$fouling$	fouling
$h$	Hydraulic
$hyd$	Hydraulic diameter
$i$	inlet
$m$	minichannel
$o$	Out
$Phx$	Phase change
$s$	Surface
$sat$	Saturation
$Tot$	Total
$w$	Water
$wall$	Wall
$1$	Species 1
$aq$	Aqueous
$b$	bulk
$d$	Deposit
$f$	Foulant
$g$	Gas
$h$	Hydraulic
$r, rem$	Removal
$Sat$	Saturation
$S$	Surface, solution
$w$	Wall

## 8.2. References

- [1] R. J. Robes, Short History of the Art of Distillation: from the Beginnings Up to the Death of Cellier Blumenthal, Ams Pr Inc; First Edition, 1948.
- [2] "Facts and Statistics about Water and Its Effects," [Online]. Available: [https://thewaterproject.org/water-scarcity/water\\_stats](https://thewaterproject.org/water-scarcity/water_stats). [Accessed Sep 2016].
- [3] N. Ghaffour, "The challenge of capacity-building strategies and perspectives for desalination for sustainable water use in MENA," *Desalination Water Treat*, pp. 48-53, 2009.
- [4] "Desalination Data," [Online]. Available: <http://pacinst.org/publication/key-issues-in-seawater-desalination-proposed-facilities>. [Accessed Sep 2014].
- [5] "Association of California Water Agencies," [Online]. Available: <http://www.acwa.com/content/drought>. [Accessed Sep 2016].
- [6] G. Cismowski, W. Cooley, L. Martin, J. McCarthy, M. Schnagl and A. Toto, "Salinity in the Central Valley- An Overview, Regional Water Quality Control Board, Central Valley Region, California Environmental Protection Agency," [Online]. Available: <http://ponce.sdsu.edu/swrcb-02may06-ovrvw-rpt.pdf>.
- [7] V. Belessiotis, S. Kalogirou and E. Delyannis, "Thermal Solar Desalination: Methods and Systems," Elsevier, p. 84.
- [8] "The World's Saltiest Bodies Of Water," [Online]. Available: <https://www.worldatlas.com/articles/the-world-s-most-saline-bodies-of-water.html>. [Accessed 11 4 2022].
- [9] M. Elimelech and W. Pillip, "The future of sea water desalination: energy, technology, and the environment," pp. 717-717, 2011.
- [10] J. Thompson, A. Rahardianto, H. Gu, M. Uchymiak, A. Bartman, M. Hedrick, D. Lara, J. Copper, J. Faria, P. Christofides and Y. Cohen, "Rapid field assessment of RO desalination of brackish agricultural drainage water," *Water Res*, pp. 2649-2660.
- [11] H. El-Dessouky and H. Ettouney, Fundamentals of Salt Water Desalination, Elsevier Science, 2002.
- [12] M. I. Yusoff, L. W. Zhe, M. Irwanto, A. .M, S. Hassan, S. Ibrahim and A. Amelia, "Comparison of solar panel cooling system by using dc brushless fan and dc water," *Physics*, 2014.
- [13] S. Zubeer, H. Mohammed and M. Illkan, " review of photovoltaic cells cooling techniques," *E3s Web of Conferences*, 2017.
- [14] "Water FX," [Online]. Available: [waterfx.com](http://waterfx.com). [Accessed sep 2016].

- [15] "US Department of Energy Office of Energy Efficiency and Renewable Energy," [Online]. Available: <https://www.energy.gov/eere/solar/funding-opportunity-announcement-solar-desalination>.
- [16] N. Ghaffour, T. Missimer and G. Amy, "Technical review and evaluation of the economics of water desalination: Current and future challenges for better water supply sustainability," *Desakubatuib*, pp. 197-207, 2013.
- [17] V. Narayanan, J. Liburdy and D. Pence, "Encyclopedia of Aerospace Engineering, eds R. Blockley and W. Shyy, John Wiley," in *Thermal Applications of Microchannel Flows*, Chichester.
- [18] N. Kockmann, *Transport Phenomena in MicroProcess Engineering*, Springer Publishing Group.
- [19] B. Tuckerman and R. Pease, "High- Performance Heat Sinking for VLSI," *IEEE Electron Devices Letters*, pp. 126-129, 1981.
- [20] J. Brander, T. Henning, U. Schygulla and K. Schubert, "Microstructure Heat Exchanger Applications in Laboratory and Industry", *Heat Transfer Engineering*, vol. 28, pp. 761-771, 2011.
- [21] S. Karagiannidis and J. Mantzaras, "Numerical investigation on the start-up of methane-fueled catalytic microreactors," *Combust. Flame*, vol. 157, pp. 1400-1413, 2010.
- [22] A. Tonkovich, S. Perry, Y. Wang, Y. Qui, T. LaPlante and W. Rogers, "Microchannel process technology for compact methane steam reforming," *Chemical Engineering Science*, vol. 59, pp. 4819-4824, 2004.
- [23] J. W. Rose and E. J. Le Fevre, "A Theory of Heat Transfer by Dropwise Condensation," *International Heat Transfer Conference*, vol. 2, pp. 362-375, 1966.
- [24] A. Umur and P. Griffith, "Mechanism of dropwise condensation," *ASME J Heat Transfer*, vol. 87, pp. 275-282, 1965.
- [25] M. Ali El Saei, M. Kamel and M. El Kafrawi, "Study of the Operating Conditions for Three Large MSF Desalination Units Each of Capacity 7.2/8.6 MSD in Abu Dhabi, UAE," *Desalination*, vol. 73, pp. 207-230, 1989.
- [26] A. Hassan Khan, *Desalination and Water Purification - Desalination Processes and Multistage Flash Distillation Practice*, Amsterdam: Elsevier, 1986.
- [27] F. Incropera, D. Dewitt, T. Dergman and A. Lavine, *Fundamentals of Heat and Mass Transfer*, Wiley, 2011.
- [28] W. Nusselt, "Die Oberflächenkondensation des Wasserdampfes," *Zeitschrift des Vereines Deutscher Ingenieure*, vol. 60, pp. 541-575, 1916.
- [29] W. M. Rohsenow, "Heat Transfer and Temperature Distribution in Laminar Film Condensation," *Trans ASME*, vol. 78, pp. 1654-1648, 1956.
- [30] E. Sparrow and J. Gregg, "A boundary-layer treatment of laminar film condensation," *J. Heat Transfer*, vol. 81, pp. 13-23, 1959.

- [31] E. Schmidt, W. Schurig and W. Sellschopp, "Versuche über die Kondensation von Wasserdampf in Film- und Tropfenform," *Tech. Mech. Thermodyn*, vol. 1, pp. 53-63, 1930.
- [32] J. W. Rose, "Dropwise condensation theory and experiment: a review," *Institution of Mechanical Engineers*, 2002.
- [33] T. Young, "An Essay on the Cohesion of Fluids," *Philos. Trans R. Soc. London*, pp. 65-87, 1805.
- [34] R. Wenzel, "Resistance of Solid Surface To wetting by Water," *InD. Eng. Chem*, vol. 28, pp. 988-994, 1936.
- [35] A. Cassie and S. Baxter, "Wettability of Porous Surfaces," *Trans. Faraday Soc*, vol. 40, pp. 546-551, 1944.
- [36] R. J. Johnson and R. Dettre, "Contact angle Hysteresis. III. Study of an idealized hetrogenous surface," *J. Phys. Chem*, vol. 68, pp. 1744-1750, 1964.
- [37] V. V. Yaminsky, "Molecular mechanisms of hydrophobic transitions," *J. Adhes. Sci. Technol*, vol. 14, no. 187-233, 2000.
- [38] R. Enright, N. Miljkovic, J. L. Alvarado, K. Kim and J. W. Rose, "Dropwise condensation on micro-and nanostructured surfaces, Nanoscale Microscale," *Thermophys. Eng*, vol. 18, pp. 223-250, 2014.
- [39] S. Vemur, K. J. Kim, B. D. Wood, S. Govindaraju and T. W. Bell, "Long Term Testing For Dropwise Condensation Using Self-Assembled Monolayer Coatings Of N-Octadecyl Mercaptan," *Appl. Therm. Eng*, vol. 26, no. 421-429, 2006.
- [40] J. Zhang B, J. Park, K. J. Kim and H. Yoon, "Biologically inspired tunable hydrophilic/hydrophobic surfaces: a copper oxide self-assembly multitier approach," *Bioinspiration and Biomimetics*, vol. 7, no. 3, 2012.
- [41] S. Lee, K. Cheng, V. Palmre, M. M. H. Bhuiya, K. J. Kim, B. J. Zhang and H. Yoon, "ransfer measurement during dropwise condensation using micro/nano-scale porous surface," *Int. J. Heat Mass Transf*, vol. 65, pp. 619-626, 2013.
- [42] B. J. Zhang, C. Kuok, K. J. Kim, T. Hwang and H. Yoon, "Dropwise steam condensation on various hydrophobic surfaces: Polyphenylene sulfide (PPS), polytetrafluoroethylene (PTFE), and self-assembled micro/nano silver (SAMS)," *Int. J. Heat Mass Transf. 89*, pp. 353-358, 2015.
- [43] G. Azimi, R. Dhiman, H.-M. Kwon, A. Paxson and K. Varanasi, "Hydrophobicity of rare-earth oxide ceramics," *Nat. mater*, vol. 12, pp. 315-320, 2013.
- [44] D. J. Huang and T. S. Leu, "Fabrication of high wettability gradient on copper substrate," *Appl. Surf. Sc*, vol. 280, pp. 25-32, 2013.
- [45] C. Lee and D. Kim, "Fabrication of patterned surfaces that exhibit variable wettability," *Appl. Surf. Sci.*, vol. 288, pp. 619-624, 2014.
- [46] V. P. Carey, *Liquid-Vapor Phase Change Phenomenon*, New York: Taylor and Francis, 2008.
- [47] P. Birbarah and N. Miljkovic, "External Convective Jumping-Droplet Condensation on Flat Plate," *Int. J. Heat and Mass*, vol. 107, pp. 74-88, 2017.

- [48] S. Anand, T. A. Paxon, R. Dhiman, D. Smith and K. K. Varanasi, "Enhanced Condensation on Lubricant-Impregnated Nanotextured Surfaces," *ACS*, vol. 6, no. 11, pp. 10122-10129, 2012.
- [49] C. Graham and P. Griffith, "Drop size distribution and heat transfer in dropwise condensation," *Int. J. Heat and Mass Transfer*, vol. 16, pp. 337-346, 1973.
- [50] J. R. Maa, "Drop size-distribution and heat flux of dropwise condensation," *Chemical Engineers J*, vol. 16, pp. 81-87, 1978.
- [51] M. Abu-Orabi, "Modeling of heat transfer in dropwise condensation," *Int. J. Heat and Mass Transfer*, vol. 1998, 41.
- [52] I. Tanasawa and J. Ochiai, "Experimental study on heat transfer during dropwise condensation," *Bull. Jap. Soc. Mech. Engrs*, vol. 16, p. 1184-1197, 1973.
- [53] C. Graham, "The limiting heat transfer mechanisms of dropwise condensation. PhD thesis," Massachusetts Institute of Technology, 1969.
- [54] I. R. Glicksman and A. W. Hunt, "Numerical simulation of dropwise condensation," *Int. J. Heat Mass Transfer*, vol. 15, p. 2251-2269, 1972.
- [55] T. Murase, H. S. Wang and J. Rose, "Effect of inundation for condensation of steam on smooth and enhanced condenser tubes," *International Journal of Heat and Mass Transfer*, vol. 49, pp. 3180-3189, 2006.
- [56] "Facts and Statistics about Water and Its Effects," 2016. [Online]. Available: [https://thewaterproject.org/water-scarcity/water stats](https://thewaterproject.org/water-scarcity/water-stats).
- [57] W. Rohsenow, J. Webber and T. Ling, "Effect of Vapor on Laminar and Turbulent-Film Condensation," *Trans ASME*, vol. 78, pp. 1637-1643, 1956.
- [58] E. F. Carpenter and A. P. Colburn, "The Effect of Vapor Velocity on Condensation Inside Tubes," *General Discussion on Heat Transfer*, 1951.
- [59] G. Nellis and S. Klein, *Heat Transfer*, New York: Cambridge Press, 2012.
- [60] S. Kline and F. McClintock, "Describing Uncertainties in Single-Sample Experiments," *Physics*, p. 1953, 1953.
- [61] T. Bott, *Fouling of Heat Exchangers*, Birmingham: University of Birmingham, 1995.
- [62] Van Nostrand, S. H. Leach and J. L. Haluska, *Fouling of Heat Transfer Equipment*, Washington: Mesiphere Publishing Corp, 1981.
- [63] P. A. Thakery, "The cost of Fouling in Heat exchanger plants, in," *Corrosion Science and Technology and Instr. Chem Engineerins*, 1979.
- [64] H. U. Zettler, "Heat Exchanger Fouling and Cleaning XIII – 2019," 7 6 2019. [Online]. Available: <https://heatexchanger-fouling.com/refereed-proceedings/heat-exchanger-fouling-and-cleaning-xiii-2019/>. [Accessed 19 5 2022].
- [65] S. Kakaç and H. Liu, *Heat Exchanger - Selection, Rating and Thermal Design*, CRC Press, 1998.
- [66] W. M. Rohsenow, J. P. Hartnett and Y. I. Cho, *Handbook of Heat Transfer*, McGraw-Hill, 1998.



- [67] J. Barbee, M. Davis, S. Davis, D. Gaddis, J. Harrison, M. Holtz, R. McElroy, J. Polizzi and J. Willett, Standards Of The Tubular Exchanger Manufacturers Association, New York: Tema, 2007.
- [68] M. G. Mwaba, M. R. Golriz and J. Gu, "A semi-empirical correlation for crystallization fouling on heat exchanger surface," *Applied Thermal Engineering*, p. 26, 2006.
- [69] R. Ritter, "Crystalline Fouling Studies," *Journal of Heat transfer*, vol. 105(2), pp. 374-378, May 1983.
- [70] J. Bucko, M. Mayer, W. Benzinge, W. Augustin, R. Dittmeyer and S. Scholl, "Influence Of Deposits By Crystallization Fouling In Microchannels On The Heat Transfer Performance Of Micro Heat Exchangers," *International Conference on Nanochannels, Microchannels, and Minichannels*, 2011.
- [71] T. Pääkkönen, C. Riihimäk, E. Simsonson, E. EMuurinen and R. Keiski, "A modeling of CaCO<sub>3</sub> Crystallization Fouling on a Heat Exchanger," *International Journal of Heat and Mass Transfer*, vol. 83, pp. 84-98, 2015.
- [72] O. A. Hamed and H. A. Al-Otaibi, "Prospect of operation of MSF Desalination plants at high TBT and low antiscalant dosing rate," *Desalination*, pp. 181-189, 2010.
- [73] D. Kern and R. E. Seaton, "A theoretical analysis of thermal surface fouling," *British Chemical ENgineering*, vol. 14, no. 5, p. 258, 1959.
- [74] "Britannica," [Online]. Available: [Britannica.com/science/seawater](http://Britannica.com/science/seawater). [Accessed 11 2021].
- [75] A. Delyannis and E. Delyannis, Gmelin Handbuch der anorganischen chemie, "Sauerstoff" Anhang "water Desalting, Verlag: Springer, 1974.
- [76] S. M. Alsadaie and I. M. Mujtaba, "Dynamic Modeling of Heat Exchanger Fouling in Multistage Flash Desalination," *Desalination*, vol. 2017, pp. 47-65.
- [77] F. J. Millero, "Thermodynamics of the Carbon Dioxide System int the Ocean," *GeoChim. Cosmochim*, pp. 661-667, 1995.
- [78] W. Augustin and M. Bohnet, "Influence of the Ratio of Free hydrogen Ions on Crystallization Fouling," *Chem Engineering Process*, vol. 34, pp. 79-85, 1995.
- [79] A. Helalizadeh, H. Müller-Steinhagen and M. Jamalrahmadi, "Mathematical Modelling of Mixed Salt Precipitation During Convective Heat Transfer and Sub-cooled Flow Boiling," *Chem Engineering Science*, pp. 5078-5088, 2005.
- [80] R. A. Konak, "A New Model for Surface Reaction-Controlled Growth of Crystals from Solution," *Chemical Engineering Science*, vol. 29, pp. 1537-1543, 1974.
- [81] F. Fahimiani, A. P. Watkinson and N. Epstein, "Early events in the precipitation fouling of calcium sulphate dehydrate under sensible heating conditions," *Can. J. Chem. Eng*, pp. 679-691, 2007.
- [82] F. Brahim, W. Augustin and M. Bohnet, "Numerical Simulation of the Fouling Process," *International Journal of Thermal Science*, vol. 42, pp. 323-334, 2003.

- [83] F. Fahiminia, P. Watkinson and N. Epstein, "Investigation of Initial Fouling Rates of Calcium Sulfate Solutions under Non-boiling Conditions," *Engineering Conferences International*, 2003.
- [84] J. T. Howe and W. A. Mersman, "Nasa Technical Note 12," 1959.
- [85] J. Rose, Y. Utaka and I. Tanasawa, Dropwise Condensation, Handbook of Phase Change: Boiling and Condensation, Philadelphia: Taylor and Francis, 1999.

### 8.3. Acknowledgment

Completing this work would not have been possible without the infinite help, unbreakable patience, and generous contribution of Professor Vinod Narayanan.

The invaluable contribution of the committee members, Professor Bryan Jenkins and Professor Valeria La Saponara, is deeply appreciated.

Doctor Erfan Rasouli's precious experimental insight, wisdom, resourcefulness, and delightful sense of humor have rekindled the fires of hope lost to despair.

Doctor Mehdi Famouri's mentorship and countless words of encouragement have illuminated the dark path of the unknown.

Doctor Taymaz Homayouni's ample technical consults are much appreciated.

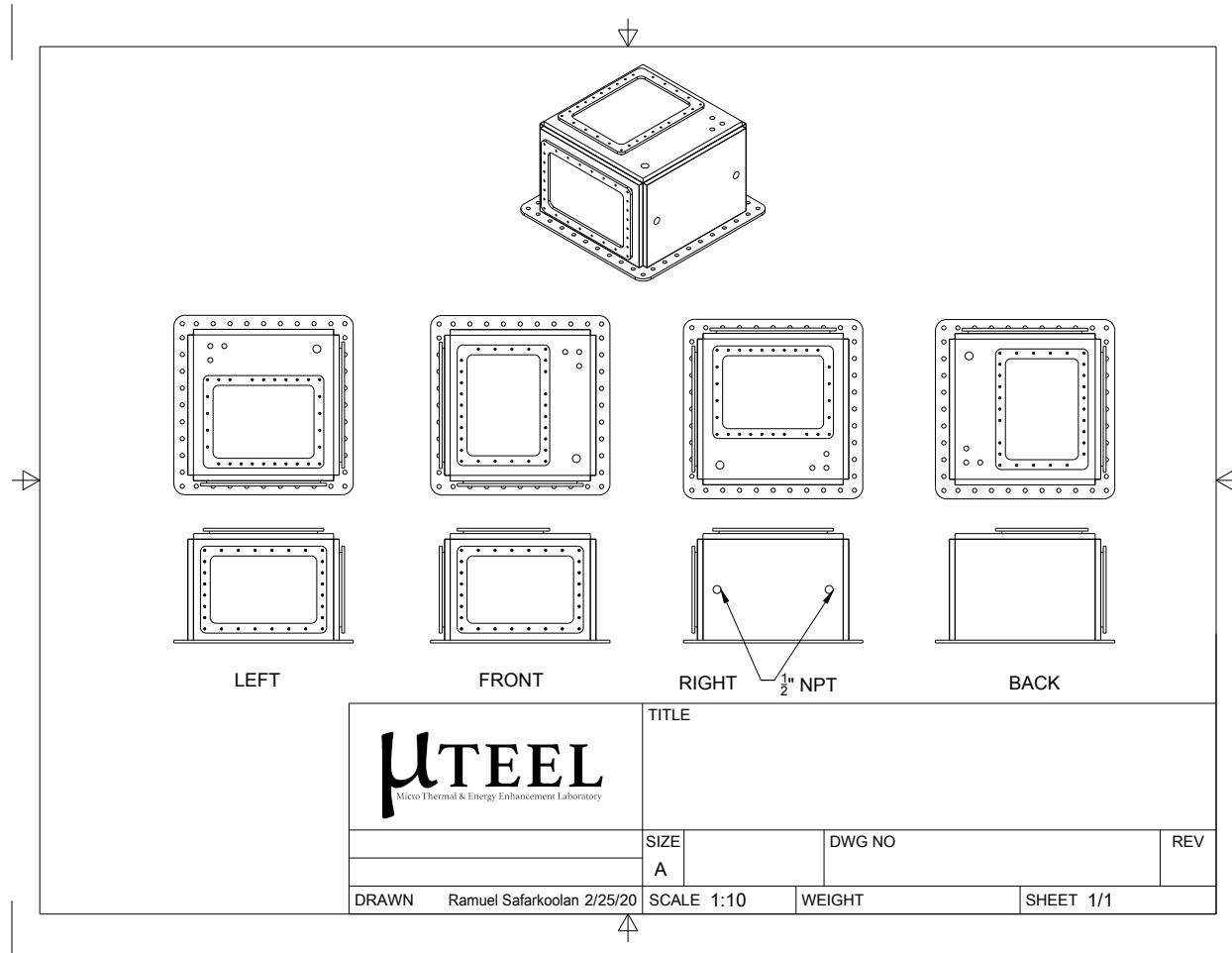
It should be noted that the help of UC Davis Biological and Agricultural Department's machine shop staff, such as Jed Roach, Andy Cobb, Tom Bell, and UC Davis School of Engineering's machine shop manager Jose Mojica has been crucial to the completion of this work.

The help and support of dear friends such as Ehsan Arasteh, Amin Gaffourian, Joe Graff, Chris Nielson, and Alex Schmidt, and the excellent mentorship of internship supervisors Doctor Chuck Mueller and Doctor Leonard Pease's are sincerely valued.

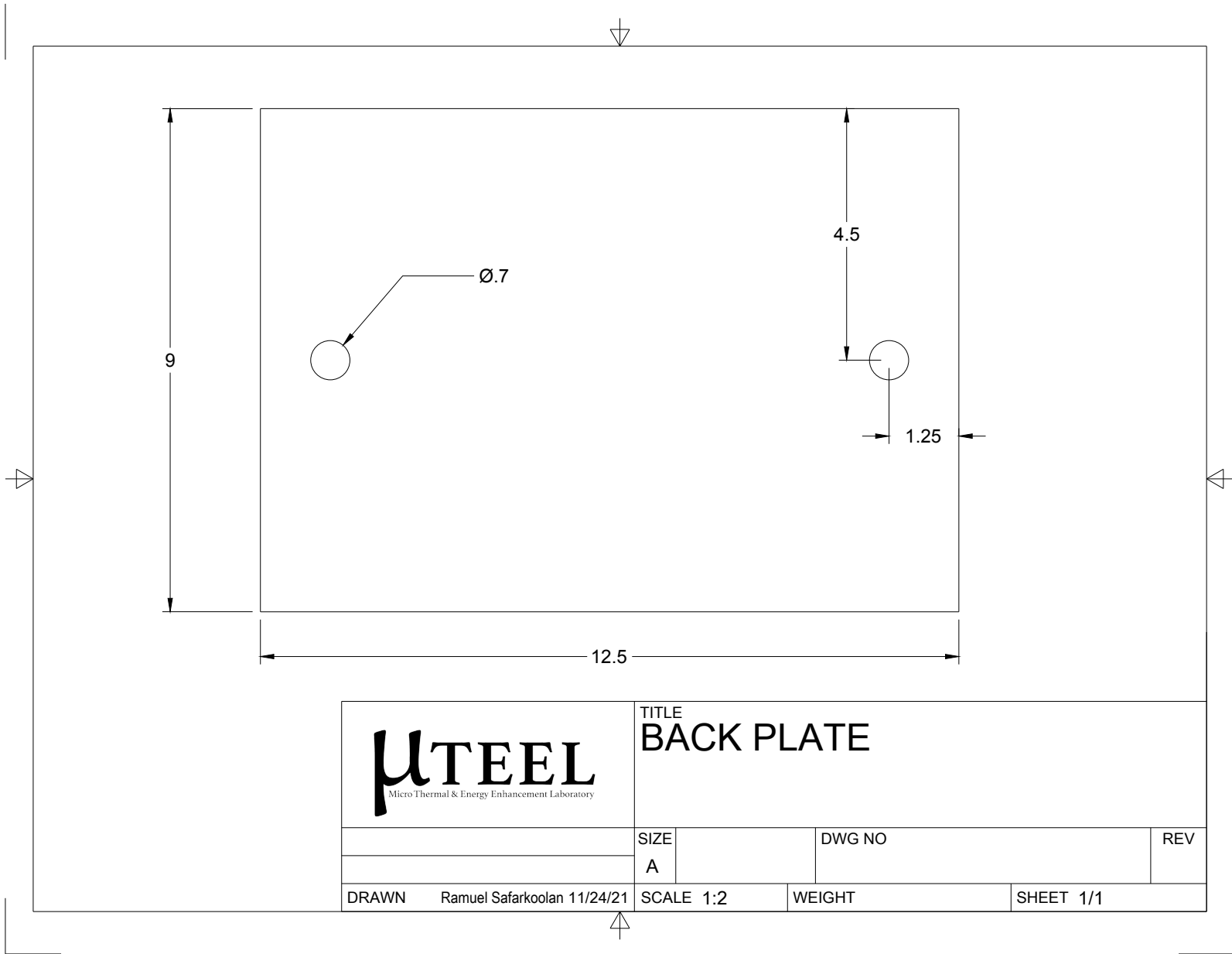
## 8.4. Appendix I: Steam Chamber Blueprint

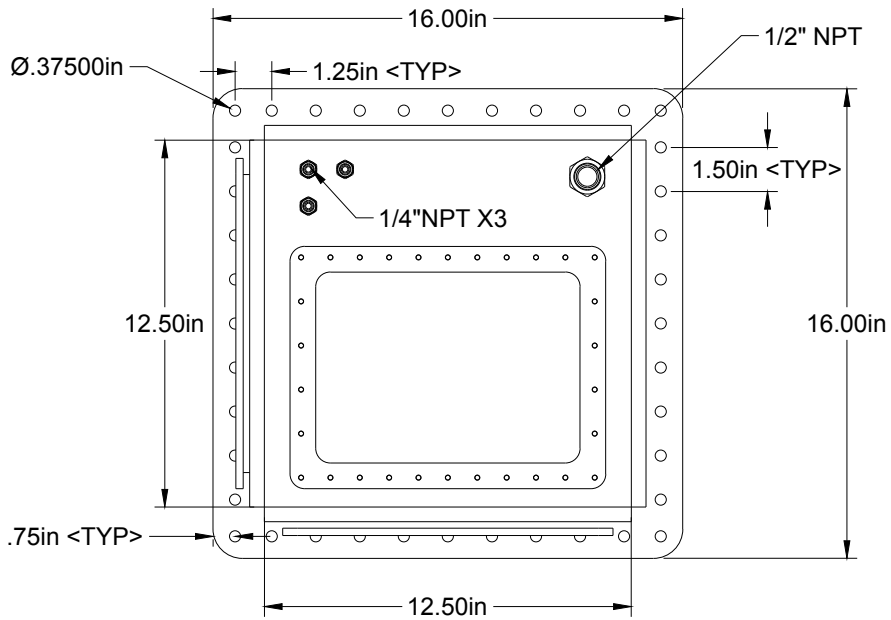
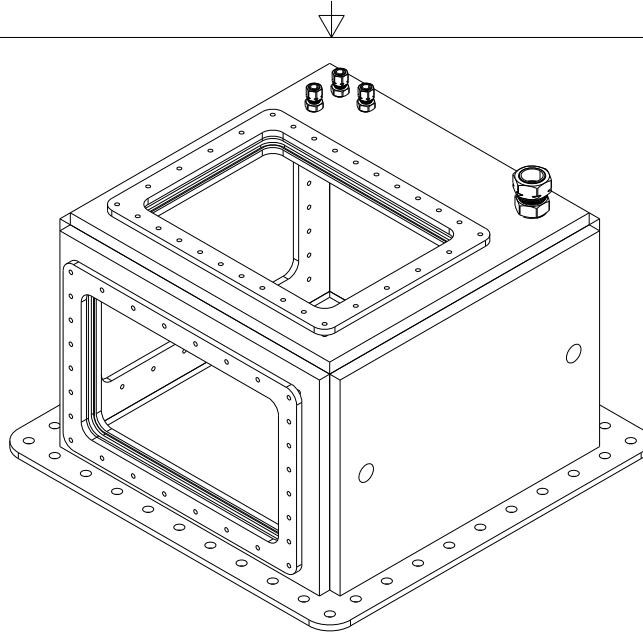
The following are the technical drawings of the steam chamber

168



169

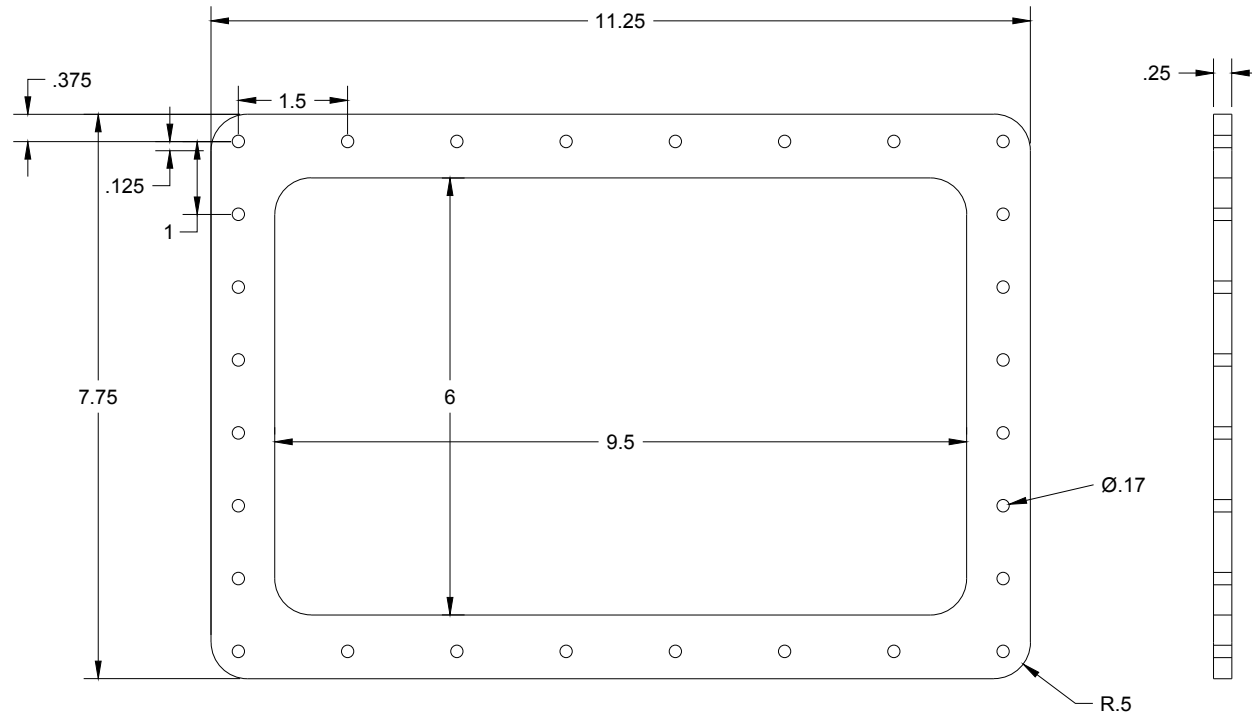





TITLE  
CONDENSATION APARATUS

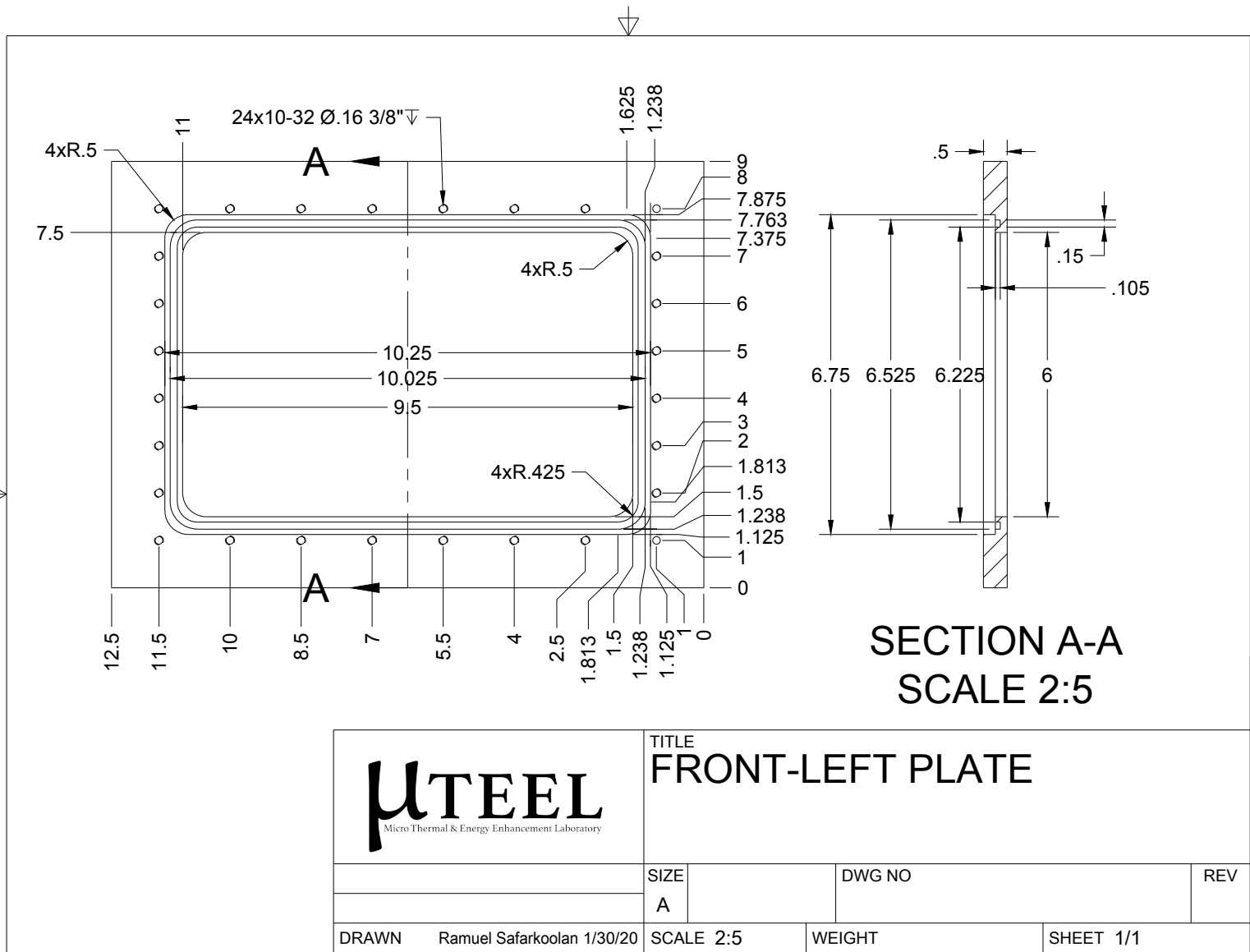
	SIZE	DWG NO	REV
	A		
DRAWN Ramuel Safarkoolan 8/27/21	SCALE 1:5	WEIGHT	SHEET 1/1

171



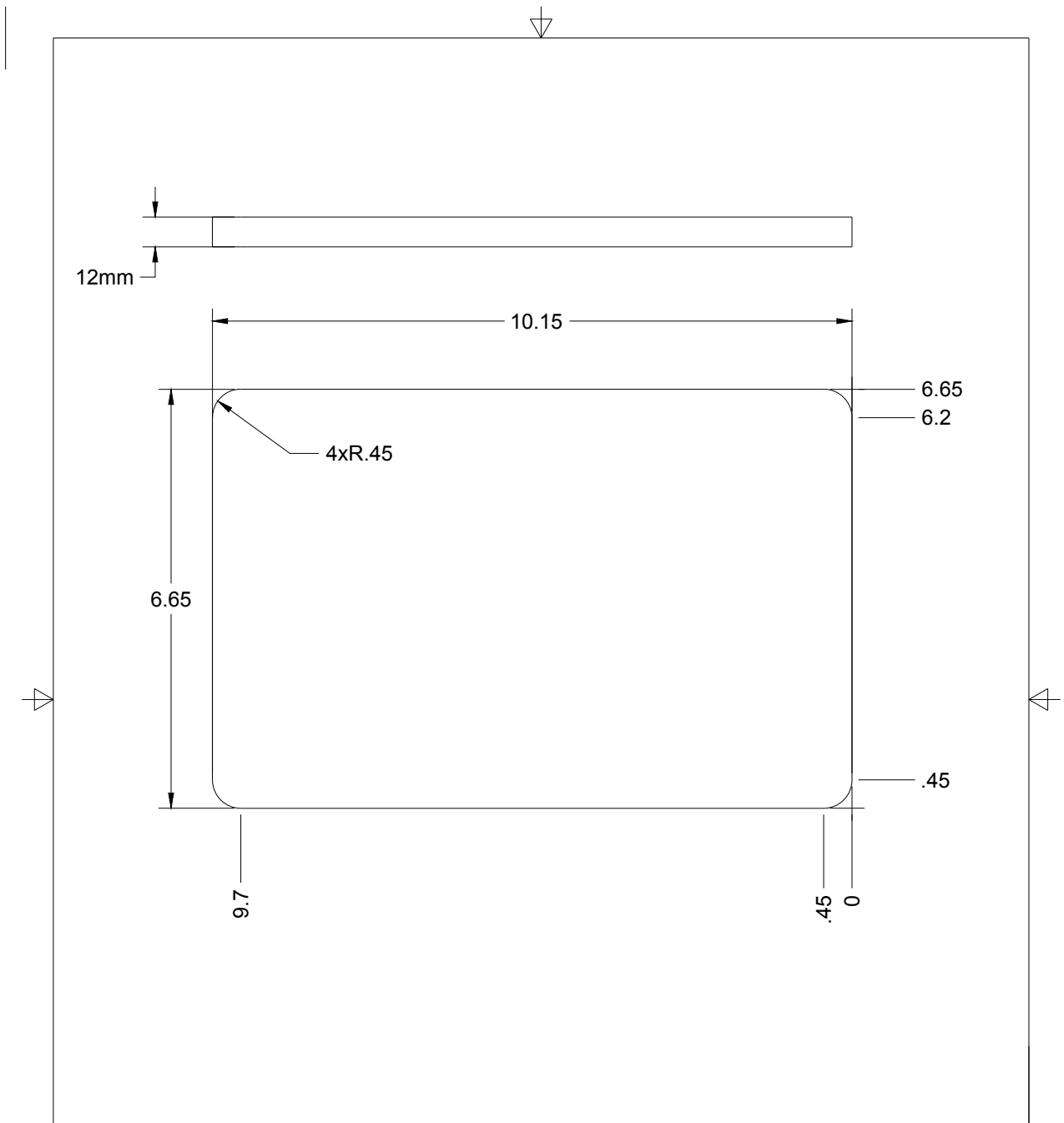
 Micro Thermal & Energy Enhancement Laboratory	TITLE FRONT-LEFT CLAMP		
	SIZE A	DWG NO	REV
DRAWN Ramuél Safarkoolan 1/30/20	SCALE 1:1	WEIGHT	SHEET 1/1


172



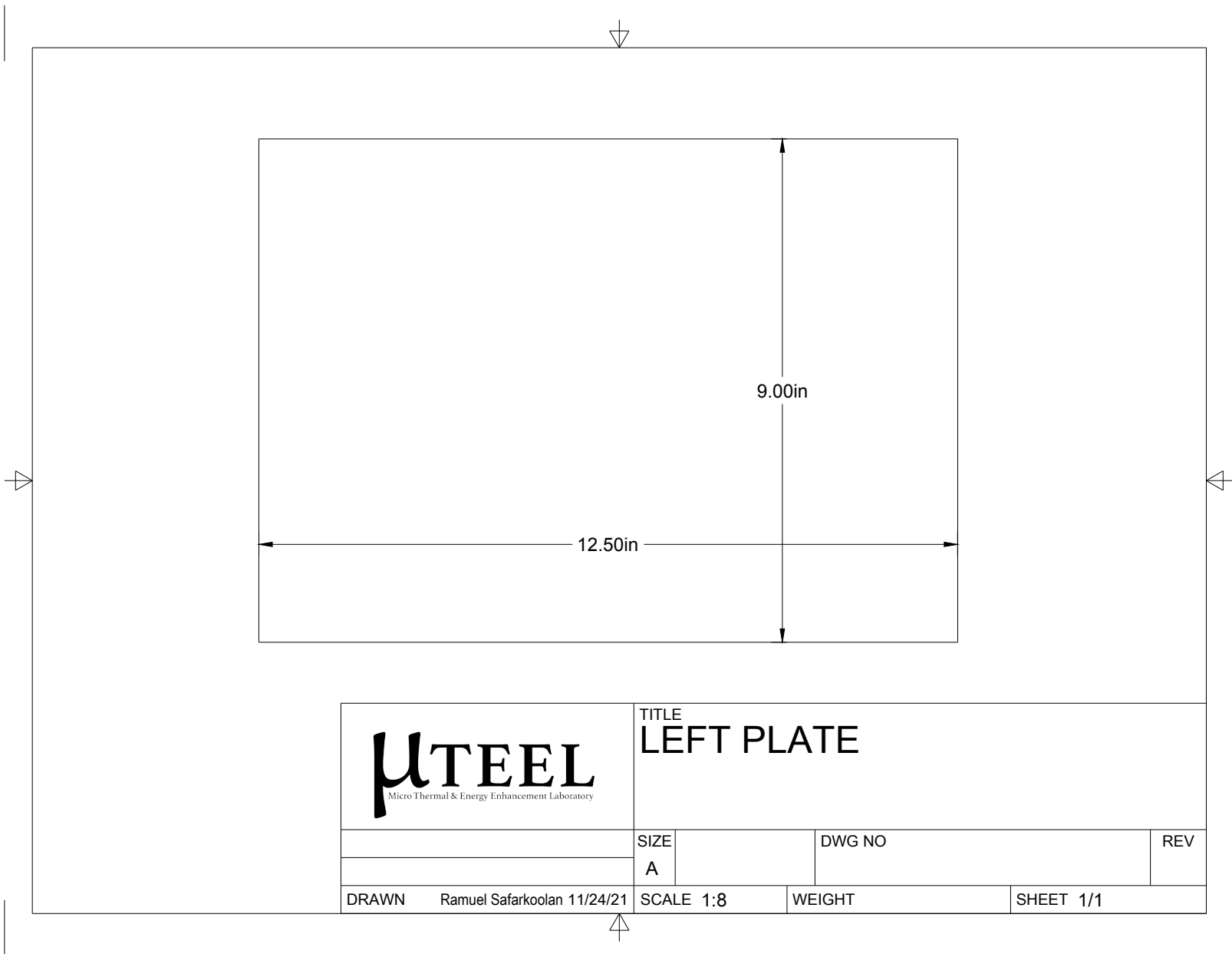
		TITLE	
		FRONT-LEFT PLATE	
	SIZE	DWG NO	REV
	A		
DRAWN	Ramuel Safarkoolan 1/30/20	SCALE 2:5	WEIGHT
			SHEET 1/1




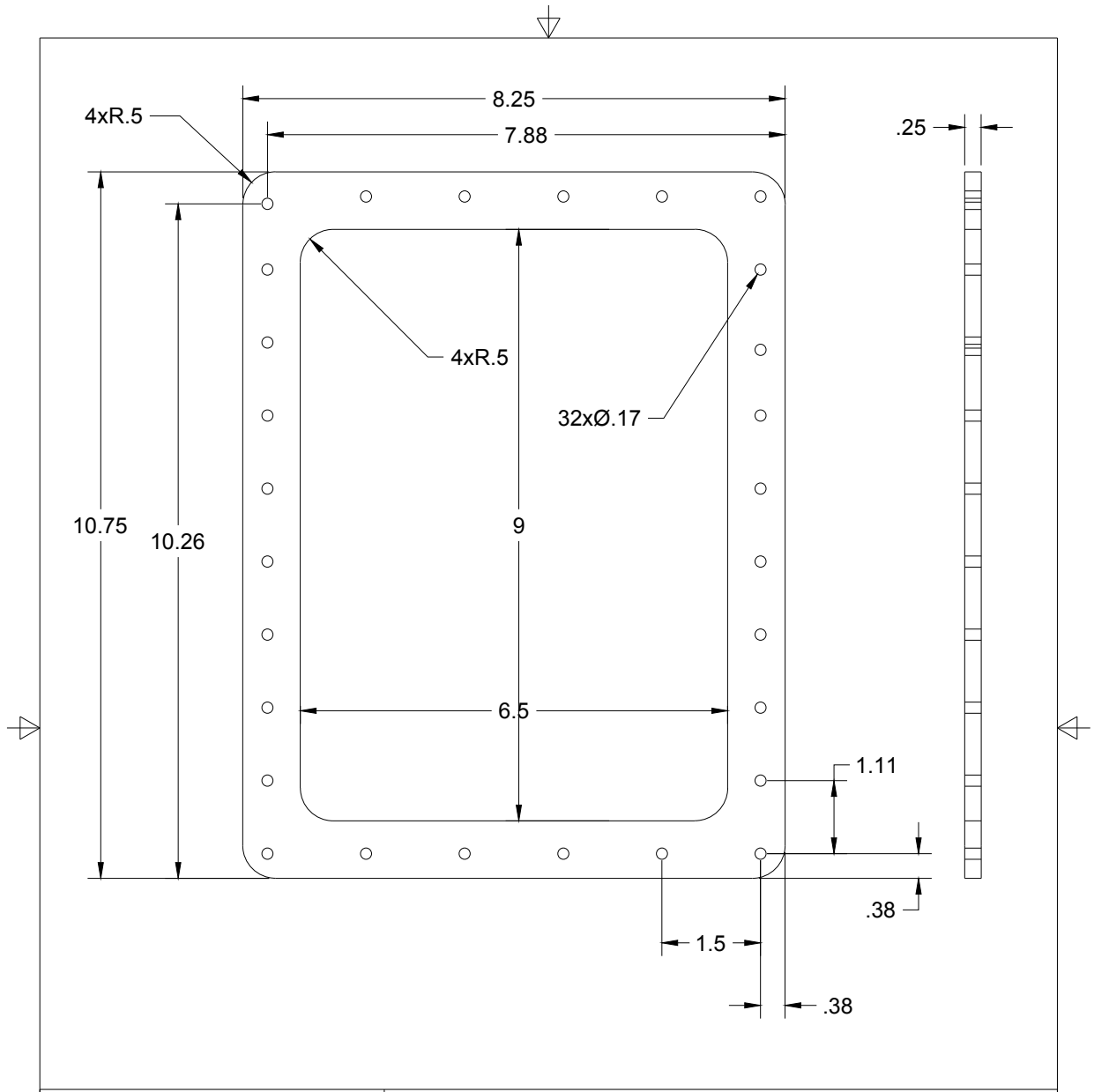


 <p>Micro Thermal &amp; Energy Enhancement Laboratory</p>	TITLE			FRONT-LEFT WINDOW
	SIZE	DWG NO	REV	
	A			
DRAWN	Ramuel Safarkoolan 1/31/20	SCALE 1:2	WEIGHT	SHEET 1/1

174

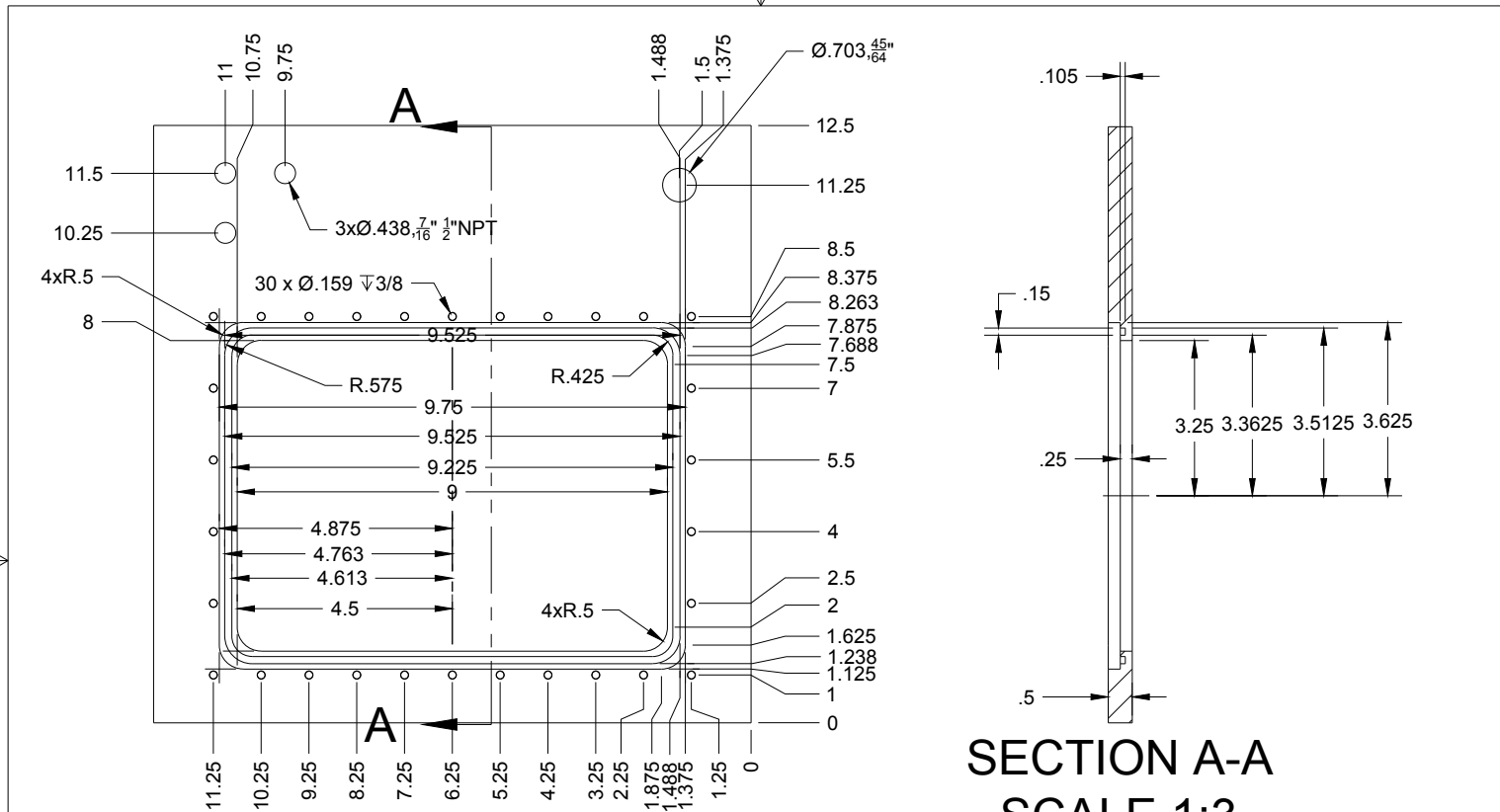


 Micro Thermal & Energy Enhancement Laboratory		TITLE LEFT PLATE	
	SIZE A	DWG NO	REV
DRAWN Ramuel Safarkoolan 11/24/21	SCALE 1:8	WEIGHT	SHEET 1/1




		PROJECT		
		TITLE <b>TOP CLAMP</b>		
APPROVED	SIZE	CODE	DWG NO	REV
CHECKED	A			
DRAWN	Ramuel Safarkoolan 3/3/20	SCALE 1:2	WEIGHT	SHEET 1/1

176



SECTION A-A  
SCALE 1:3

 <p>Micro Thermal &amp; Energy Enhancement Laboratory</p>		TITLE TOP PLATE		
		Ramuel Safarkoolan	SIZE A	DWG NO
DRAWN Ramuel Safarkoolan 1/30/20	SCALE 1:3	WEIGHT	SHEET 1/1	

## 8.5. Appendix II: Derivation of steam velocity

Momentum control volume analysis equation 4 – 467 Nellis and Klein.

$$\underbrace{\frac{d}{dx} \left[ \int_0^\delta (u^2 - uu_\infty) dy \right]}_{\text{momentum change}} + \underbrace{\frac{du_\infty}{dx} \int_0^\delta (u - u_\infty) dy}_{\text{pressure force}} + v_{y=0} u_\infty = \underbrace{-\frac{1}{\rho} \tau_0}_{\text{shear force}} \quad 58$$

3<sup>rd</sup> order polynomial with  $\tau_{y=\delta} = 0$  assumption table 4-4 576 Nellis and Klein.

$$u = u_\infty \frac{\frac{3y}{2\delta} - \frac{y^3}{2\delta^3} + \frac{\rho v \delta \left( \frac{3y^2}{4\delta^2} - \frac{y^3}{2\delta^3} \right)}{\mu} + \frac{\rho \delta^2 \left( \frac{y}{4\delta} - \frac{y^2}{2\delta^2} + \frac{y^3}{4\delta^3} \right) \frac{\partial u_\infty}{\partial x}}{\frac{\rho v \delta}{4\mu} + 1} \quad 59$$

Or if  $\lambda = \frac{y}{\delta}$ , here y is measured from the plate.

$$u = u_\infty \frac{\frac{3}{2}\lambda - \frac{1}{2}\lambda^3 + \frac{\rho v \delta \left( \frac{3}{4}\lambda^2 - \frac{1}{2}\lambda^3 \right)}{\mu} + \frac{\rho \delta^2 \left( \frac{1}{4}\lambda - \frac{1}{2}\lambda^2 + \frac{1}{4}\lambda^3 \right) \frac{\partial u_\infty}{\partial x}}{\frac{\rho v \delta}{4\mu} + 1} \quad 60$$

Substituting the assumed velocity profile in the momentum control volume equation the following terms emerge:

**Momentum Change:**

$$\frac{d}{dx} \left\{ \underbrace{\frac{\delta u_{\infty}^2 \left[ -4\rho^2 \delta^4 \left( \frac{du_{\infty}}{dx} \right)^2 + 9\rho^2 v \delta^3 \frac{du_{\infty}}{dx} u_{\infty} + \delta^2 \left( 54\rho^2 v^2 - 12\mu\rho \frac{du_{\infty}}{dx} \right) + 486\mu\rho v \delta + 936\mu^2 \right]}{420(4\mu + \rho v \delta)^2}} \right\} \quad 61$$

**Pressure Force:**

$$\frac{du_{\infty}}{dx} \left[ -\frac{\delta u_{\infty} \left( -\rho \delta^2 \frac{du_{\infty}}{dx} + 6\rho v \delta + 18\mu \right)}{12(4\mu + \rho v \delta)} \right] \quad 62$$

**Shear Stress:**

$$\tau_0 = \frac{\rho u_{\infty} \mu \delta^2 \frac{du_{\infty}}{dx} + 6u_{\infty} \mu^2}{(\rho v \delta^2 + 4\mu \delta)} \quad 63$$

**Shear Force:**

$$-\frac{\rho u_{\infty} \mu \delta^2 \frac{du_{\infty}}{dx} + 6u_{\infty} \mu^2}{\rho(\rho v \delta^2 + 4\mu \delta)} \quad 64$$

When Momentum change, pressure force, and shear force for the assumed velocity profile are substituted into the momentum control volume the following equation emerges.

$$\frac{dB}{dx} + \frac{du_\infty}{dx} \left[ -\frac{\delta u_\infty \left( -\rho\delta^2 \frac{du_\infty}{dx} + 6\rho v\delta + 18\mu \right)}{12(4\mu + \rho v\delta)} \right] + v u_\infty = -\frac{\rho u_\infty \mu \delta^2 \frac{du_\infty}{dx} + 6u_\infty \mu^2}{\rho(\rho v\delta^2 + 4\mu\delta)} \quad 65$$

Discretizing the problem in x direction we have n control volumes

$$n = \frac{h}{\Delta x} \quad 66$$

Applying the discretization to equation 8 we have:

$$\begin{aligned} \frac{B_{i+1} - B_i}{\Delta x} + \frac{u_{\infty,i+1} - u_{\infty,i}}{\Delta x} \left[ -\frac{\delta_i \overline{u_{\infty,i}} \left( -\rho\delta_i^2 \frac{u_{\infty,i+1} - u_{\infty,i}}{\Delta x} + 6\rho v_i \overline{\delta_i} + 18\mu \right)}{12(4\mu + \rho v_i \overline{\delta_i})} \right] + \overline{v_i} \overline{u_{\infty,i}} \\ = -\frac{\rho \overline{u_{\infty,i}} \mu \overline{\delta_i}^2 \frac{u_{\infty,i+1} - u_{\infty,i}}{\Delta x} + 6\overline{u_{\infty,i}} \mu^2}{\rho(\rho \overline{v_i} \overline{\delta_i}^2 + 4\mu \overline{\delta_i})} \end{aligned} \quad 67$$

Where the bar operator,  $\overline{\phantom{x}}$ , indicates the current and next control volume averaged value, i.e.

$$\overline{x_i} = \frac{x_i + x_{i+1}}{2}. \quad 68$$

With surface shear stress defined as

$$\tau_{0,i} = \frac{\overline{\rho u_{\infty,i}} \overline{\mu \delta_i^2} \frac{u_{\infty,i+1} - u_{\infty,i}}{\Delta x} + 6 \overline{u_{\infty,i}} \mu^2}{\overline{\rho v_i} \overline{\delta_i^2} + 4 \overline{\mu \delta_i}} \quad 69$$

On the liquid side, conservations of energy and momentum balance lead to the following equation

$$k_l \frac{T_{sat,i} - T_w}{\overline{\delta_{\ell,i}} h_{fg}} = \rho \left[ \frac{(\rho - \rho_{\infty})}{\mu_f} g \overline{\delta_{\ell,i}^2} \frac{\delta_{\ell,i+1} - \delta_{\ell,i-1}}{\Delta x} \pm \frac{\tau_{0,i}}{\mu_f} \overline{\delta_{\ell,i}} \frac{\delta_{\ell,i+1} - \delta_{\ell,i}}{\Delta x} \pm \frac{\delta_{\ell,i}^2}{2\mu_f} \frac{\tau_{0,i+1} - \tau_{0,i}}{\Delta x} \right] \quad 70$$

Steam velocity is related to steam mass flow rate through the following equation

$$u_{\infty,i} = \frac{\dot{m}_i}{\rho_s(DL)} \quad 71$$

Control-volume Pressure change assuming inviscid flow outside the boundary layer is given by Bernoulli's equation

$$P_{i+1} = P_i - \frac{1}{2} \rho_s (u_{\infty,i+1}^2 - u_{\infty,i}^2) \quad 72$$

The mass flow rate change across the control volume is only due to condensation and given by

$$\dot{m}_{i+1} = \dot{m}_i - 2\dot{c}_i \quad 73$$

Control volume condensation is calculated from

$$\dot{c}_i = k \frac{T_{sat,i} - T_w}{\overline{\delta_{\ell,i}} h_{fg,i}} \quad 74$$



And the control volume saturation temperature is calculated from

$$T_{sat,i} = T_{sat,i}(P_i)$$

75

Control volume suction velocity is calculated from

$$v_i = \frac{\dot{c}_i}{\rho_l L \Delta x}$$

76

The unknowns in equations 10,12-19 are

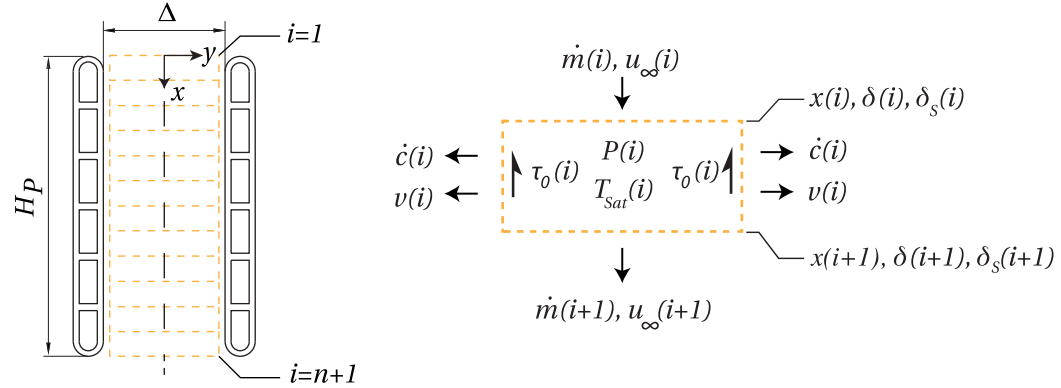
$$v_{1-n}, c_{1-n}, \dot{m}_{1-n}, u_{\infty,1-n}, \delta_{1-n}, \delta_{s,1-n}, \tau_{0,1-n}, T_{sat,1-n}, B_{1-n}, P_{1-n}$$

Which can be solved for using the following boundary conditions

$$x_1 = \delta_1 = \delta_{s,1} = B_1 = v_{n+1} = \dot{m}_{n+1} = \tau_{0,1} = 0$$

77

and prescribed steam saturation temperature,  $T_{sat,0}$ , plate to plate spacing,  $D$ , plate height,  $H$ , and length,  $L$



Equations for internal flow part  $2\delta_s \geq \Delta$

$$u \frac{\partial u}{\partial x} + v \frac{\partial u}{\partial y} = -\frac{1}{\rho} \frac{dp}{dx} + \nu \left( \frac{\partial^2 u}{\partial x^2} + \frac{\partial^2 u}{\partial y^2} \right) \quad 78$$

Integrate with respect to y from  $y = 0, y = \Delta/2$

$$\int_0^{\Delta/2} u \frac{\partial u}{\partial x} dy + \underbrace{\int_0^{\Delta/2} v \frac{\partial u}{\partial y} dy}_2 = \int_0^{\Delta/2} \frac{1}{\rho} \frac{dp}{dx} dy + \int_0^{\Delta/2} \nu \frac{\partial^2 u}{\partial x^2} dy + \int_0^{\Delta/2} \nu \frac{\partial^2 u}{\partial y^2} dy \quad 79$$

2 is problematic so

$$d(uv) = vdu + u dv \quad 80$$

Integrate

$$\int_0^{\Delta/2} d(uv) = \int_0^{\Delta/2} v \frac{\partial u}{\partial y} dy + \int_0^{\Delta/2} u \frac{\partial v}{\partial y} dy \quad 81$$

$$\underbrace{u_{\Delta/2} v_{\Delta/2} - u_0 v_0}_0 = \int_0^{\Delta/2} v \frac{\partial u}{\partial y} dy + \int_0^{\Delta/2} u \frac{\partial v}{\partial y} dy \quad 82$$

$$\int_0^{\Delta/2} v \frac{\partial u}{\partial y} dy = u_0 v_0 - \int_0^{\Delta/2} u \frac{\partial v}{\partial y} dy \quad 83$$

$$\int_0^{\Delta/2} v \frac{\partial u}{\partial y} dy = u_0 v_0 + \int_0^{\Delta/2} u \frac{\partial u}{\partial x} dy \quad 84$$

What is  $v_0$ ?

Continuity

$$\int_0^{\Delta/2} \frac{\partial u}{\partial x} dy = - \int_0^{\Delta/2} \frac{\partial v}{\partial y} dy \quad 85$$

$$\int_0^{\Delta/2} \frac{\partial u}{\partial x} dy = - \int_{v_0}^{v_{\Delta/2}} dv = -(v_{\Delta/2} - v_0) \quad 86$$

$$v_0 = \int_0^{\Delta/2} \frac{\partial u}{\partial x} dy + v_{\Delta/2} \quad 87$$

Combined eq 87 with 84

$$\int_0^{\Delta/2} v \frac{\partial u}{\partial y} dy = u_0 \left( \int_0^{\Delta/2} \frac{\partial u}{\partial x} dy + v_{\Delta/2} \right) + \int_0^{\Delta/2} u \frac{\partial u}{\partial x} dy \quad 88$$

Multiply eq 88 by  $\rho$  and  $\boxed{2}$  is known:

$$\underbrace{\int_0^{\Delta/2} v \frac{\partial u}{\partial y} dy}_2 = u_0 \left( \int_0^{\Delta/2} \frac{\partial u}{\partial x} dy + v_{\Delta/2} \right) + \int_0^{\Delta/2} u \frac{\partial u}{\partial x} dy \quad 89$$

Since pressure is assumed only to be a function of x the pressure term can be integrated to yield

$$\int_0^{\Delta/2} \frac{1}{\rho} \frac{dp}{dx} dy = \frac{\Delta}{2\rho} \frac{dp}{dx}. \quad 90$$

To solve equation 79 a second order polynomial velocity profile

$$\frac{u}{u_0} = a\lambda^2 + b\lambda + c \quad 91$$

With the following boundary conditions

$$\lambda = 0; u = u_0, \frac{\partial u}{\partial y} = 0 \quad 92$$

$$\lambda = 1; u = 0$$

is assumed.

The boundary conditions dictate that the velocity profile takes the following form

$$\lambda = 1; u = 0 \rightarrow a + b + c = 0$$

$$\lambda = 0; u = u_0 \rightarrow c = 1$$

$$\lambda = 0; \frac{\partial u}{\partial y} = 0 \rightarrow b = 0 \quad 93$$

$$a = -1$$

Or

$$\frac{u}{u_0} = -\lambda^2 + 1 \quad 94$$

Mass flux through the control volume is

$$\dot{m} = 2 \int_0^{\Delta/2} \rho u L dy \quad 95$$

Or

$$\dot{m} = 2\rho L \int_0^{\Delta/2} u dy \quad 96$$

$$\lambda = \frac{y}{\Delta/2} \rightarrow \Delta/2 \lambda = y \rightarrow \Delta/2 d\lambda = dy$$

$$\dot{m} = \rho L \Delta \int_0^1 u d\lambda = \rho L u_0 \Delta \int_0^1 (-\lambda^2 + 1) d\lambda = \frac{2}{3} u_0 \Delta \rho L \quad 97$$

$$\boxed{u_0 = \frac{3}{2} \frac{\dot{m}}{\Delta \rho L}} \quad 98$$

Since  $m$  is a function of  $x$ , so is  $u_0$ .

$$\frac{\partial u}{\partial x} = (-\lambda^2 + 1) \frac{du_0}{dx} \quad 99$$

$$\begin{aligned} \int_0^{\frac{\Delta}{2}} \frac{\partial u}{\partial x} dy &= \int_0^{\frac{\Delta}{2}} (-\lambda^2 + 1) \frac{du_0}{dx} dy = \frac{du_0}{dx} \int_0^{\frac{\Delta}{2}} (-\lambda^2 + 1) dy = \frac{du_0}{dx} \frac{\Delta}{2} \int_0^1 (-\lambda^2 + 1) d\lambda \\ &= \frac{du_0}{dx} \frac{\Delta}{2} \int_0^1 (-\lambda^2 + 1) d\lambda = \frac{du_0}{dx} \frac{\Delta}{3} \end{aligned} \quad 100$$

$$\frac{\partial^2 u}{\partial x^2} = (-\lambda^2 + 1) \frac{d^2 u_0}{dx^2} \quad 101$$

$$\frac{\partial u}{\partial y} = \frac{\partial u}{\partial \lambda} \frac{d\lambda}{dy} (-2\lambda) u_0 \frac{2}{\Delta} = -\frac{4}{\Delta} u_0 \lambda \quad 102$$

$$\frac{\partial^2 u}{\partial y^2} = \frac{\partial}{\partial \lambda} \left( \frac{\partial u}{\partial \lambda} \right) \frac{d\lambda}{dy} = -\frac{4}{\Delta} u_0 \frac{2}{\Delta} = -\frac{8}{\Delta^2} u_0 \quad 103$$

$$\begin{aligned} \int_0^{\Delta/2} u \frac{\partial u}{\partial x} dy &= \frac{\Delta}{2} \int_0^1 u_0 (-\lambda^2 + 1)(-\lambda^2 + 1) \frac{du_0}{dx} d\lambda = \frac{\Delta}{2} u_0 \frac{du_0}{dx} \int_0^1 (-\lambda^2 + 1)^2 d\lambda = \\ &= \frac{\Delta}{2} u_0 \frac{du_0}{dx} \left( \frac{1}{5} \lambda^5 - \frac{2}{3} \lambda^3 + \lambda \right)_0^1 = \frac{4}{15} u_0 \Delta \frac{du_0}{dx} \end{aligned} \quad 104$$

$$\begin{aligned} \int_0^{\Delta/2} v \frac{\partial u}{\partial y} dy &= u_0 \left( \int_0^{\Delta/2} \frac{\partial u}{\partial x} dy + v_{\Delta/2} \right) + \int_0^{\Delta/2} u \frac{\partial u}{\partial x} dy \\ &= u_0 \left( \frac{1}{3} \frac{du_0}{dx} \Delta + v_{\Delta/2} \right) + \frac{4}{15} u_0 \Delta \frac{du_0}{dx} \end{aligned} \quad 105$$

$$= \frac{3}{5} u_0 \Delta \frac{du_0}{dx} + u_0 v_{\Delta/2}$$

$$\nu \int_0^{\Delta/2} \frac{\partial^2 u}{\partial x^2} dy = \nu \frac{\Delta}{2} \int_0^1 (-\lambda^2 + 1) \frac{d^2 u_0}{dx^2} dy = \nu \frac{\Delta}{2} \frac{d^2 u_0}{dx^2} \int_0^1 (-\lambda^2 + 1) dy = \nu \frac{\Delta}{3} \frac{d^2 u_0}{dx^2} \quad 106$$

$$\nu \int_0^{\Delta/2} \frac{\partial^2 u}{\partial y^2} dy = \nu \frac{\Delta}{2} \int_0^1 -\frac{8}{\Delta^2} u_0 d\lambda = -\frac{4\nu u_0}{\Delta} \int_0^1 d\lambda = -\frac{4\nu u_0}{\Delta} \quad 107$$

$$\frac{\Delta}{2\rho} \frac{dp}{dx} = \int_0^{\Delta/2} u \frac{\partial u}{\partial x} dy + \int_0^{\Delta/2} v \frac{\partial u}{\partial y} dy - \int_0^{\Delta/2} \nu \frac{\partial^2 u}{\partial x^2} dy - \int_0^{\Delta/2} \nu \frac{\partial^2 u}{\partial y^2} dy \quad 108$$

$$\frac{\Delta}{2\rho} \frac{dp}{dx} = \frac{4}{15} u_0 \Delta \frac{du_0}{dx} + \frac{3}{5} u_0 \Delta \frac{du_0}{dx} + u_0 v_{\Delta/2} - \nu \frac{\Delta}{3} \frac{d^2 u_0}{dx^2} + 4\nu \frac{u_0}{\Delta} \quad 109$$

$$\frac{\Delta}{2\rho} \frac{dp}{dx} = \frac{13}{15} u_0 \Delta \frac{du_0}{dx} + u_0 v_{\Delta/2} - \nu \frac{\Delta}{3} \frac{d^2 u_0}{dx^2} + 4\nu \frac{u_0}{\Delta}$$

$$\boxed{\frac{dp}{dx} = \frac{26}{15} u_0 \rho \frac{du_0}{dx} + \frac{2\rho}{\Delta} u_0 v_{\Delta/2} - \frac{2}{3} \mu \frac{d^2 u_0}{dx^2} + 8\mu \frac{u_0}{\Delta^2}} \quad 110$$

$$\tau_0(x) = \mu \frac{\partial u}{\partial y} \Big|_{y=\frac{\Delta}{2}} = \mu \frac{\partial u}{\partial \lambda} \Big|_{\lambda=1} \frac{d\lambda}{dy} \Big|_{y=\frac{\Delta}{2}} = \mu u_0 (-2\lambda)_{\lambda=1} \left( \frac{2}{\Delta} \right) = -\frac{4\mu u_0}{\Delta} \quad 111$$

$$\boxed{\tau_0(x) = -\frac{4\mu u_0}{\Delta}} \quad 112$$

$$\frac{\Delta P}{\Delta x} = \frac{26}{15} u_0 \rho \frac{\Delta u_0}{\Delta x} + \frac{2\rho}{\Delta} u_0 v_{\Delta/2} - \frac{2}{3} \mu \frac{\Delta(\Delta u_0)}{\Delta x^2} + 8\mu \frac{u_0}{\Delta^2} \quad 113$$

$$\frac{P_{i+1} - P_i}{\Delta x} = \frac{26}{15} u_{0,i} \rho \frac{u_{0,i+1} - u_{0,i}}{\Delta x} + \frac{2\rho}{\Delta} u_{0,i} v_{\Delta/2,i} - \frac{2}{3} \mu \frac{u_{0,i-1} - 2u_{0,i} + u_{0,i+1}}{\Delta x^2} + 8\mu \frac{u_{0,i}}{\Delta^2} \quad 114$$

$$P_{i+1} = P_i + \frac{26}{15} u_{0,i} \rho (u_{0,i+1} - u_{0,i}) + \frac{2\rho}{\Delta} u_{0,i} v_{\frac{\Delta}{2},i} \Delta x - \frac{2}{3} \mu \frac{u_{0,i-1} - 2u_{0,i} + u_{0,i+1}}{\Delta x} + 8\mu \frac{u_{0,i}}{\Delta^2} \Delta x \quad 115$$

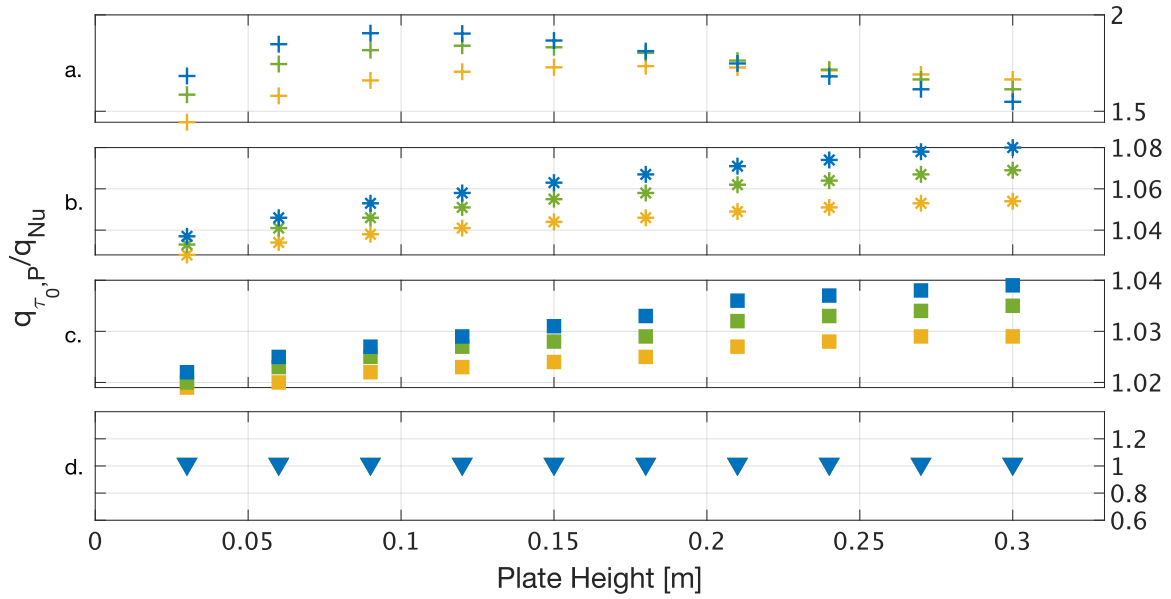
$$P_{i+1} = \mathcal{F}(u_{o,i-1}, u_{o,i}, u_{o,i+1}, P_i)$$

To solve equation 115 and 112 the knowledge of the centerline velocity is required. For that we need to solve the mass balance equation 73.

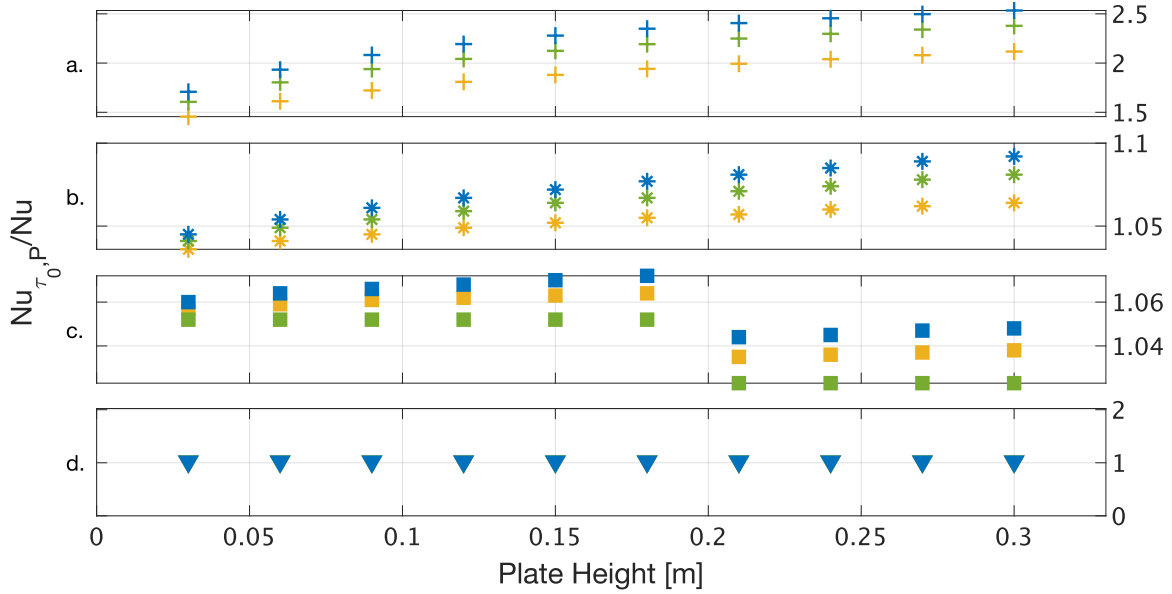


## 8.6. Appendix III: Other subcooling results

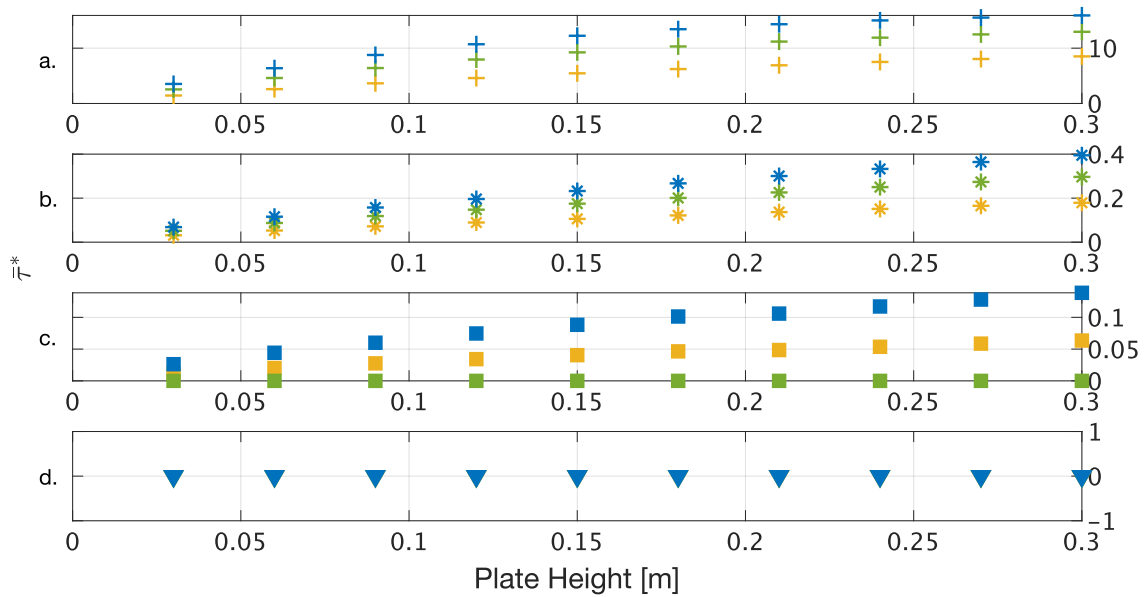
### 8.6.1. $T_{sat} = 100\text{ }^{\circ}\text{C}$



AP Figure 1: Effect of varied plate spacing of a. 1mm, b. 6mm, c. 10 mm, d. 1000 mm, plate height, and subcooling on plate-height condensation flux ratio for  $n = 200$ ,  $T_{sat} = 100^{\circ}\text{C}$ . Mustard, green, and blue shapes represent 4, 8, and 12 K subcooling respectively.

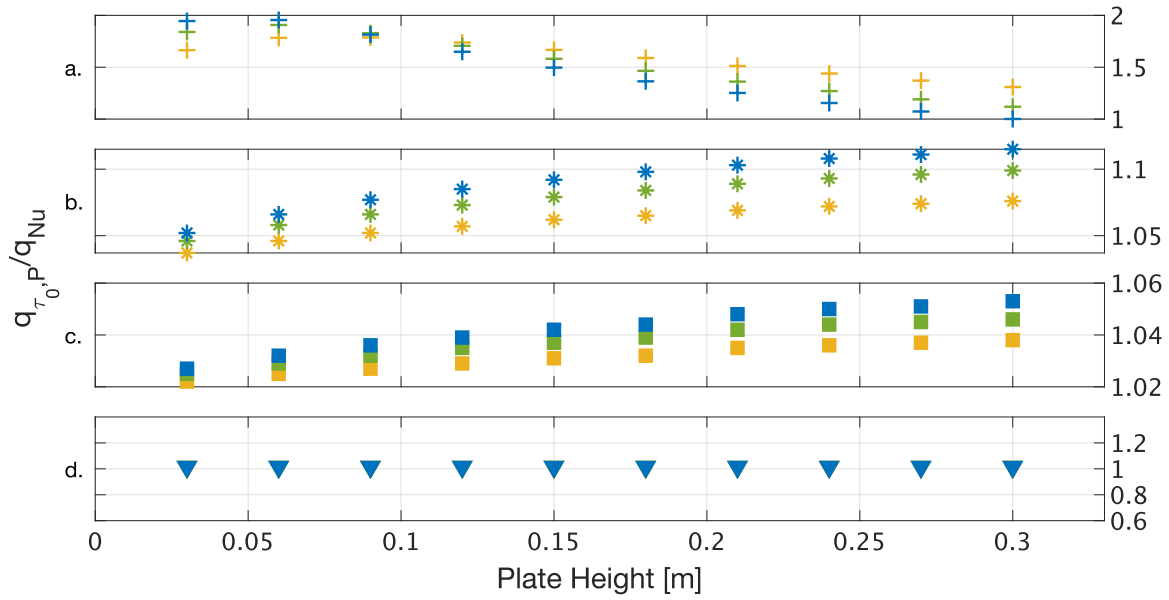


AP Figure 2: Effect of varied plate spacing of a. 1mm, b. 6mm, c. 10 mm, d. 1000 mm, plate height, and subcooling on plate-height averaged Nusselt number ratio for  $n = 200, T_{sat} = 100^\circ\text{C}$ . Mustard, green, and blue shapes represent 4, 8, and 12 K subcooling respectively.

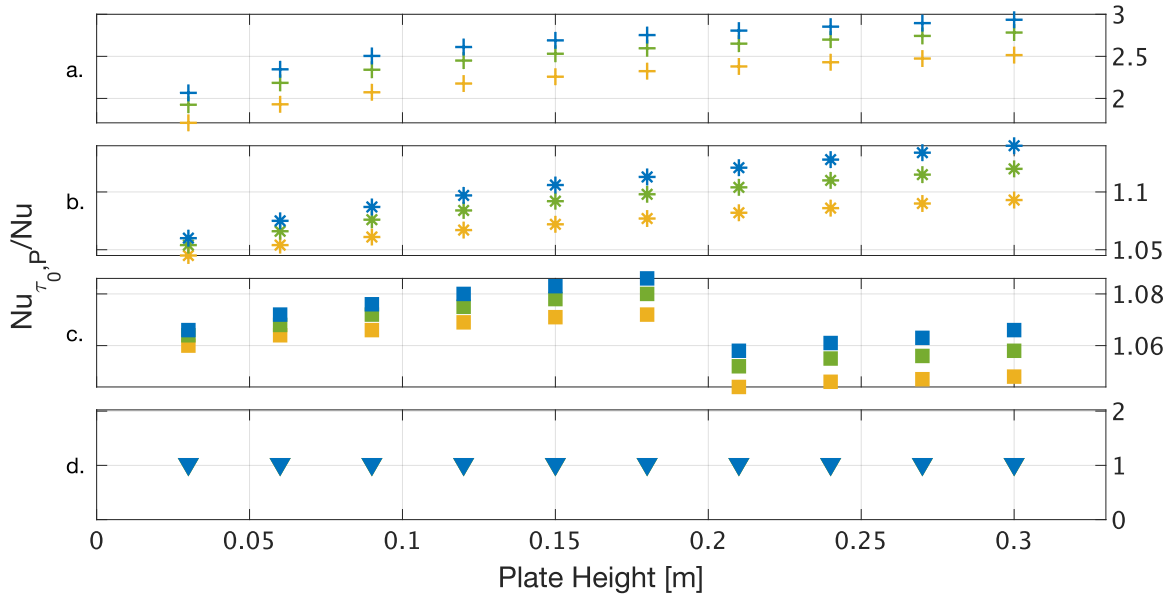


AP Figure 3: Effect of varied plate spacing of a. 1mm, b. 6mm, c. 10 mm, d. 1000 mm, plate height, and subcooling on plate-height averaged nondimensional shear stress for  $n = 200, T_{sat} = 100^\circ\text{C}$ . Mustard, green, and blue shapes represent 4, 8, and 12 K subcooling respectively.

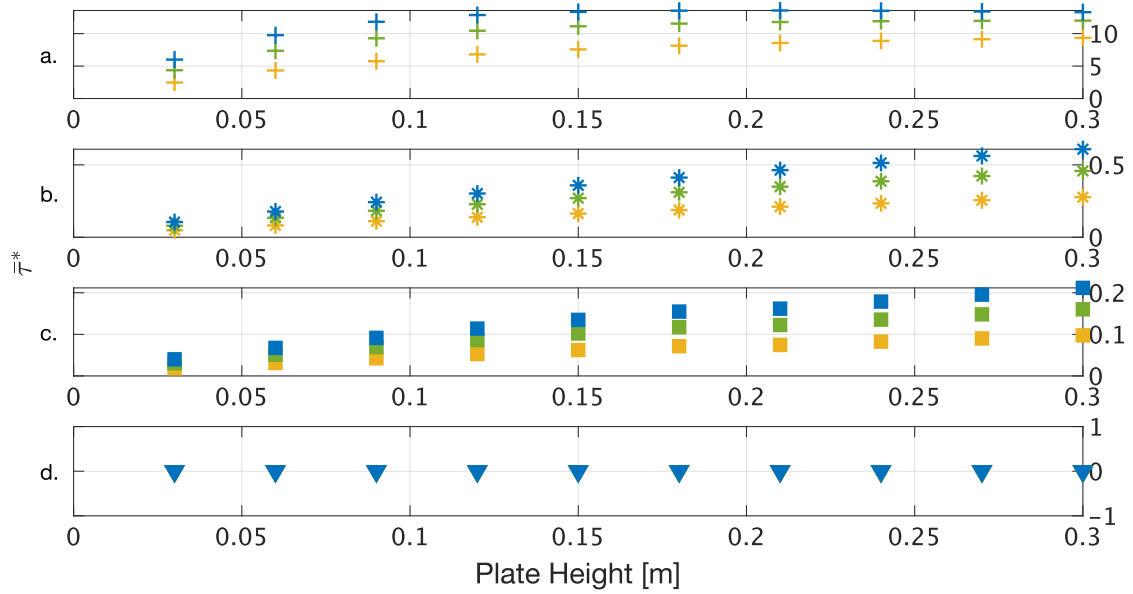
### 8.6.2. $T_{sat} = 80\text{ }^{\circ}\text{C}$



AP Figure 4: Effect of varied plate spacing of a. 1mm, b. 6mm, c. 10 mm, d. 1000 mm, plate height, and subcooling on plate-height condensation flux ratio for  $n = 200, T_{sat} = 80^{\circ}\text{C}$ . Mustard, green, and blue shapes represent 4, 8, and 12 K subcooling respectively.

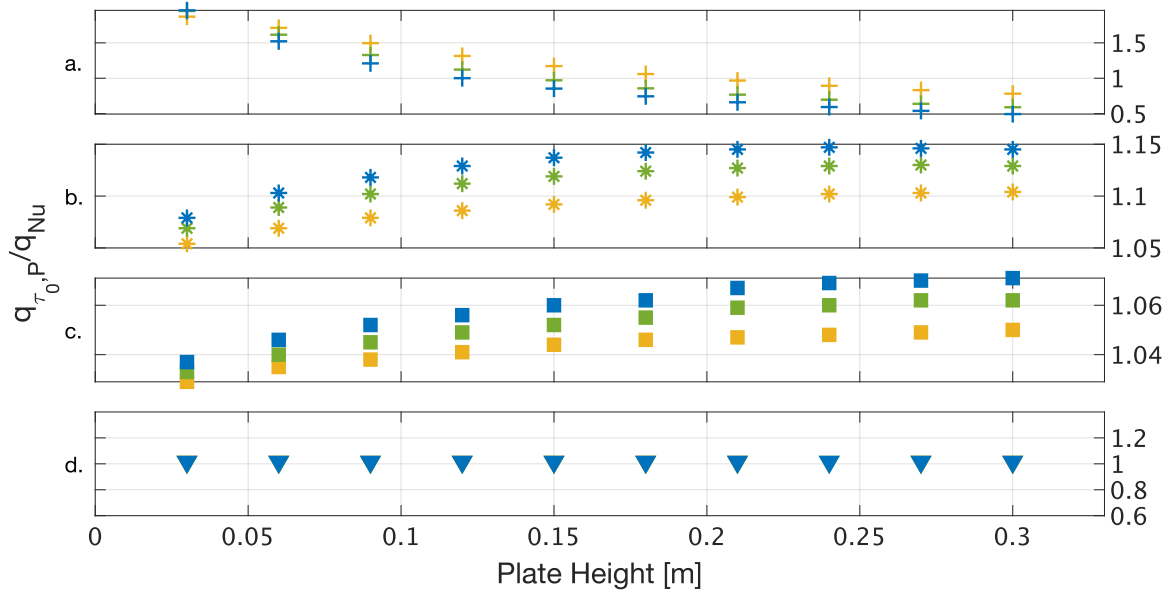


AP Figure 5: Effect of varied plate spacing of a. 1mm, b. 6mm, c. 10 mm, d. 1000 mm, plate height, and subcooling on plate-height averaged Nusselt number ratio for  $n = 200, T_{sat} = 80^{\circ}\text{C}$ . Mustard, green, and blue shapes represent 4, 8, and 12 K subcooling respectively.

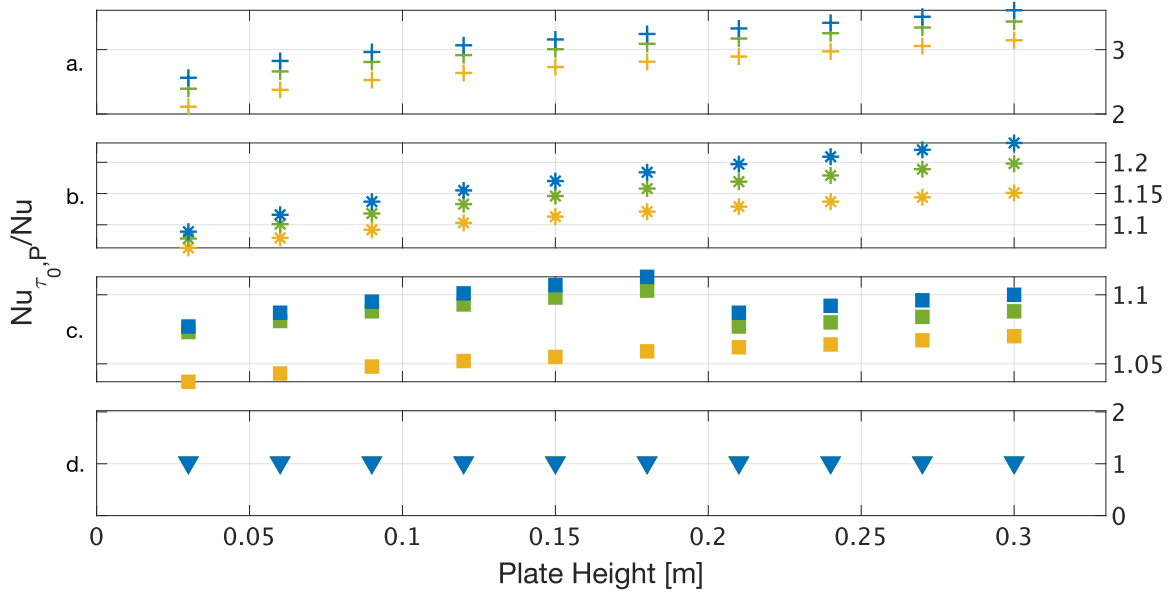


AP Figure 6: Effect of varied plate spacing of a. 1mm, b. 6mm, c. 10 mm, d. 1000 mm, plate height, and subcooling on plate-height averaged nondimensional shear stress for  $n = 200$ ,  $T_{sat} = 80^\circ\text{C}$ . Mustard, green, and blue shapes represent 4, 8, and 12 K subcooling respectively.

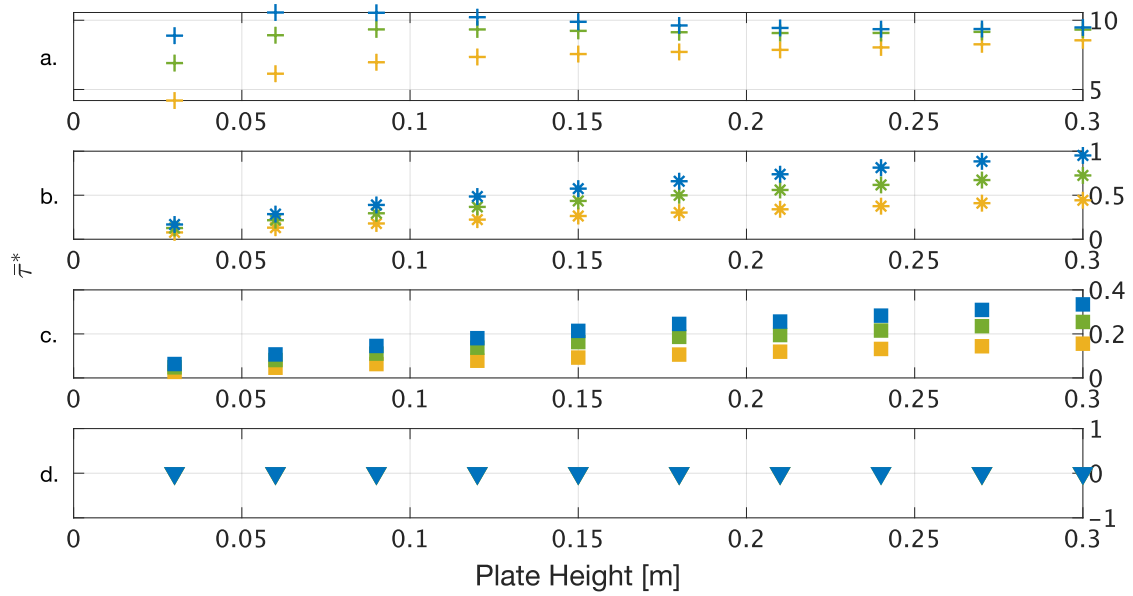
### 8.6.3. $T_{sat} = 60\text{ }^{\circ}\text{C}$



AP Figure 7: Effect of varied plate spacing of a. 1mm, b. 6mm, c. 10 mm, d. 1000 mm, plate height, and subcooling on plate-height condensation flux ratio for  $n = 200, T_{sat} = 60^{\circ}\text{C}$ . Mustard, green, and blue shapes represent 4, 8, and 12 K subcooling respectively.



AP Figure 8: Effect of varied plate spacing of a. 1mm, b. 6mm, c. 10 mm, d. 1000 mm, plate height, and subcooling on plate-height averaged Nusselt number ratio for  $n = 200, T_{sat} = 60^{\circ}\text{C}$ . Mustard, green, and blue shapes represent 4, 8, and 12 K subcooling respectively.



AP Figure 9: Effect of varied plate spacing of a. 1mm, b. 6mm, c. 10 mm, d. 1000 mm, plate height, and subcooling on plate-height averaged nondimensional shear stress for  $n = 200$ ,  $T_{sat} = 80^\circ\text{C}$ . Mustard, green, and blue shapes represent 4, 8, and 12 K subcooling respectively.